University of Catania

Department of Biological, Geological and Environmental Sciences

PhD course on Earth and Environmental Sciences

XXXIV PhD Cycle

Deformation pattern and modelling of active faults along the northern sector of the Malta Escarpment (western Ionian basin)

Dr. Salvatore Gambino

PhD coordinator: Chiar.ma Prof.ssa Agata Di Stefano (Unict)

Supervisor: Chiar.mo Prof. Carmelo Monaco (Unict)

Co-supervisor: Dr. Luciano Scarfì (INGV-CT)

Year 2022

To see a World in a Grain of Sand

And a Heaven in a Wild Flower,

Hold Infinity in the palm of your hand

And Eternity in an hour […].

William Blake (1757-1827)

This thesis has been developed at the Department of Biological, Geological and Environmental sciences – Earth Science section of the **University of Catania** and at the Center for Ocean and Society, Kiel Marine Science, **Christian-Albrechts-University**, Kiel, Germany (within the international mobility under the PhD project).

The project has been founded by the PhD grant '*borsa di Ateneo*' and funding '*Fondo Dottorato*' provided by the Italian Ministry of Education and Research (MIUR).

The project has been developed in collaboration with international research groups:

1. Center for Ocean and Society, Kiel Marine Science, Christian-Albrechts-University, Kiel, Germany (Dr. **Felix Gross**).
2. Laboratoire Géosciences Océan, Univ. Brest/French National Centre for Scientific Research, Plouzané, France (Dr. **Marc-André Gutscher**)

The thesis has been supervised by Prof. **Carmelo Monaco** (Full Professor at the University of Catania) and Dr. **Luciano Scarfì** (First Researcher at the National Institute of Geophysics and Vulcanology – INGV – Etnean Observatory, Catania, Italy).

The manuscript has been reviewed by Prof. **Sebastian Krastel** (Institute of Geosciences Christian-Albrechts-Universität, Kiel, Germany) and by Dr. **Stephane Dominguez** (CNRS UMR 5243 - Géosciences Montpellier, Université de Montpellier, France).

Petex ltd is also acknowledged for providing academic license of the **MOVE** software used throughout this thesis.

Abstract

This research project is based on a multidisciplinary approach including structural-geological, geophysical, and computer-based analyses of active deformation in south-eastern Sicily. This densely populated area is commonly considered one of the most dangerous of the entire Italian peninsula in terms of seismic (and tsunami-related) hazard, being struck by some of the most destructive (M>7.0) earthquakes (and related tsunamis) in historical time.

High-resolution marine seismic data (reflection profiles and bathymetry) allowed a better definition of the spatial extension and in-depth geometry of active faults previously identified in the near offshore between Catania and Syracuse. Here, the Plio-Quaternary reactivation of a Mesozoic extensional, crustal discontinuity (the Malta Escarpment, here referred as MESC) led to the formation of a 60 km-long, N-S trending, E-dipping, extensional fault system whose shallower expression is represented by three main splays controlling the continental slope bathymetric expression and the sedimentation of a turbidite basin at the MESC base.

Seismic interpretation and chrono-stratigraphic correlation based on available literature provided a time-constrain to defining the through-time tectonic activity of faults (throw-rate 0.1-0.4 mm/yr for the Pliocene and up to 3-7 mm/yr for Holocene time). Interpolation of interpreted seismic profiles permitted the development of a 2,5D faults model. Faults-related 3-dimensional parameters were used to derive the maximum expected magnitude (based on empirical scaling relations) indicating a high seismic potential for the studied faults. Return periods of about 500 years, estimated for M≈7 earthquakes based on seafloor faults scarp, have been found for the studied fault system.

Kinematic fault data collected along the SE-Sicily coastal sector, coupled with available literature (borehole, geodetic, and structural data) allowed to define the regional stress field. Stress analysis on 3D fault models (*Slip Tendency*) indicates how the system is well oriented for reactivation (according to the field-derived stress tensors), increasing, thus, the faults seismic potential.

Sequential restoration (also known as back-restoration or back-stripping) performed over two selected seismic profiles allowed a step-by-step analysis of deformation experienced by the fault related turbidite basin. This analysis enabled the validation/recalibration of seismic interpretation, estimation of erosion and, thus, re-assessment of faults throws and heaves. Restoration highlighted how deformation evolved and modulated through time (throw-rate of 0.20-0.40 mm/yr and 0.1-0.05 mm/yr respectively for Pliocene and Pleistocene time). In the early stage (early Pliocene), the basin experienced a significant deformation with the horizontal component prevailing over the vertical one. Such a deformation was diffuse and the MESC faults contributed to roughly one third of the total deformation. Since the early Pliocene the amount of deformation slightly decreased toward the present day, when the MESC faults contribute almost entirely to the total deformation of the studied sector. In addition, the analysis highlighted how the overall deformation should be the result of two different processes: 1) regional (still active) tectonics driving the activity of MESC faults and 2) a ductile deformation controlling the early stage (Pliocene) of the turbidite basin evolution. This latter process may find confirmation in the internal geometry of Pliocene reflectors. Analogies between the seismic-stratigraphic geometries of Pliocene reflectors and sand-box analogue models suggest that the deformation of the turbidite basin may have been controlled by the migration of underlying ductile (salt?) layer within the Messinian units.

Lastly, identification and volume assessment of submarine mass deposits along the studied sector may contribute to the estimation of tsunami hazard and to further constrain the studied faults to historical earthquakes and tsunamis (e.g., the 1169 and 1693 events)

Riassunto

Il presente progetto di ricerca è basato su un approccio multidisciplinare, che include analisi di tipo geologico-strutturale, geofisiche e di modellazione informatica, in Sicilia Sud-orientale. Quest'area densamente popolata, è considerata una delle più pericolose dell'intera penisola italiana in termini di rischio sismico (e relativo rischio tsunami) essendo stata colpita da alcuni dei più distruttivi (M>7.0) eventi sismici (e relativi tsunami) in epoca storica.

Profili sismici e batimetria ad alta risoluzione hanno permesso una definizione più dettagliata dell'estensione e della geometria in profondità di faglie attive precedentemente identificate al largo della costa tra Catania e Siracusa. In quest'area, la riattivazione di una discontinuità crostale di natura estensionale (la Scarpata di Malta, di seguito chiamata MESC) ha portato alla formazione di un sitema di faglie orientato circa N-S, lungo 60 km e immergente verso Est, la cui espressione superficiale è raprresentata da tre faglie principali. Queste ultime, controllano la batimetria della scarpata continentale e la sedimentazione di un bacino torbiditico alla base della stessa.

L'interpretazione dei profili sismici e la correlazione crono-stratigrafica delle unità sismiche (basata su dati di letteratura) hanno consentito di definire l'attività tettonica delle faglie nel tempo (rigetti verticali di 0.1-0.4 mm/a e 3-7 mm/a rispettivamente per il Pliocene e l'Holocene). L'interpolazione dei profili sismici interpretati ha permesso di sviluppare un modello pseudo-tridimensionale (2,5D) delle faglie. I parametri delle faglie tridimensionali sono stati usati per stimare le massime magnitudo attese (in base a relazioni empiriche), indicando un alto potenziale sismico per le faglie studiate (M>7.0). Inoltre, periodi di ritorno per eventi con M≈7 sono stati stimati sulla base delle scarpate di faglia in corrispondenza del fondo marino.

Dati cinematici sui piani di faglia situati a terra lungo il settore costiero, corroborati da dati di letteratura (dati di pozzo, geodetici e strutturali), hanno permesso la definizione del campo di stress regionale. Quest'ultimo, applicato ai modelli di faglia 3D (analisi della Slip Tendency) ha permesso

di osservare come le faglie oggetto di studio, siano ben orientate rispetto allo stress applicato e, pertanto, propense alla riattivazione. Tale considerazione ha un'influenza diretta sulla considerazione del potenziale sismico delle struutre studiate.

L'appicazione, su due profili scelti 'ad hoc', della metodologia d'analisi chiamata Sequential Restoration, ossia basata sul ripristino della deformazione subita dal bacino torbiditico, ha permesso lo studio passo-dopo-passo della storia evolutiva del bacino in oggetto. L'analisi ha, inoltre, permesso la validazione/ri-calibrazione della precedente interpretazione sismica dei profili e di stimare l'erosione subita dalle diverse unità; in tal modo è stato possibile rivalutare i rigetti verticali e orizzontali delle faglie studiate. La ristorazione ha messo in evidenza come la deformazione si sia evoluta e modulata nel tempo (rigetti verticali di 0.2-0.4 mm/a e 0.1-0.05 mm/a rispettivamente per il Pliocene e Pleistocene). Nella fase iniziale (Pliocene inf.) il bacino ha subito una deformazione significativa, con la componente orizzontale che prevaleva su quella verticale. In questa fase, la deformazione era diffusa e suddivisa su più strutture; tra queste, le faglie MESC contribuivano poer circa un terzo della deformazione totale. Questa deformazione è andata diminuendo fino ai giorni nostri; in questa fase le faglie MESC contribuiscono quasi interamente alla deformazione totale del bacino. Questa analisi ha permesso, inoltre, di discriminare due processi deformativi che hanno contribuito alla totale deformazione del bacino; 1) un processo tettonioc (ancora in atto) che guida l'attività delle faglie MESC e 2) una deformazione duttile che ha controllato la deformazione del bacino nelle prime fasi (Pliocene). Quest'ultimo processo sembra trovare conferma analizzando la geometri interna dei riflettori sismici che caratterizzano l'unità attribuita al Pliocene. Analogie tra la geometria dei riflettori sismici dell'unità pliocenica e le osservazioni di modelli analogici in sand-box suggerisce che tale deformazione duttile può essere il risultato di migrazione di sale sottostante al livello Pliocenico (verosimilmente all'interno del Messiniano).

In ultima analisi, l'osservazione e la stima volumetrica di depositi di frane sottomarine lungo il settore studiato, potranno contribuire alla valutazione del rischio tsunami e fornire un ulteriore

vincolo per associare le faglie oggetto di studio ad eventi sismici, e relativi tsunami, avvenuti in epoca storica (ad esempio gli eventi del 1169 e 1693).

1. Introduction

1.1. Motivation and scope

The western Ionian basin (including southern Calabria and eastern Sicily) represents one of the most seismically active sectors of the Mediterranean area. Moreover, the urban areas of Catania, Messina and Syracuse, accounting for about 2 million of people, make the eastern Sicily a high-density populated area, and contribute to increase the risk related to natural hazards (seismic, volcanic, oceanic etc.). Devastating earthquakes have struck this area in historical and instrumental times. Historical catalogues report some of the strongest and most damaging seismic events ever occurred in recent time along the whole Italian peninsula. Among those, the 11 January 1693 (estimated M≈7.4), the 4 February 1169 (estimated M≈7) and other minor, but nevertheless damaging events. The above-mentioned earthquakes caused destruction and uncountable causalities (about 60.000 casualties and more than 40 towns damaged by the 1693 event) over the entire Ionian sector of SE-Sicily. Earthquake-triggered tsunamis have been sporadically reported associated to seismic events, pointing out to a possible offshore source for these earthquakes. However, the actual location of the seismic source is still a matter of debate, and assumptions about possible on shore or offshore faults have been made. In instrumental times, the offshore 13 December 1990 earthquake (M_L=5.4) represents the strongest event recorded in the study area. Moreover, it is commonly considered a further clue for a plausible offshore seismic source for the historically reported strong- to major earthquakes.

The tectonic and geological framework of the area is rather complex being located at the frontal sector of the active Eurasia-Nubia collisional belt. In addition, the area lays at the edge of a crustal scale discontinuity (the Malta Escarpment), recently involved (and reactivated) in the N-S oriented plate collision (and subsequent SE-ward subduction retreat). The Ionian offshore sector of SE-Sicily has been deeply studied in the last two decades, even though only the very recent surveys

provided a detailed view on the structural and tectonic setting of the western Ionian basin. Here, the most striking structural feature is represented by the 300 km-long Malta Escarpment, for long time considered one of the most likely sources of destructive earthquakes. However, advances in the knowledge of the proximal sector of the western Ionian basin depict a quite complex array of tectonic structures whose mutual relations and actual seismo-tectonic roles are still poorly known.

For the reason stated above, a key role, for further evaluation of potential natural hazards and related risks in the eastern Sicily, is played by the achievement of a deeper comprehension of the tectonic, structural and deformation pattern of the offshore area. This thesis deals with the recent and ongoing deformation (style and rate of deformation), definition of seismic potential, stress analysis and overtime deformation of faults located on the reactivated, of the northern portion of the Malta Escarpment and adjacent basin (western Ionian basin). Moreover, evaluation and relative implication of other possible hazards will be treated. The abovementioned goals have been achieved through the seismic-structural interpretation and elaboration of marine seismic data (seismic profiles and bathymetry) acquired during various marine surveys. Interpretation of seismic lines provided a basis for elaboration of 3D models of faults and main horizons. Stress-field determined by elaboration of onshore faults kinematic data and integration with available literature allowed the stress analysis on offshore faults and estimation of their seismic potential. The sequential restoration (back restoration analysis) of selected seismic profiles provided an in-depth insight into the deformation history experienced by the studied basin and involved processes.

1.2. Geological regional Setting

1.2.1. General overview of the study area

The study area localizes on the coastal sector of south-eastern Sicily and western Ionian basin (Fig. 1.1). The region covers about 5.000 km^2, between the latitude 37°00'N - 37°30'N and between the longitude 15°00' E – 16°00' E, and mostly develops offshore. The area is located in the larger context of the central-western Mediterranean (see section 1.2.2), in the framework of Nubia-Eurasia collision (Fig. 1.2). It is in a key position of the orogenic belt since it marks the transition between the collisional belt (Sicily Fold and Thrust Belt - Hyblean foreland) and the subducting Ionian Basin (Fig. 1.1, 1.2).

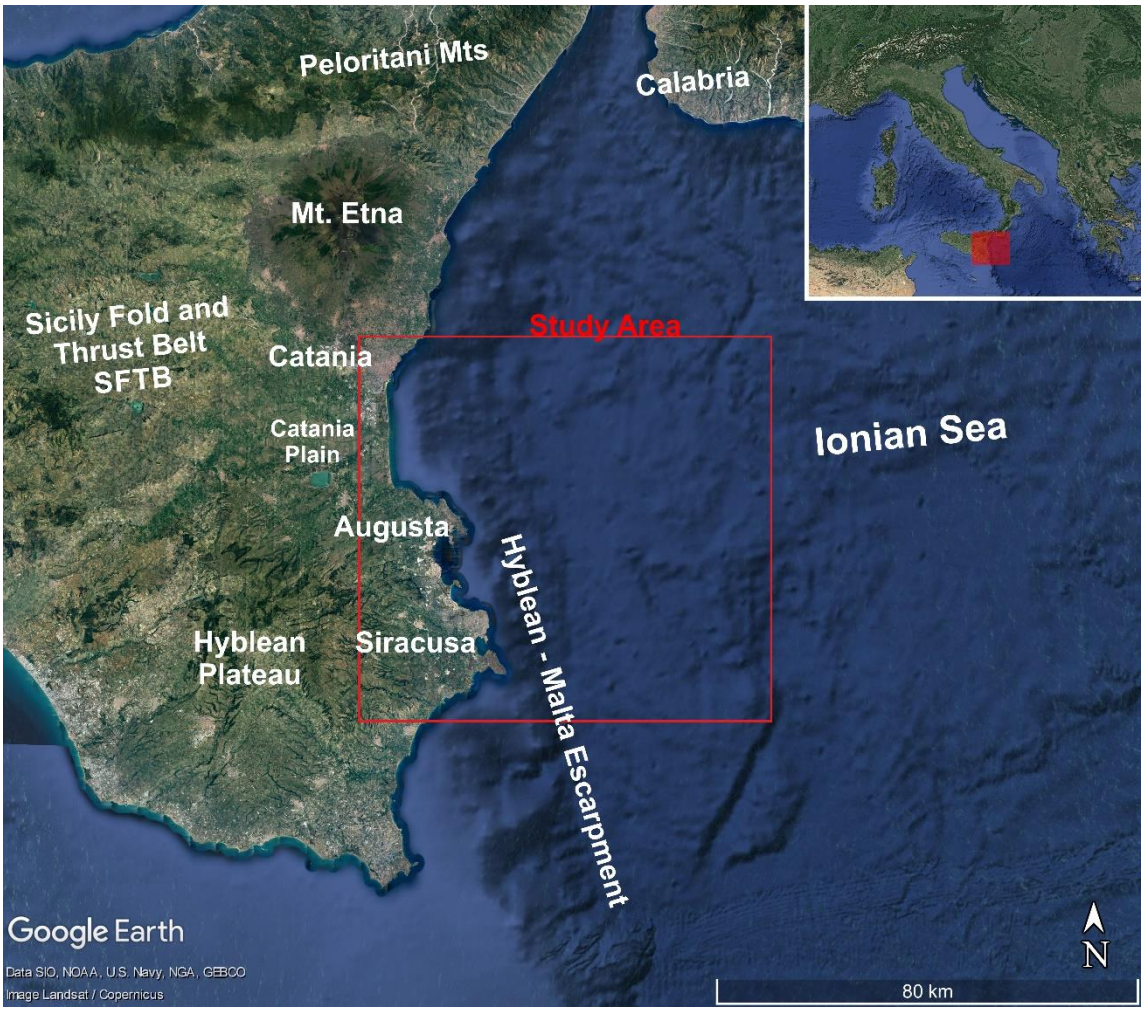

Figure 1. 1. Google Earth view showing location and spatial extension of the study area.

The onshore sector lies between Catania and Siracusa and it is covered by the topographic sheets (1:25.000) 274 and 270 by IGM (Istituto Geografico Militare); the area is also covered by the geological maps "Carta Geologica del Settore Nord-Orientale Ibleo" (1:50.000 - Carbone et al., 1986), "Carta geologica della Sicilia sudorientale" (1:100.000 – Carbone et al., 1984) and by the more recent CARG (CARtografia Geologica) sheets 634 (Catania), 631 (Augusta) and 646 (Siracusa – in progress).

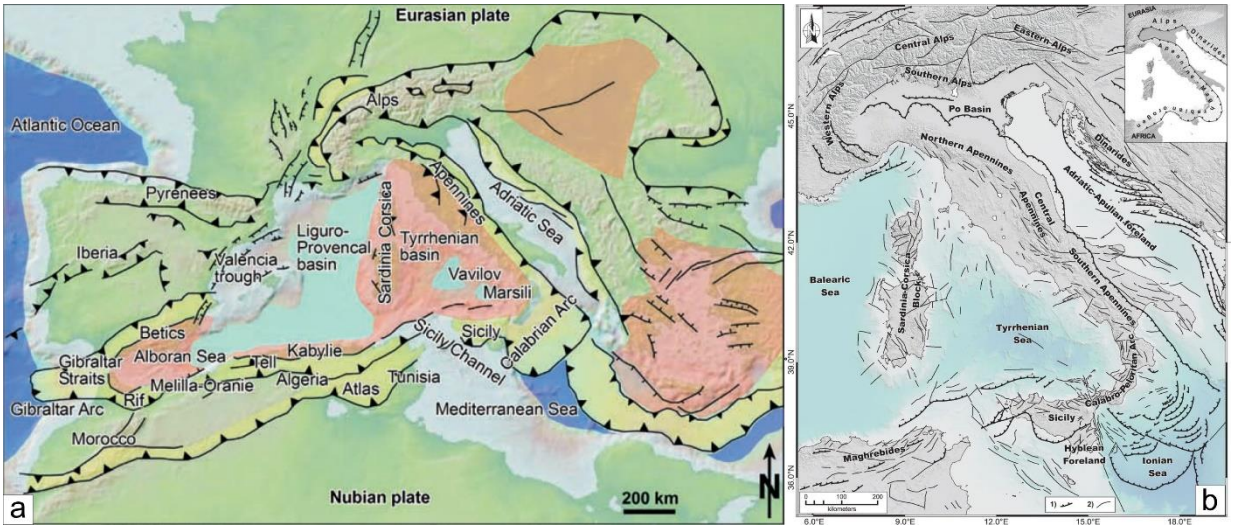

Figure 1. 2. a) Geodynamic setting of the Central–Western Mediterranean (Billi and Salvini 2001). b) Geodynamic-structural setting of the Apenninic-Maghrebian chain along the Italian peninsula and Sicily (Palano et al., 2015).

The study area is extremely varied and diversified both in terms of outcropping lithologies and geological context. In fact, the northern sector (Catania area) is involved in an active contractional deformation due to the ongoing Africa-Europe collision, and it is characterized by terrigenous sequences (alluvials, conglomerates, sandstones and clays) draped by recent volcanics (Mt. Etna – see Branca et al., 2004, 2011 and references therein). The morphology of the coastal area is influenced by historical and pre-historical lava flows, which gently degrade toward the sea where commonly form vertical cliffs due to erosional withdrawal of the coastline. The gentle slope is sometimes displaced by fault scarps (i.e., Timpe faults, NE of Catania – see Fig. 1.8) controlling both morphology and hydrography. The foothill area (Catania surroundings) is currently undergoing regional uplift, which results in the development of various orders of marine terraces (Monaco et al., 2005; Ristuccia et al., 2013).

Conversely, the southern sector is characterised by a relatively undeformed foreland succession, affected by regional uplift (Grasso and Lentini, 1982; Schmincke et al., 1997; Bianca et al., 1999; Monaco et al., 2002; Billi et al., 2006; Scicchitano et al., 2008; Henriquet et al., 2019); here, deformation is mainly extensional, and lithology mainly represented by carbonatic rocks. Topography is rather flat as expected for a carbonatic plateau and shaped by normal faults and fluvial erosion. Morphology is, in fact, dominated by karst plateau deeply carved by river canyons and by various order of marine notches, caves and terraces related to Quaternary paleo-coastlines (Bianca et al., 1999; Meschis et al., 2020). The northern sector of the so-called *Hyblean Plateau* (foreland domain) is characterized by Mesozoic-Cenozoic carbonatic succession and volcanic intercalations (see section 1.2.6). The coastline is rather indented and characterized by Plio-Pleistocene horsts and grabens, generally NW-SE to NNW-SSE oriented. The horsts are mainly constituted by Tertiary carbonates (Mt. Tauro, Maddalena peninsula and Magnisi peninsula), while the grabens are commonly filled by Quaternary deposits.

The transition between the northern and southern sectors is outlined by the presence of a wide alluvial plain which takes the significance of a collisional foredeep, the *Catania Plain*. The plain is formed by sediments (fine sands, silts, sandy gravels, etc.) transported by the Simeto and San Leonardo rivers and their tributaries (Carbone et al., 2009 and references therein).

The offshore sector is characterized by a relatively narrow continental platform which steeply degrades toward the Ionian basin, giving rise to a bathymetric drop of up to 2500 m in less than 15 km from the coast (Fig. 1.1 and 1.3). This impressive slope (with maximum dip of ≈ 30°), known as the Hyblean-Malta Escarpment (or just *Malta Escarpment*, MESC – see section 1.3.2), is the result of Mesozoic extensional processes and Neogene-Quaternary reactivations. The scarp is orthogonally marked by the presence of erosional scars and canyons that drive the eroded continental material downward the slope base where a turbidite valley (Gutscher et al., 2016), roughly N-S oriented, occurs. At the slope base a system of active faults takes place, forming a complicated tectonic pattern

(Fig. 1.5, 1.9). Some of these faults have been considered as the Neogene-Quaternary reactivation of the Malta Escarpment as a result of the Nubia-Eurasia collision (Bianca et al., 1999; Argnani and Bonazzi, 2005; Adam et al., 2000.). Other faults, such as the Alfeo Fault-System and the Ionian fault (Fig. 1.5, 1.9 - see also section 1.3) represent important features for the seismotectonics and geodynamics of western Ionian basin and in general for the Central Mediterranean (Gutscher et al., 2016; Polonia et al., 2016).

1.2.2. Central Mediterranean

The current geological and geodynamic setting of the Central-Mediterranean is the result of a long (and still ongoing) deformation history originated by the Nubia and Eurasia convergence started approximatively 80 Ma, during the late Cretaceous (Dercourt et al., 1986; Malinverno & Ryan, 1986; Dewey et al., 1989; Patacca et al., 1990; Boccaletti et al., 1990; Faccenna et al., 2001a). This convergence, at a rate of about 2 cm/yr, led to the subduction of the Tethyan oceanic crust beneath the Adria-Africa crust (Fig. 1.3) and the formation of back-arc basins (e.g. Black Sea and Caspian Sea – Decourt et al., 1986). The subsequent Europe-ward subduction (Fig. 1.3) of the Tethyan crust and the slab roll-back about 35 Ma, triggered the fragmentation of the European (Variscan) crustal margin. This led to the separation of a crustal block, constituted by the future Corsica-Sardinia and the AlKaPeCa (Alboran, Kabilies, Peloritani and Calabria – se GK, LK, Pe, Ca in Fig. 1.3a-e) blocks, and the formation (30-23 Ma) of back-arc basins (e.g., Liguro-Provençal basin, - Cherchi & Montandert, 1982; Burrus, 1984; Beccaluva et al., 1989; Gorini et al., 1993, 1994; Lonergan & White, 1997; Malinverno & Ryan, 1986). The opening of the Liguro-Provençal back-arc basin resulted in oceanic spreading starting from late Aquitanian (23-21 Ma, Burrus, 1984; Gorini et al., 1993, 1994; Seranne, 1999) in response to the counterclockwise rotation (≈ 25° - Speranza et al., 2002) and migration of the Sardinia-Corsica block toward SE (21-16 Ma, Fig. 1.3a, b - Van Der Voo, 1993; Faccenna et al., 2001a). This stage of back-arc extension known as “the *Balearic stage*” (Lentini et al., 2006) led the Sardinia-Corsica block to collide with the Africa-Adria margin producing stacked

crustal units. Due to the residual Ionian subduction, the back-arc extension shifted, since the late Miocene, toward the SE, involving a further fragmentation of the southeastern portion of the "migrating" continental block (the *Tyrrhenian stage* – Lentini et al., 2006); this led to the opening of the Tyrrhenian basin (13-11 Ma, Fig. 1.3b, c - Mattei et al., 2002; Milia and Torrente, 2014) and consequent migration of the Calabrian-Peloritani block toward the SE (Kasten and Mascle, 1990; Sartori 1990; Faccenna et al., 2001a; Jolivet et al., 2015; Prada et al., 2018; Stampfli et al., 2002; Van Hinsbergen et al., 2014). The ESE-ward movement of Calabrian-Peloritani block (Nubia fixed) has significantly slowed down but is still active (≈2 mm/yr) as documented by GPS measurements (Fig. 1.3e - D'Agostino et al., 2004, 2011; Palano et al., 2012).

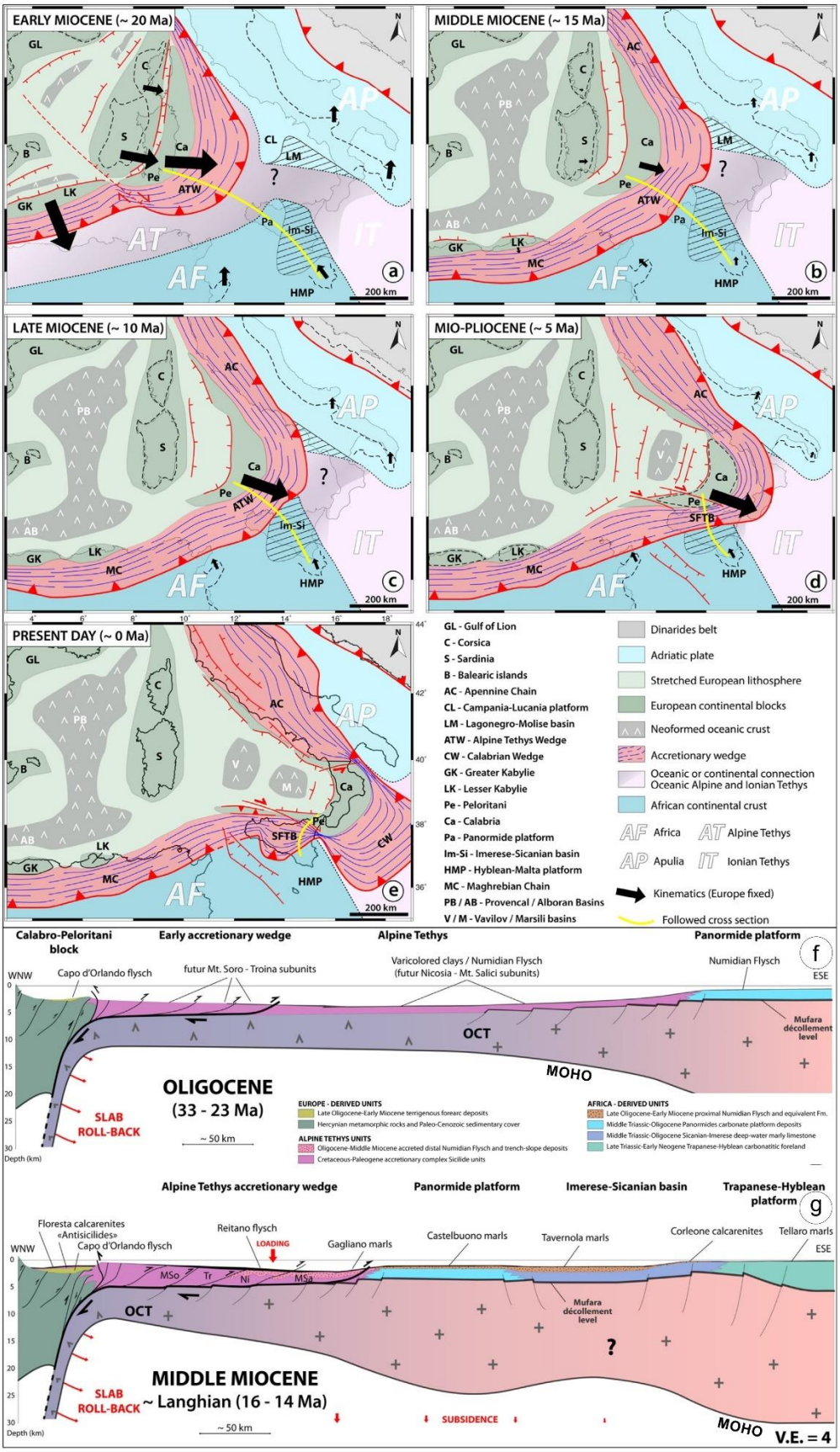

Figure 1. 3. a-e) Paleo-tectonic reconstruction of centre-western Mediterranean from early Miocene to present-day (mod. after Henriquet et al., 2020). Section views of the Oligocene (f) and middle Miocene (g) tectonic reconstruction of the Europe-Africa collision from Mesozoic to Pleistoce (mod. after Henriquet et al., 2020).

Nowadays, this long deformation history, dominated by the roughly N-S Nubia-Eurasia collision, depicts a quite complex geodynamic setting resulting in a suture zone. The whole Italian peninsula and Sicily Island represent a small emergent portion of a wider collisional suture belt, which extends from the Gibraltar strait to Anatolia (and still farther). It is characterized by two curved belts (Fig. 1.2b) or "Oroclines" (sensu Carey, 1955 – see also Marshak, 2004; Cifelli et al., 2007, 2008). The first one represented by the Alps-Appennines (in Norther and Central Italy) and the second one formed by the Southern Apennines, Calabro-Peloritanes Arc and the Sicilian Maghrebides (Southern Italy - Van Hinsbergen et al., 2020). In Sicily and southern Italy, the collisional belt is sandwiched between an old (Mesozoic), partially subducted oceanic crust (the Ionian crust) to the SE, and a recent (Neogene-Quaternary) one (the Tyrrhenian basin) to the NW (Lentini et al., 2006). In this particular collisional belt, it is possible to schematize three distinct structural domains: the Hinterland, the Orogenic and the Foreland domains (Fig. 1.4). In the following, the three domains are threated in detail with particular emphasis on the Sicily area.

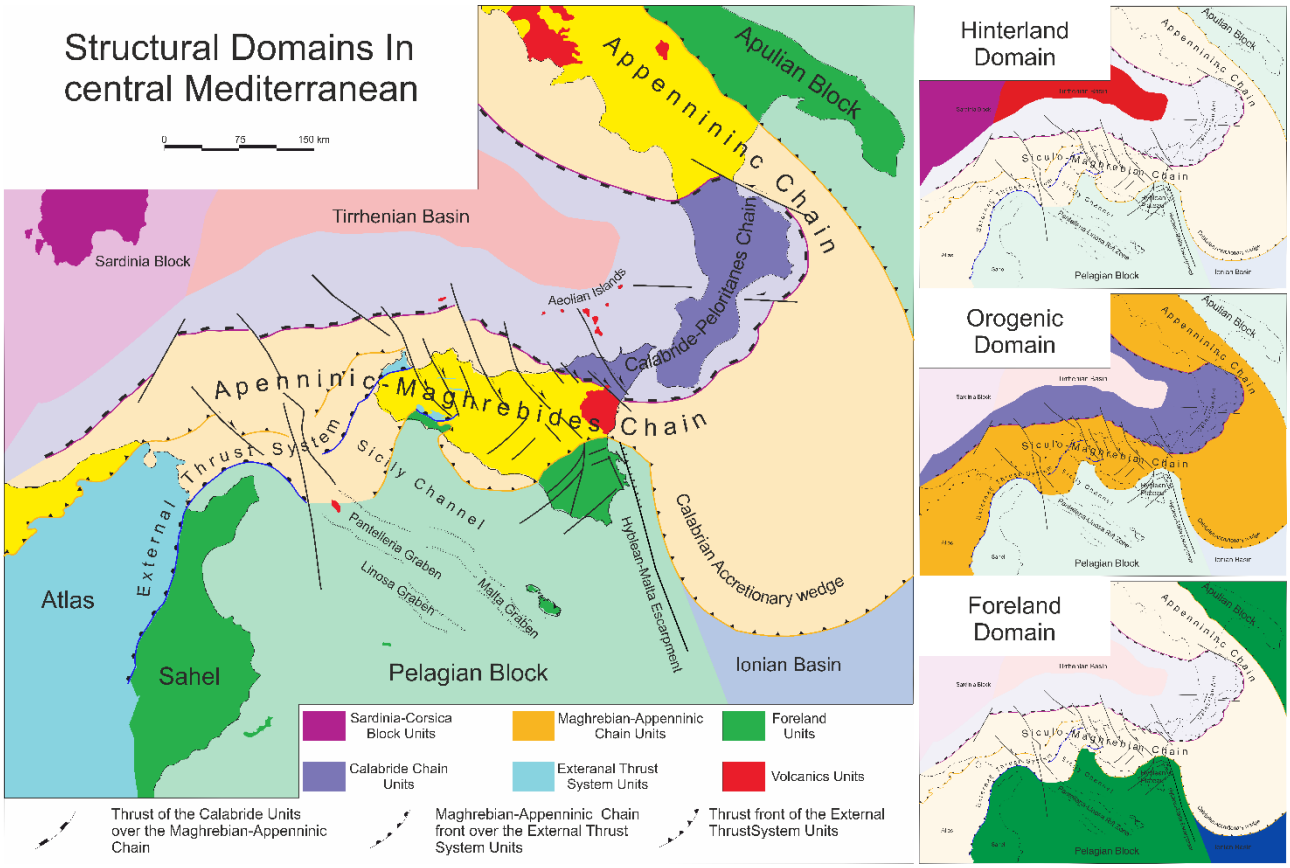

Figure 1. 4. Structural domains of central Mediterranean region. The collisional system consists of three well defined domain (from the most internal one): i) the Hinterland domain representing the fragmented/migrated European margin, ii) the Orogenic domain represented by three distinguished belt (see text) and iii) the Foreland domain consisting of the Pelagian block, Apulian block and Ionian basin (mod. after Lentini et al., 1996, 2006).

1.2.3. The Hinterland domain

The Hinterland domain is represented by the Sardinia-Corsica block and Tyrrhenian basin (Fig. 1.4), whose origin is related to the intraplate fragmentation of the European margin (Dewey et al., 1989). Even though the Calabrian-Peloritani terrains are genetically related to the Sardinia-Corsica block, they cannot be considered part of the Hinterland domains since they migrated SE-ward during the last 12 Ma and are now stacked above the Sicilian-Maghrebides chain (Lentini et al., 2006; Sartori 1990; Faccenna et al., 2001a; Jolivet et al., 2015).

The Sardinia-Corsica block is a ≈30 km-thick, continental portion characterized by a Variscan, high-pressure to high-temperature, metamorphic basement intruded by multiple granitoid plutons (Casini et al., 2012; Van Hinsbergen et al., 2020). The basement is covered by Permian to Cenozoic, continental to carbonate sediments and by Neogene volcanics (Carmignani et al., 2004). The Sardinia-

Corsica crust has experienced contractional deformation during the late Oligocene-early Miocene (Balearic stage – Lentini et al., 2006) which was then overtaken by extensional tectonics during late Miocene-Pliocene (Tyrrhenian stage). The CROP-Mare seismic lines (Finetti, 2004; Finetti et al., 2005a, 2005b) clearly show East-dipping normal faults (Tyrrhenian stage) on the Eastern margin of the Sardinia-Corsica block, cross-cutting the stacked nappes produced during the compressional phase (Balearic stage).

To the east of the Sardinia-Corsica block is the 10 km-thick oceanic crust of the Tyrrhenian basin (Fig. 1.4), whose extension started 13-11 Ma (Mattei et al., 2002; Milia and Torrente, 2014 – see above). During its spreading stage, the extension centered on localised volcanic spreading centres (tholeiitic affinity), such as the Vavilov (5-4 Ma) and Marsili (3-2 Ma) volcanoes (Kasten & Mascle, 1990; Sartori, 1990). At this stage, the extension occurred during Pliocene-Pleistocene is estimated at ≈300 km, resulting in a fast-rate up to 6 cm/yr (Faccenna, et al., 2001b; Rosenbau and Lister, 2004). This high-rate contrasts with the lower 1.5-2 cm/yr rate (extension of 150 km) estimated for the Northern Tyrrhenian (Faccenna, et al., 2001b, 2004; Rosenbau and Lister, 2004). Simultaneously to the Tyrrhenian extension, the NE-SW trending, arc-related volcanism migrated toward the SE reaching the current configuration of the Aeolian volcanic arc (Faccenna et al., 2001a). Nowadays, the southern Tyrrhenian sector is characterized by the Quaternary volcanic activity (both extinct and still active) related to the subduction of the northwest-dipping Ionian oceanic crust (Malinverno and Ryan, 1986; Doglioni, 1991; Gvirtzman and Nur, 1999; Faccenna et al., 2001a). This activity (firstly tholeiitic, then calc-alcaline and finally potassic on the active Stromboli and Vulcano islands, Peccerillo et al., 2013; De Astis et al., 2013 and references therein) started about 1-1.3 Ma and formed seven volcanic islands (the proper Aeolian islands – Fig. 1.4) and six seamounts. Farther to the west there is the Ustica-Anchise alignment (Na-alcaline to calc-alcaline volcanics) which is interpreted as intra-plate (Ustica) and subduction related (Anchise Seamount) volcanism (Trua et al., 2003; Argnani and Savelli, 1999; Schiano et al., 2004)

Along the offshore area of northern Sicily and of the southern Apennines, seismic lines outlined the presence of a 22 km-thick continental crust which has been interpreted as the Panormide-Apenninic block (Lentini et al., 2002), a crustal sector covered by Mesozoic-Cenozoic, shallow-water carbonatic sequence and located during the Mesozoic between two oceanic crusts (the Tethys to the N and the Ionian-Imerese-Lagonegrese Basin to the S – Fig. 1.3f, g). This crustal block is currently moving toward the south (Europe referred) and colliding to the African margin. Result of this convergence in Sicily is a system of NW-SE trending, right-lateral shear faults known in literature as the "South Tyrrhenian System" (Finetti et al., 1996) affecting the northern sector of the island both offshore and onshore (Fig. 1.4).

1.2.4. The Orogenic domain

The Orogenic collisional system in Central Mediterranean is an arc-shaped belt running along the Italian peninsula and connecting to the African Maghrebian belt through Sicily (Fig.1.5, 1.6). This curved orogenic system has experienced rotational deformation (on the vertical axis) due to the progressive SE-ward migration of the Calabrian-Peloritanes block (Fig. 1.3, 1.5 - Faccenna et al., 1996, 2001a; Catalano et al., 2004). Rotation up to 100° (clockwise for the Sicilian belt and counterclockwise for Southern Apennines - Speranza et al., 2003), in fact, led to the current E-W (Sicily) and NW-SE (southern Italy) orientation of the orogeny.

In Sicily, the orogenic system consists of three main tectonic domains related to different crustal and paleo-environmental settings which are, nowadays, stacked one above each other due to the 300-km of shortening experienced since Miocene (Faccenna, et al., 2001b; Rosenbau and Lister, 2004). The three domains are (from the structurally highest one): the Calabride-Peloritanes chain, the Apenninic-Maghrebian chain and the External Thrust system (Lentini et al., 2006).

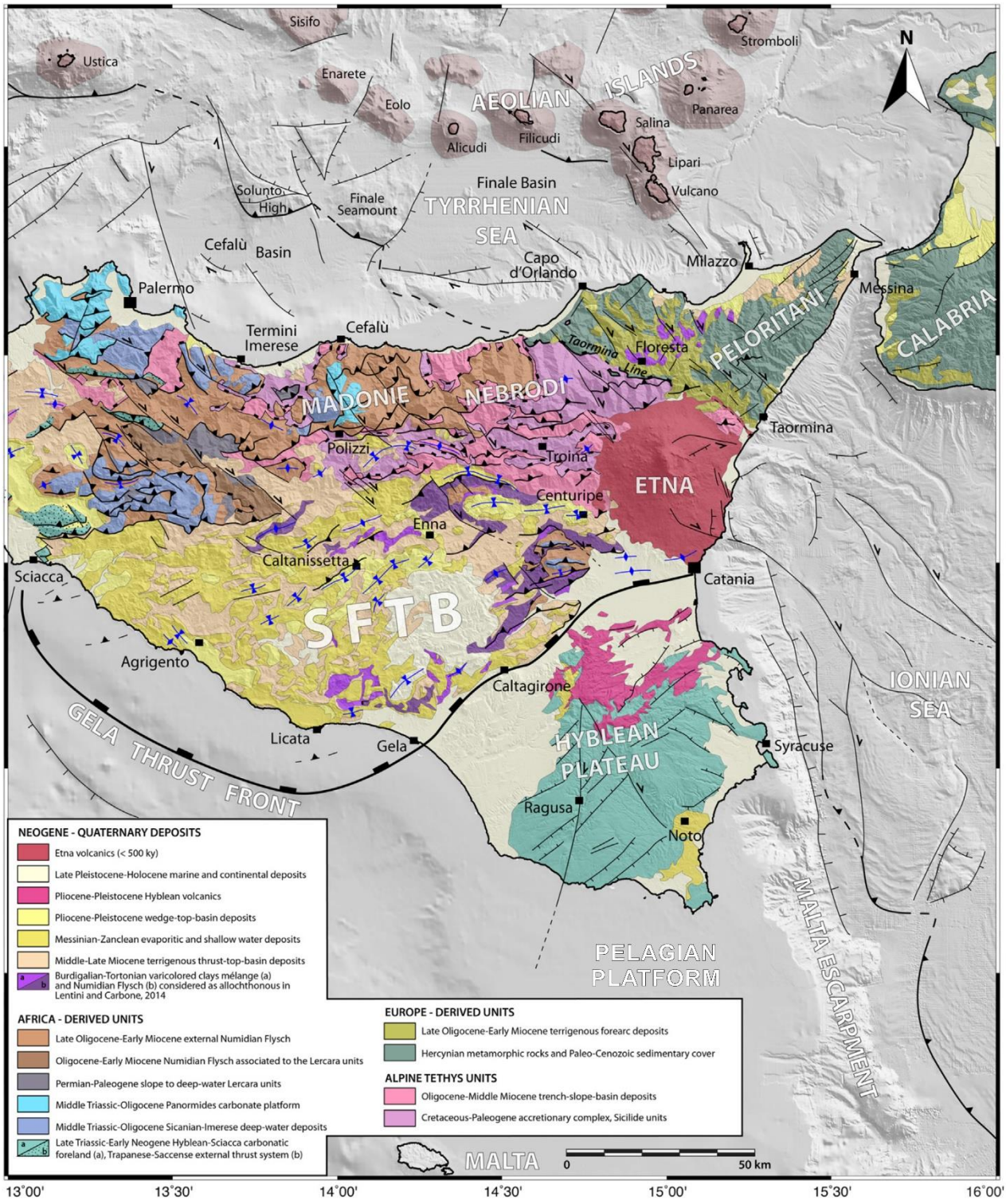

Figure 1. 5. Geological-Structural map of central-eastern Sicily. (mod. after Henriquet et al., 2020).

The ***Calabride-Peloritanes*** chain (known in literature with various names such as *Calabride-Peloritani Orogen, Calabride-Peloritani Arc* or *Kabilo-Calabride chain* – Boccaletti et al., 1984; Del Ben, 1993; Lentini et al., 1994, 1995; Monaco et al., 1996; Barca et al., 2010) interrupts the continuity of the Apennines chain (Fig. 1.4). The current geologic-structural setting of the Calabride-Peloritani

chain is mostly the result of Palaeozoic orogenic processes (Hercynian), overprinted by the Alpine-Apennine and strike-slip tectonics. These latter phases partially affected the Mesozoic ocean-derived units and sedimentary cover as well, producing a local metamorphic overprint (Cirrincione et al., 2008; Fazio et al., 2008). It consists, therefore, of exhumed, un-rooted, alloctonous crystalline nappes, belonging to the fragmented European southern margin (Sartori 1990; Faccenna et al., 2001a; Lentini et al., 2006; Jolivet et al., 2015) with relicts of their Mesozoic-Cenozoic sedimentary cover. Thrusting mainly developed because of buttressing of the Calabrian accretionary wedge and has been accompanied by the slab roll-back, back-arc extension of the Tyrrhenian basin and the subsequent SE-ward migration of the Calabride-Peloritani Arc. The outcropping terranes are located in Calabria and NE Sicily and are bounded by the Pollino fault zone (Northern Calabria) and by the Taormina line (Sicily - Ghisetti and Vezzani, 1982). It extends to the Kabyle chain (Algeria) through the offshore Tyrrhenian sector of Sicily and the Sicily Channel (Lentini et al., 1994, 2006). It is further subdivided in various tectonic units, but it can be schematized in three main tectonics complexes (from base to top): 1) Mesozoic (slightly metamorphic) carbonate platform sequences (Basal Complex), 2) oceanic-derived units (Liguride and Sicilide Complex), locally metamorphosed by HP/LT conditions and 3) an upper portion (Calabride Complex) representing an almost complete continental crustal section (Cirrincione et al., 2015 and refences therein).

The ***Apenninic-Magrhebian chain***, locally known as the ***Sicily Fold and Thrust Belt*** (SFTB, Fig. 1.5 - Barreca and Monaco, 2013; Catalano et al., 2013) lies in an intermediate structural position within the orogenic domain and it is overlain by the Calabride-Peloritani chain. It consists of imbricated sedimentary sequences belonging to various paleo-environmental setting both of oceanic (Alpine Tethys and Ionian basin) and continental affinity (Panormide platform located between the two oceanic basins). This belt is further subdivided in three tectonic units (from base to top): Ionides Unit, Panormide Platform Unit and Alpine Tethys (or Sicilides) Unit (Lentini et al., 1995, 2006). The *Ionides Unit* (also known as Imerese Unit) is composed of Mesozoic-Cenozoic, pelagic sedimentary

sequences deposited on the Ionian Paleo-basin grading to Oligocene-Miocene terrigenous successions. It is well exposed in western Sicily and buried in Eastern Sicily except for an embricated stack outcropping to the SW of Mount Etna (Mt. Judica Unit). The Ionides unit underwent compression and thrusting from Miocene to Pliocene (Lentini et al., 2006). The *Panormide Platform Unit* consists of Mesozoic-Cenozoic sedimentary deposits with Platform or transitional (Platform-Basin) facies with a Tertiary, clay-sandstone cover (Lentini and Vezzani, 1974). This facies variability (shallow to pelagic) testifies the topographic/bathymetric control exerted by the Jurassic opening of the Neotethys (Nigro and Renda, 2002; Distefano et al., 2002). This unit crops out in western Sicily (Palermo) while it is buried in the eastern sector. The *Alpine Tethys Unit* (known as *Sicilide* – Ogniben, 1960) consists of alloctonous terranes deposited on the most internal oceanic domain (Tethys Ocean) close to the crustal European margin. This unit has undergone compression since Oligocene-Miocene (Finetti et al., 1996) and due to its plasticity and high "mobility" (mainly clayey deposits) the sequences travelled from the internal position as far as the most advanced front of the chain (Gela Nappe) (Henriquet et la., 2020).

The ***External Thrust System (ETS)***, which takes the names of *Pelagian-Sicilian Thrust Belt* (in Sicily) and *Apulian Thrust System* (in Southern Italy), is the lowermost (outermost) element of the orogenic system (Fig. 1.4). It is produced by the detachment of the basin-ward margin of the Pelagian Foreland domain (Lentini et al., 1996). It is well exposed in western Sicily (between Trapani and Sciacca – Lentini Carbone, 2014). Moreover, its northward and eastward continuity is testified by seismic lines (Lentini et al., 2002; Finetti et al., 2005b). The unit consists of Triassic-early Jurassic platform limestones, overlain by middle Jurassic-early Oligocene pelagic limestones followed by continental-epicontinental Oliocene-Miocene deposits. The deformation of the External Thrust System started in late Miocene (Tortonian) due to the Tyrrhenian Basin opening (Mattei et al., 2002; Milia and Torrente, 2014).

1.2.5. The Foreland domain

The foreland represents the slightly deformed continental margin, on which the tectonic nappes overthrust (Fig. 1.4 - Ben Avraham et al., 1990; Lentini et al., 1994, 2006; Henriquet et al., 2019). It currently includes the Apulian Block (Southern Italy), the Pelagian block (Southern Sicily and Sicily Channel) and the Ionian basin (Fig. 1.4). The outermost margin of the Pelagian foreland has been involved in the contractional processes since late Miocene and today constitutes the External Thrust System (see above).

The Pelagian block (Fig. 1.4, 1.6) extends from Northern Africa (Tunisia) to Sicily (Sciacca and Hyblean Plateau) through the Sicily Channel (Finetti, 1982; Burollet et al., 1987; Boccaletti et al., 1989; Reuther, 1989; Argnani, 1990) and represents the flexured Northern portion of the Africa (Nubia) plate. It is characterized by ≈ 30 km continental crust (Burollet, 1991; Scarascia et al., 2000) and a Mesozoic-Cenozoic, carbonatic (shallow-water to deep-water) cover intercalated by volcanic products (Patacca et al., 1979; Bianchi et al., 1987; Grasso et al., 2004). In the central portion of the Pelagian block, the Sicily Channel (Fig. 1.4) is a large extensional basin whose deformation is the result of flexuration of the Nubia plate beneath the collisional belt (Dewey et al.,1989). The extensional crustal thinning (since Neogene – Finetti,1984; Argnani, 1993; Civile et al., 2010) has given rise to three sub-parallel rift zones (Pantelleria, Linosa and Malta grabens – Fig. 1.4). The area has been characterized by alkaline to peralkaline, anorogenic, volcanic activity since Pliocene-Pleistocene (with oldest products dated at Tortonian time – Beccaluva et al., 1981; Calanchi et al, 1989; Corti et al., 2006; Rotolo et al., 2006).

1.2.6. The Hyblean Plateau

The Hyblean Plateau (hereafter HP), along with the Sicily Channel, represent the emergent (HP) and submerged (Sicily Channel) portions of the Pelagian Block (Fig. 1.4, 1.6, 1.7); a foreland domain in the Northern portion of the African (i.e., Nubia) plate margin (Burollet et al., 1978; Ben-Avraham and Grasso, 1991). It is bounded by two main structural features, which are integrated in

the Nubia-Eurasia plates collision: 1) the SFTB front bounding the Western and Northern sides and 2) the Hyblean-Malta Escarpment (or Malta Escarpment) to the East (Fig. 1.4).

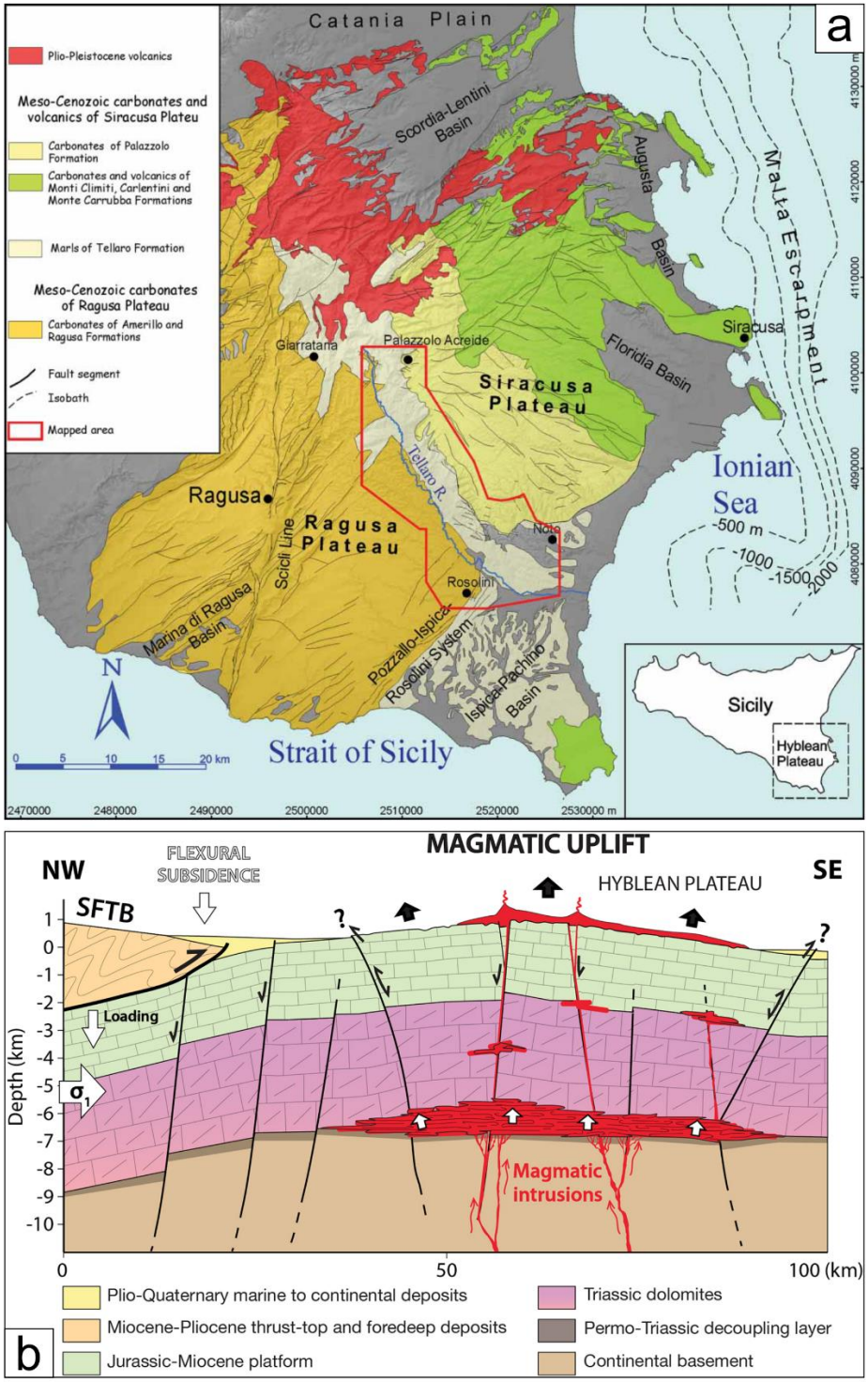

Figure 1. 6. a) Geological-Structural map of the Hyblean Plateau (SE Sicily). (From Romagnoli et al., 2015). b) N-S schematic cross-section showing magmatic intrusion (responsible for the "dome shape") and volcanic activity in the Hyblean area (from Henriquet et al., 2019)

The northward continuity of the Hyblean Plateau is detected (by mean of geophysical data) under the Apenninic-Maghrebian collisional front, as far as the Etnean area (Fig. 1.6b - Cristofolini et al., 1979; Lentini, 1982; Bianchi et al., 1987; Ben-Avraham and Grasso, 1991). To the south, the HP opens toward the Sicily Channel, where an intraplate, dextral, shear-zone has given rise to rifting processes (pull-apart) within the foreland of the Nubia-Eurasia collision (Finetti et al., 1984; Boccaletti et al., 1987; Cello et al., 1985; Reuther and Eisbacher, 1985; Ben-Avraham et al., 1987; Reuter et al., 1993; Coltelli et al., 2016).

The north-western down-bending of the HP under the collisional chain (SFBT) is covered by Plio-Quaternary sediments of the Catania-Gela foredeep (Fig. 1.6b - Ogniben, 1969; Butler et al., 1992). The elevated topography of HP has been interpreted for long time as a positive forebulge (*sensu* Jordan et al., 1995) due to the orogenic chain (SFTB) load (Billi et al., 2006; Cogan et al., 1989; Pedley & Grasso, 1992). This hypothesis supported by crustal profiles (Lentini et al., 2005, 2007; Accaino et al., 2011; Catalano et al., 2012, 2013) is not consistent with the non-cilidrical, dome-shaped geometry of the Hyblean Plateau. The dome geometry, highlighted by the radial drainage system and the positive magnetic and gravimetric anomalies of HP (Milano et al., 2020), led Henriquet et al. (2019) to propose mafic sill intrusion as a plausible tectono-magmatic process to explain the HP dome shape (Fig. 1.6b). In addition, the interaction of magmatic intrusion and inherited crustal structures are invoked to explain the multiple faults systems (see section 1.3.1) observed within the HP. In this context, recent strike-slip fault systems (such as the Scicli-Ragusa fault) are clearly related to the ongoing regional collision (Cultrera et al., 2015).

Nowadays, the uplifted topography of HP prevents under-thrusting below the SFTB. As a result, the HP behaves like an indenter causing later extrusion of the chain. This process explains the arc-shaped curvature of the belt (SFTB) to the east and west of the Hyblean Plateau (Tapponnier, 1977; Mantovani et al., 1993; Adam et al., 2000; see Fig. 1.4).

The Hyblean continental affinity has been interpreted on the basis of crustal thickness (≈25 km – Finetti, 1982; Cassinis, 1983; Dewey et al., 1989; Scarascia et al., 1994) and correlation with drilled crystalline rocks (Precambrian granites and metamorphic rocks) observed in Tunisia (Burollet, 1991). Otherwise, no evidence of such rocks has been found in the Hyblean area, where the only direct evidence of crustal basement is represented by ultramafic, mantle-related, volcanic xenoliths (Scribano et al., 2006). The 25-30 km thick Hyblean crust is capped by ~10 km of carbonate succession intercalated by volcanic products. The carbonatic sedimentary cover consists of a sequence of shallow- to deep-water Meso-cenozoic rocks (Patacca et al., 1979; Bianchi et al., 1987; Grasso et al., 2004) outcropping respectively in the eastern and western sector of the Hyblean Plateau (Grasso and Lentini, 1984). Quaternary deposits are generally preserved within structural depressions (Scordia graben, Augusta and Floridia depressions - Grasso and Lentini, 1984; Cultrera et al., 2015).The volcanic intercalations consist of mostly tholeiitic, sub-marine to sub-aerial products spanning from Cretaceous to Pleistocene time (Longaretti et al., 1991; Schmincke et al.,1997; Torelli et al., 1998; Rocchi et al., 1998; Behncke, 1998) largely outcropping in a N-S alignment along the Ionian coast (Carbone et al. 1984, 1986). The Pliocene magmatic activity is mainly located in the northwestern portion of HP. Late Pliocene is marked by a rapid variation in the chemical composition from mafic alkaline to tholeiitic; this change is coeval to the development of NE-SW trending normal faults and related to NW collapse of HP during the formation of the foredeep (Schmincke et al. 1997; Behncke, 2001). The presence of volcanic products buried under the Catania Plain sediments testifies that Hyblean volcanism shifted northward towards the Etnean area (Longaretti et al. ,1991; Branca et al., 2004, 2007).

1.2.7. Ionian Basin

As part of the foreland domain, the Ionian Basin separates the two continental blocks of the same domain: the Apulia and the Pelagian blocks (Fig 1.5, 1.8).

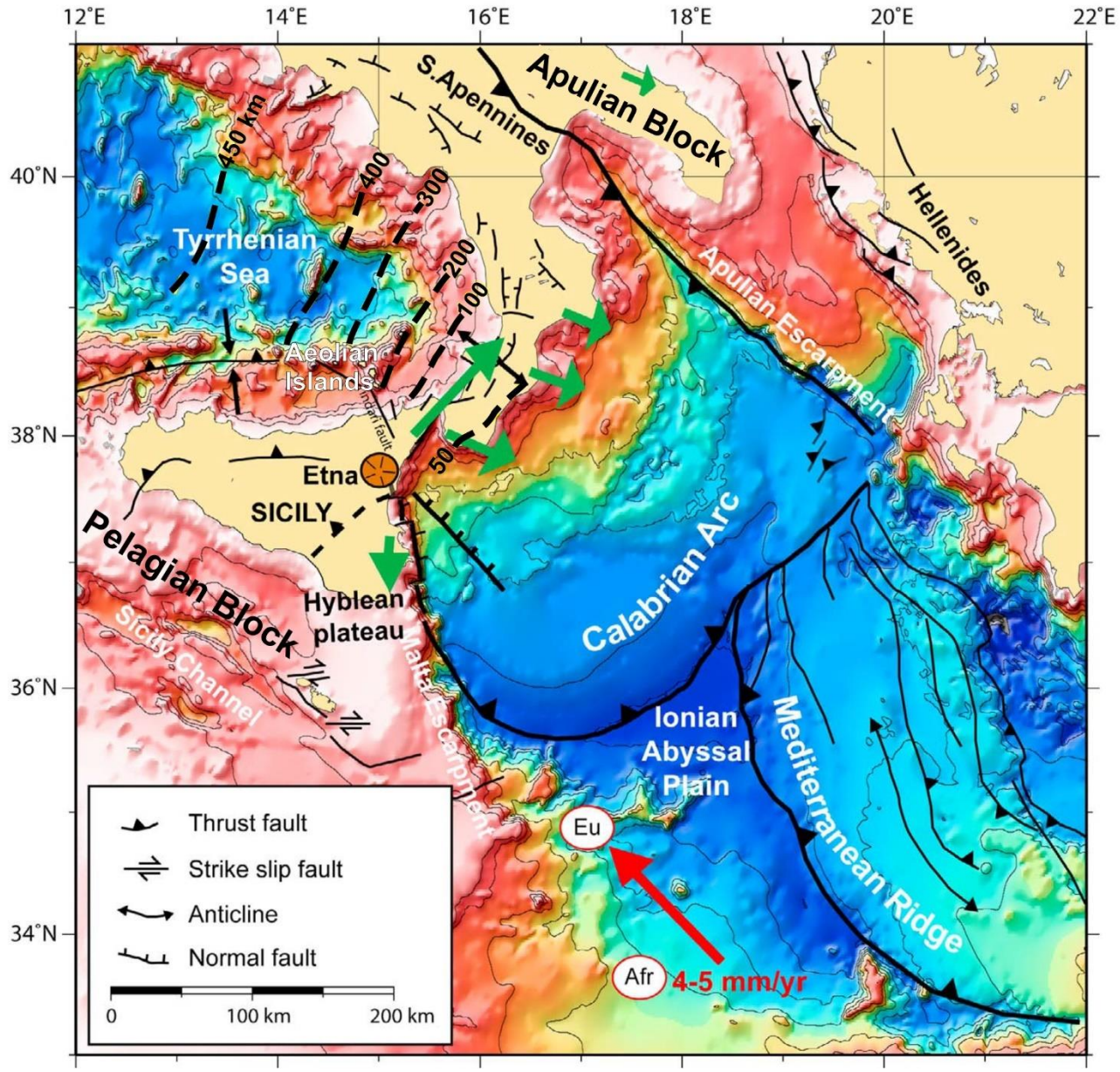

Figure 1. 7. Bathimetry and Geodynamic setting of the Ionian Sea. Green arrows indicatethe GPS vectors (Apulian block fixed), red arrows indicate the Africa motion with respect to Europe. Dotted lines indicate the slab depth. (Mod. after Polonia et al., et al., 2011)

Located eastward of the Hyblean Plateau (Pelagian Block), the Ionian Basin is sandwiched between two subduction zones (Dannowski et al., 2019); the Ionian subduction (Barreca et al., 2019 also known as Calabrian subduction - Polonia et al., 2011, or Southern Tyrrhenian subduction – Selvaggi and Chiarabba, 1995; Bianchi et al., 2016) to the northwest and the Hellenic subduction (Mediterranean Ridge in Fig. 1.7) to the southeast (Le Pichon et al., 1982; Hatzfeld et al., 1993). To the north, the presence of an active subduction slab (the Ionian subduction) is supported by volcanic activity (i.e., Aeolian Islands, Fig. 1.5, 1.7 – Malinverno and Ryan, 1986; Doglioni, 1991; Gvirtzman

and Nur, 1999; Faccenna et al., 2001a), seismic data (CROP line – Finetti, 2004; Finetti et al., 2005b) and seismologic data (Scarfì et al., 2013, 2016, 2018; Calò et al., 2012). Despite the 25-30 km-thick crust characterizing the HP (11-17 km thick crust and 5-7 km sedimentary cover - Hinz, 1974; Makris et al., 1986; Ferrucci et al., 1991; de Voogd et al., 1992), the nature of Ionian Sea has been debated for a long time. Numerous works, since the '70s have been developed in order to clarify whether it is characterized by oceanic (Finetti and Morelli, 1973; Rossi and Sartori, 1981; Finetti, 1982; Finetti et al., 1996, 2005b; Mascle and Chaumillon, 1998; Stampfli et al. 1998; Catalano et al., 2000, 2001; Polonia et al., 2002; Reston et al., 2002; Dellong et al., 2018) or thinned continental crust (Farrugia & Panza 1981; Calcagnile et al. 1982; Cernobori et al. 1996). Moreover, values of 130 and 250 mGal (gravity anomaly) in the Ionian abyssal plain which decrease to 20- 30 mGal toward the Calabrian front, together with low heat flow values (30-40 mW m^{-2}) (Della Vedova & Pellis, 1989) suggested an oceanic crust of early Mesozoic age. Anyway, many other uncertainties and disagreements still persist about the Ionian age. Different authors attributed it to different ages: Permian (Vai, 1994; Finetti, 2004), Permian-Triassic (Finetti, 2004; Argnani and Bonazzi, 2005; Speranza et al., 2012), or Jurassic (Finetti et al., 1996; Catalano et al., 2000; Tugent et al., 2019).

Nowadays, the oceanic-crust hypothesis is generally accepted, and the Ionian abyssal plain should represent the remnant of the Mesozoic Tethys Ocean (Speranza et al., 2012; Dannowski et al, 2019) opened in Permian-Trissic times. In this view, the Hyblean-Pelagian platform has the significance of a passive continental margin (Catalano et al., 2000, 2001) currently separated from the subducting Ionian abyssal plain by a STEP fault (Argnani, 2000, 2009; Argnani and Bonazzi, 2005; Govers and Wortel, 2005; Gallais et al., 2013; Gutscher et al., 2016).

In the northwestern Ionian basin, an active accretionary wedge (Calabrian Accretionary Wedge), deriving from the Ionian lithosphere subducting underneath Calabria (to the northwest), overthrusts the Ionian abyssal plain (Catalano and Sulli, 2006; Gallais et al., 2012). The wedge consists of a stack of sedimentary units originally deposited above the Ionian crust (Finetti, 1982,

2004; Valenti, 2010). The wrench basal *décollement* coincides with Messinian sequences that accommodate the deformation maintaining the underlying portion undeformed (Catalano et al., 2001; Cuffaro et al., 2019).

1.3. Tectonic Setting

1.3.1. General overview

The tectonic framework of the study area is the result of a long-lasting process and related interaction of tectonic blocks in the central Mediterranean since Mesozoic times (Lentini, 2006; Catalano et al., 2006; Dellong et al., 2018; Henriquet et al., 2020) with recent rearrangement in Neogene-Quaternary times (Barberi et al., 1973; Malinverno and Ryan, 1986; Dewey et al., 1989; Boccaletti et al., 1990; Patacca et al., 1990; Gueguen et al., 1998; Dellong et al., 2018).

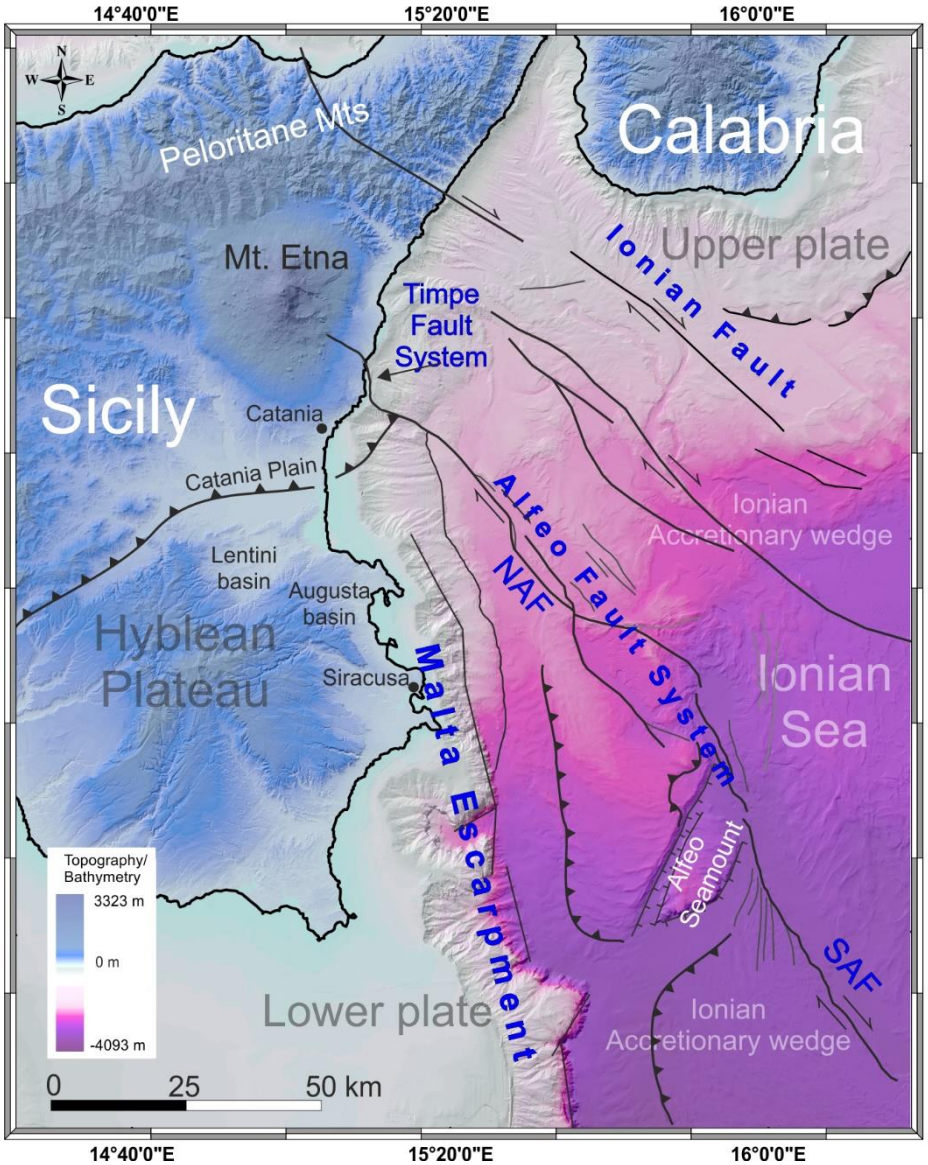

Figure 1.8. Main structural features of eastern Sicily and western Ionian basin. NAF and SAF indicate the two portions of the Alfeo Fault System (also known as Alfeo-Etna Fault - Polonia et al., 2016) North Alfeo Fault and the South Alfeo Fault respectively (Gutscher et al., 2016). Modified after Gambino et al. (2021).

This latter time span is characterized by the N-S oriented, Nubia-Eurasia plates convergence. As a result, the structural context of the western Ionian and south-eastern Sicily is rather complex due to different deformation processes affecting the emergent and submergent areas (Fig. 1.4).

The main tectonics features in the study area are represented by the internal Hyblean faults systems (on shore), the Malta Escarpment (hereafter MESC) and the strike-slip tectonic structures affecting the Calabrian accretionary wedge (Alfeo Fault System and Ionian Fault, Fig. 1.5, 1.9).

The abovementioned structures play an important role on the geodynamics and seismotectonics of the area, but their current tectonic significance within the complex setting of the Ionian subduction zone is still matter of study. Still unclear is their relationship with the Ionian subduction. The MESC was thought to be a STEP fault (sensu Govers and Wortel, 2005) by various authors (Argnani, 2000, 2009; Argnani and Bonazzi, 2005) until Gallais et al. (2013) proposed a 50 km-offshore, NNW-SSE trending structure previously mapped by many authors (Cernobori et al., 1996; Minelli and Faccenna, 2010; Nicolich et al., 2000; Polonia et al., 2011) which may have formed at the transition between continental crust and thinned continental crust. Afterwards, Gutscher et al. (2016), proposed the North-Alfeo fault and the South-Alfeo fault (the two segments of the Alfeo Fault System) as the tectonic expression of a STEP fault in the Ionian Sea which approximatively corresponds to that one proposed by Gallais et al. (2013). It is worth noting that the original STEP acronym (Govers and Wortel, 2005) indicating "Subduction-Transform Edge Propagators" has been renamed (by Gutscher et al., 2019) as "Subduction Tear Edge Propagator" which is more suitable since it includes scissor-like kinematics. More recently, Barreca et al. (2019) proposed another candidate as a STEP fault in the Ionian Sea, extending north-westwards the previously proposed Ionian fault (Polonia et al., 2011, 2016). Combining field and seismological data, the authors mapped a regional-scale, dextral strike-slip fault slicing across the entire NE corner of Sicily and documenting its prolongation (SE trending) in the Ionian Sea.

In the following lines these main features are described separately.

1.3.2. Hyblean Plateau

The Hyblean plateau shows an internal diffuse network of variously oriented, normal- to strike-slip faults (Fig. 1.6a, 1.8, 1.9). Its structural setting derives from the combination of flexuration processes, response to the main horizontal stress and inherited Mesozoic structures (Grasso and Reuter, 1988) and Cenozoic evolution (Henriquet et al., 2019). Due to its crustal thickness (25-30 km) and prominent relief, the Hyblean Plateau resists to under-thrusting beneath the SFTB orogenic nappes and behaves as an indenter with respect to the advancing collisional front.

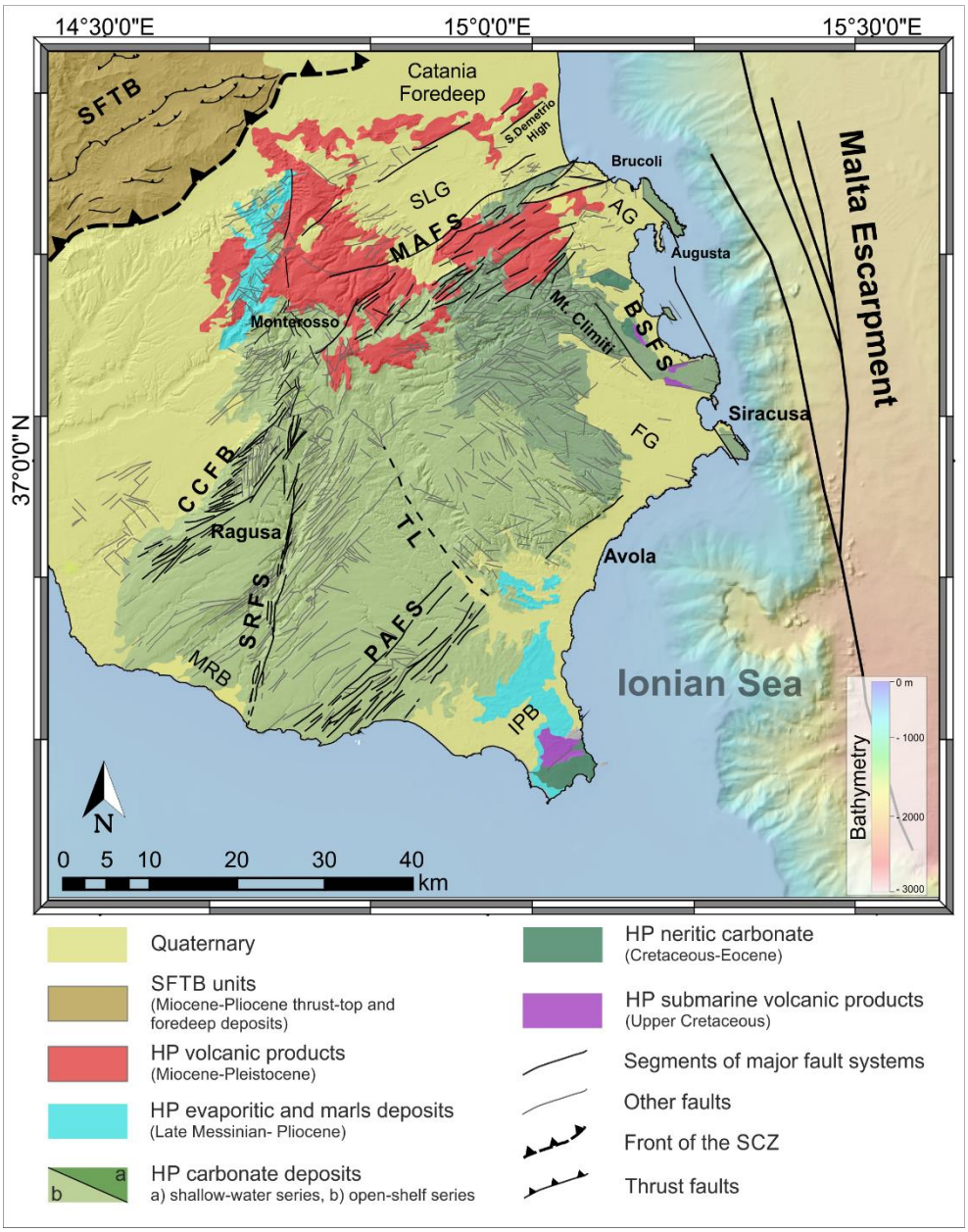

Figure 1.9. Main structural features of the Hyblean Plateau. SFTB, Sicilian Fold and Thrust Belt; SLG, Scordia-Lentini Graben; AG, Augusta Graben;FG, Floridia Graben; BSFS, Brucoli–Siracusa Faults System; MAFS, Monterosso–Agnone Fault; SRFS, Scicli–Ragusa

Faults System; PAFS, Pozzallo–Avola Faults System; TL, Tellaro Line; MRB, Marina di Ragusa Basin; Ispica-Pozzallo Basin (mod. after Carbone et al., 1987).

Three main fault systems cutting through the Hyblean Plateau can be schematised: 1) the NE-SW oriented extensional fault system, cutting the NW and SE sector of the plateau (MAFS, CCFB and PAFS in Fig. 1.6, 1.9), 2) the N-S trending, Scicli-Ragusa Fault (SRFS), 3) the NNW-SSE trending faults in the Eastern coastal sector (Brucoli-Siracusa Fault System, BSFS).

The first group includes the Monterosso-Agnone fault system (MAFS) in the northern sector of the HP, the Comiso-Chiaramonte fault belt (CCFB) in the southwestern sector and the Pozzallo-Avola fault system (PAFS) in the southeastern sector (Ghisetti and Vezzani, 1980; Cogan et al., 1989; Grasso et al., 2000; Cultrera et al., 2015; Henriquet et al., 2019). These NE-SW fault systems are sub-parallel to the front of the Sicilian Fold and Thrust Belt (SFTB) and are interpreted as the result of the north-westward down bending of the Hyblean Plateau beneath the SFTB (Billi et al., 2006; Cogan et al., 1989; Pedley & Grasso, 1992). In the northern and western sector (MAFS and CCFB), the NW-ward collapse of these normal fault systems caused the formation of the sub-parallel Gela-Catania foredeep, and the extensional deformation favoured the emplacement of Pliocene-Quaternary volcanics characterising the northern sector of the Hyblean Plateau (Schmincke et al. 1997; Behncke, 2001; Henriquet et al., 2019). The MAFS, CCFB and PAFS Quaternary activity have given rise to the formation of NE-SW oriented horsts and grabens such as the Scordia-Lentini graben and the S. Demetrio high (to the North), the Marina di Ragusa basin (MRB, to the SW) and the Ispica-Pachino basin (IPB, to the SE). On the southern sector, one of the major faults of the NE-SW system is the 20 km-long Avola fault, whose activity is estimated to have occurred in the last 400 kyr (Bianca et al., 1999).

The Scicli-Ragusa Fault (SRFS in Fig. 1.6, 1.9) is a regional, NNE-SSW trending shear zone, formed in Plio-Pleistocene time with right-lateral kinematics (Ghisetti and Vezzani, 1980; Grasso and Reuter, 1988; Ben-Avraham and Grasso, 1990). It has been recently (0.85 Ma, see further) reactivated with left-lateral kinematics in the context of the Nubia-Eurasia convergence and its deformation rate

varies from 1.2-1.4 mm/yr to 0.5 mm/yr respectively in its northern and southern sectors (D'Agostino and Selvaggi, 2004; Montone et al., 2004; Serpelloni et al., 2007; Catalano et al., 2008; Mattia et al., 2012; Musumeci et al., 2014). The roughly 70 km-long fault trace of the Scicli-Ragusa is not continuous but rather segmented and it possibly extends southwards in the offshore (Gardiner et al., 1995). Structural, seismological, and geodetic observations reveal the inversion from right to left-lateral kinematics in the last 0.85 Ma, when it has been active with a rate of 1.3 mm/yr (Bousquet and Lanzafame, 2004; Catalano et al., 2006; Musumeci et al., 2005; Lavecchia et al., 2007; Mastrolembo Ventura et al., 2014). However, no clear offset is observed in outcrops.

The eastern sector of the HP is controlled by normal to oblique, NNW-SSE, east-dipping faults (Brucoli-Siracusa fault system, BSFS). These faults are considered to be associated with the Malta Escarpment structures located 20 km offshore (see below). Their recent activity is testified by the presence of grabens filled by Quaternary marine deposits (Augusta and Floridia grabens – Bianca et al., 1999). In the central part of the Hyblean Plateau, another NW-SE trending fault has been recently mapped by Romagnoli et al. (2015): the Tellaro fault. This polyphase, left-lateral, tectonic structure separates the Hyblean Plateau into the Siracusa and the Ragusa domain (Ghisetti & Vezzani, 1980; Grasso & Lentini, 1982; Pedley & Grasso, 1992). It represents a crustal discontinuity which played an important role in the post-Tortonian evolution of the HP (Romagnoli et al., 2015) accommodating the relative motions between the Ragusa and Syracuse domains of the Hyblean Plateau.

1.3.3. Malta escarpment

To the East, the Hyblean Plateau is bordered by the Malta Escarpment, a 300-km long crustal discontinuity giving rise to a bathymetric drop of about 3,000 m. It marks the transition between the Pelagian platform and the oceanic Ionian Basin (Fig. 1.4 - Finetti 1985; de Voogd et al., 1992; Catalano et al., 2000; Gallais et al., 2013; Dellong et al., 2018) and its formation is related to the Permo-Triassic crustal stretching (Sengör, 1979) and subsequent Jurassic–Cretaceous spreading stage (Ben-Avraham and Grasso, 1991; Catalano et al., 2001; Gallais et al., 2011; Dellong et al., 2018).

Successively it has been reactivated in the context of the Neogene convergence between Nubia and Eurasia plates (Torelli, 1998; Catalano et al., 2000). Nowadays, the Malta Escarpment marks the transition "Continent-Ocean" separating two sectors of the African plate with different crustal thickness/rheology: 1) the 25-30 km thick, continental-like Hyblean Plateau to the West, and 2) the 8-10 km thick, oceanic Ionian basin (Dellong et al., 2018).

The Plio–Quaternary activity of Malta Escarpment fault system is characterized by oblique extension (Scandone et al., 1981; Fabbri et al., 1982; Casero et al., 1984; Bianca et al., 1999; Argnani & Bonazzi 2005; Palano et al., 2012; Gambino et al., 2021a), even though the late Quaternary kinematics is still debated. Neotectonics observations (Adam et al., 2000) and seismological data (Amato et al., 1995; Musumeci et al., 2014) suggest that onshore structures related to the MESC fault system are characterized by left-lateral kinematics. Conversely, regional-scale geodynamic studies (e.g., Bianca et al., 1999; Doglioni et al., 2001), seismological (Presti et al., 2013) and geodetic data (Mattia et al., 2012; Palano et al., 2012) clearly indicate a right-lateral component for the Malta Escarpment fault system. In addition, diverging GPS vectors measured on the Hyblean and Adria blocks (Ward 1994; Mastrolembo et al., 2014; D'Agostino and Selvaggi, 2004; Grenerczy et al., 2005), indicates an ESE–WNW-oriented crustal extension (internal to the foreland domain). In this geodynamic context, the NNW–SSE oriented MESC kinematics should result oblique (right-lateral transtensional). Recently, marine seismic profiles revealed active tectonic extension along the northern sector of the Malta Escarpment; anyway, its strike-slip component remains still poorly-constraints (Argnani and Bonazzi, 2005; Argnani et al., 2012; Gambino et al. 2021a).

The MESC was thought to be a STEP fault (sensu Govers and Wortel, 2005) by various authors (Grivtzman & Nur, 1999; Doglioni et al., 2001; Argnani, 2000, 2009; Argnani and Bonazzi, 2005). Recently, other fault systems, located in the Ionian Sea, has been interpreted as STEP (see below).

1.3.4. Calabrian Accretionary Wedge, Alfeo Fault System, and Ionian Fault

To the east of the Malta Escarpment is the Calabrian Accretionary Wedge (CAW) whose Western portion is affected by dextral strike-slip kinematics. The Calabrian Accretionary Wedge has developed mainly offshore even though a small portion crops out in eastern Calabria (Figs. 1.3, 1.5). Its internal deformation is localised in a thick Mesozoic-Cenozoic sedimentary sequence including Messinian evaporites. The CAW is divided into three morpho-structural domains (Polonia et al., 2011) depending on the position of the basal thrust with respect to the Messinian evaporites: 1) post-Messinian accretionary wedge (frontal sector), 2) pre-Messinian clastic accretionary wedge (intermediate position) and 3) the inner plateau (Fig. 1.10). The different rheology and deformation styles of such domains have resulted in the formation of major faults zones cutting through the CAW. These fault zones are represented by the Ionian Fault (Polonia et al., 2011, 2016) and the Alfeo Fault (Gutscher et al., 2016 – also known as Alfeo-Etna Fault, Polonia et al., 2016). Both faults were considered good candidate to play the role of STEP in relation to the roll-back of the Ionian slab (Gallais et al., 2013; Gutscher et al., 2016, 2017, 2019; Polonia et al., 2011, 2016; Barreca et al., 2019; Maesano et al., 2020), but the debate about the exact position of the STEP is still open. Polonia et al. (2016) considered the Alfeo faults as the offshore counterpart of the right-lateral deformation affecting the NE Sicily (the Tindari Fault System - Billi et al., 2006a; Barreca et al., 2019), with the Ionian fault being the only plausible STEP fault. Conversely, other authors support the Alfeo Fault as a Subduction Tear fault (Gallais et al., 2013; Gutscher et al., 2016, 2017; Dellong et al., 2018; Maesano et al., 2020).

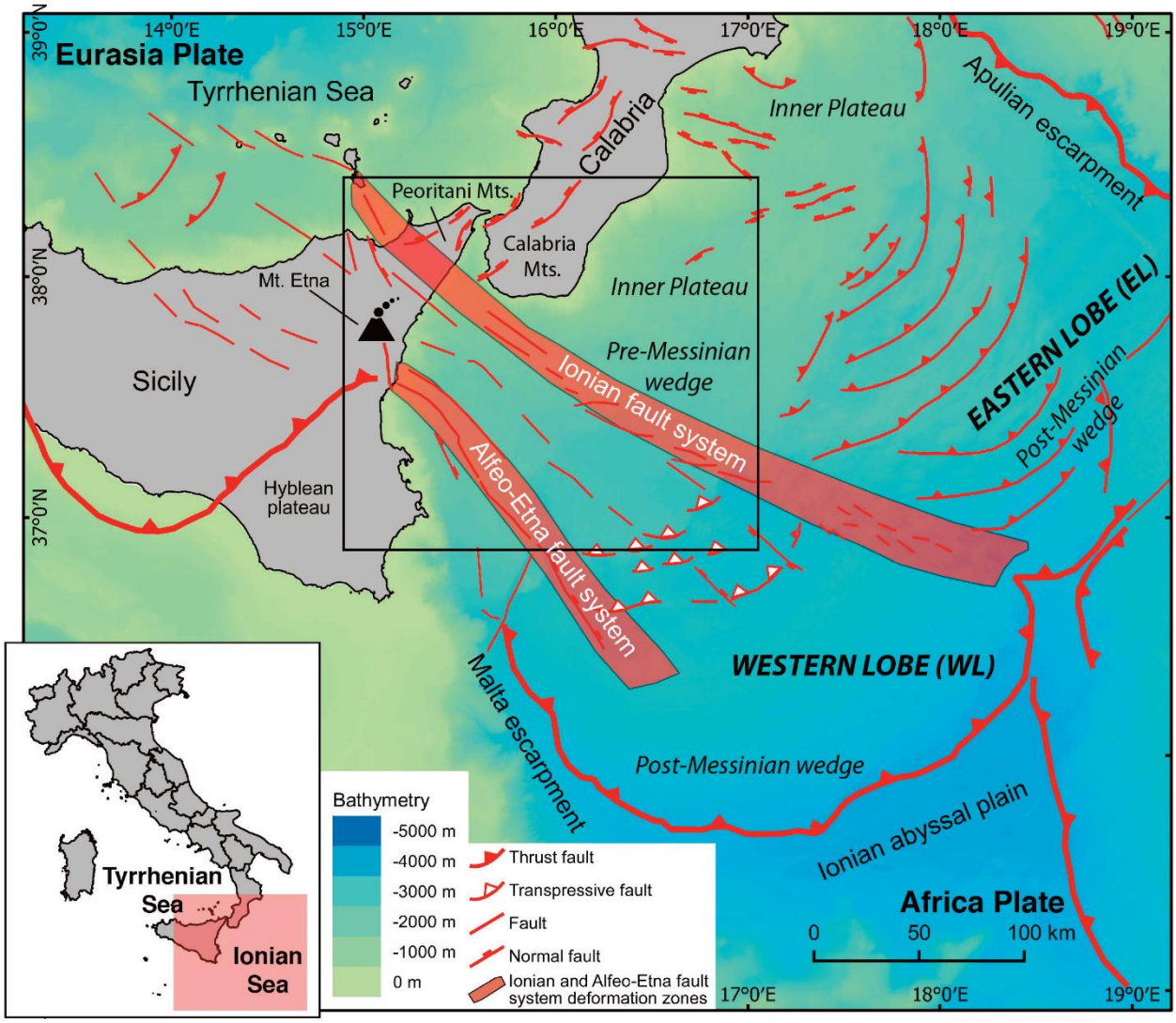

Figure 1.10. Tectonic setting of the western Ionian basin showing the internal subdivision of the Calabrian Accretionary Wedge and strike-slip structures of Alfeo-Etna Fault System (or Alfeo Fault System – Polonia et al., 2016 and Gutscher et al., 2016 respectively). From Billi et al., 2020.

Whatever the geodynamic significance of these structures, both Alfeo and Ionian faults represent important structural features for determination of seismic hazard in western Ionian basin, together with the reactivated portion of the Malta Escarpment.

Apart from these contrasting interpretations, the Ionian fault divides, with right-lateral kinematics, the Calabrian Accretionary Wedge in two different lobes: the eastern and the western lobe (Polonia et al., 2011, 2012). The main difference between the two lobes is the depth of the basal thrust, which is deeper in the eastern and shallower in the western lobe; this is reflected in a different structural style (higher and steeper topography in eastern lobe and smoother in the western lobe) and a higher deformation rate of the eastern lobe with respect to the western one. This also implies that

the Ionian fault represents a lateral ramp of the CAW, active since Messinian times. The actual deep crustal nature of the Ionian fault is not universally accepted since it seems limited to the sedimentary cover (Dellong et al., 2018) and the bathymetric morphology in that area seems to rule out the possibility of dextral motion (see Gutscher et al., 2017, 2018).

The Alfeo Fault (Gutscher, 2016, Fig. 1.8; also known as Alfeo-Etna Fault, Polonia et al., 2016, Fig 1.5) is a NW-SE trending, right-lateral strike-slip fault extending for about 140 km from the offshore of Mt. Etna (to the NW) to the SE of the Alfeo Seamount (a subsided segment of the Hyblean Plateau – Sartori et al. 1991) (Fig. 1.8, 1.11). For some authors (Palano et al., 2012; Polonia et al., 2016), the Alfeo Fault might be the result of regional scale lithospheric deformation connecting the thrust zone along the northern margin of Sicily with the Calabrian subduction, which gives rise to a dextral shear corridor including the Etna volcano and segments of the Malta Escarpment. The tensional component results from the regional strain field associated with Africa–Eurasia relative motion. For other authors (Gallais et al., 2013; Gutscher et a., 2016, 2017; Dellong et al., 2018; Maesano et al., 2020) the Alfeo fault is, instead, the bathymetric expression of a STEP fault related to the NW-dipping, retreating Ionian slab. The right-lateral kinematics of NAF has been obtained by earthquake focal mechanisms (Palano et al., 2012; Musumeci et al., 2014) and morpho-bathymetric expression and seismic profiles (Gutscher et al., 2016), and from submarine scuba-diving observations (Chiocci et al., 2011). Gutscher et al (2016) divide the Alfeo fault in 1) South Alfeo Fault (SAF) and 2) North Alfeo Fault (NAF) segments, respectively south and north of the Alfeo Seamount (Fig. 1.8).

The SAF (Fig. 1.8) is an 80 km-long, N150° trending E-dipping fault with normal component of motion. It is thought to have a prevalent dextral component, which resulted in the formation of associated elongated, Pliocene-Quaternary syntectonic pull-apart basin and separates two portions of the Calabrian wedge (Fig.1.7).

The 60 km-long NAF marks the separation between the Calabrian Accretionary wedge (to the East) and the undeformed area (here called Turbidite Valley) between the NAF and the MESC (Maesano et al., 2020). Along its entire bathymetric trace, the NAF appears both as a discrete single fault line and as a zone of various sub-parallel segments (Gutscher et al., 2016), especially to the South where it merges into the SAF. The single line portions show clear indication of right-lateral kinematic related to the fault trace bending (such as pull-a-part basin). Similarly, the segmented portion shows dextral features (such as left-stepping en-echelon geometry). To the North, the NAF approaches the Ionian coastline and interrupts the Malta Escarpment (Fig. 1.5, 1.8, 1.10). This segment matches with the dextral shear fault mapped up to 15 km offshore the Etnean coastline (Chiocci et al., 2011). Onshore, NAF connects to the N-S trending normal faults ('Timpe fault system' located on the eastern sector of Etna - see Barreca et al., 2018), forming a releasing-bend zone (Monaco et al., 2021).

1.4. Seismicity and Seismotectonics

1.4.1. Seismicity

The western Ionian basin (including southern Calabria and eastern Sicily) is one of the seismically most hazardous area of the Italian peninsula and, in general, one of the most active of Central Mediterranean (Azzaro and Barbano, 2000). The area has been struck by large damaging events with magnitude exceeding 7, such as those of 4 February 1169, 11 January 1693, 5 February 1783 and 28 December 1908 (Tinti et al., 2001; Barbano et al., 2001; Piatanesi and Tinti, 1998; Rovida et al., 2016; Barreca et al., 2021). The instrumental seismicity of the last 30 years (Musumeci et al., 2014) depicts a low to moderate seismic zone characterized by earthquakes magnitude in the range of 1.0 – 5.4 (period 1990-2013). Most energetic events are located along the Ionian coast (Brancato et al., 2009 and references therein) among which the Mw=5.4 December 13th, 1990 (see Fig. 1.12), earthquake. Hypocentral depth ranges between 5-25 km for the HP and 10-30 km for the coastal sector of western Ionian basin (De Lorenzo et al., 2004; Musumeci et al., 2014).

Analysis of recent seismicity allowed to recognize the Hyblean Plateau (HP) as a segmented foreland portion (Musumeci et al., 2014 – Fig. 1.11). The Scicli-Ragusa Fault System (SRFS) and the Malta Escarpment (MESC) behave as tectonic boundaries accommodating most of the deformation of the HP and resulting in blocks segmentation. In particular, the SRFS separates the HP in two blocks (western and eastern blocks), while the MESC marks the transition to the Ionian Basin (Musumeci et al., 2014). In the western block, a low seismicity mostly occurs along the SRFS. Fault plane solutions clearly show strike slip kinematics and maximum compression oriented roughly NNW-SSE (Musumeci et al., 2014), suggesting a left-lateral motion of the SRFS; this data fit with previous results obtained by borehole breakout (Ragg et al, 1999; Montone et al., 2012), geodetic data (D'Agostino and Selvaggi, 2004; Palano et al., 2012; Mattia et al., 2012) and structural data (Monaco and Tortorici, 2000; Catalano et al., 2008; De Guidi et al., 2013; Gambino et al., 2021a). In the eastern block, the seismicity is mainly located south of the Monterosso-Agnone Fault System (MAFS in Fig.

1.6, 1.9) and along the Ionian coastal sector (Cultrera et al., 2015). To the southeast, seismicity is almost absent beyond of the Pozzallo-Avola Fault System (PAFS in Fig. 1.6, 1.9), and the high V_P/V_S ratio detected in the area has been interpreted as a high crack density zone (Musumeci et al., 2014). This hypothesis agrees with the low stress drop (0.1-10 bar) observed in the area (De Lorenzo et al., 2004), suggesting the presence of various faults and/or a weakened zone which avoids stress accumulation. These observations along with field survey led Cultrera et al. (2015) to propose the central sector of the HP as a transfer zone between the MAFS and the PAFS.

To the north, the seismicity deepens down to 40 km, accordingly to the NW-ward underplating of the HP (Sgroi et al., 2012; Musumeci et al., 2014). Conversely, a very few events occurred in the Scordia-Lentini area in the last 20 years (Musumeci et al., 2014), where active tectonic and inversion have been observed (Bousquet and Lanzafame, 2004; Catalano et al., 2008). It is still unclear whether this is due to a seismic gap (and so, high seismic hazard) or to a low seismic efficiency (De Guidi et al., 2015).

1.4.2. Historical events

Moderate to major earthquakes hit the area in both pre-instrumental (mostly) and instrumental times (Fig. 1.11, 1.12). Most destructive historical events with (estimated) magnitude above 7.0 are commonly located along the eastern Sicily coastal area: the earthquake of 4 February **1169** (south-eastern Sicily; estimated M≈7.3, Tinti et al., 2001; Barbano et al., 2001), the earthquakes of 9 and 11 January **1693** (southeastern Sicily; estimated M ≈ 7.2-7.3, Piatanesi and Tinti, 1998; Tinti et al., 2001; Barbano et al., 2001), the earthquake of 28 December **1908** (Messina strait; M=7.1, Platania, 1909; Mercalli, 1909; Barreca et al., 2021). Secondary events (Fig. 1.11, 1.12), even though with lower magnitude, heavily impacted the Hyblean area, such as those of 10 December **1542** (estimated M≈6.3), the 20 February **1818** (estimated M≈6.3), the 11 January **1848** (estimated M≈5.4) and the instrumentally registered event of 13 December **1990** (M=5.1; for a review of the above-mentioned events see Azzaro & Barbano, 2000 and refences therein). Historical chronicles associated most of

these events with tsunami effects (e.g., 1169, 1542, 1693, 1818, 1908, 1990, Tinti et al., 2004) providing information about their possible location in the Hyblean offshore or along the coastal area.

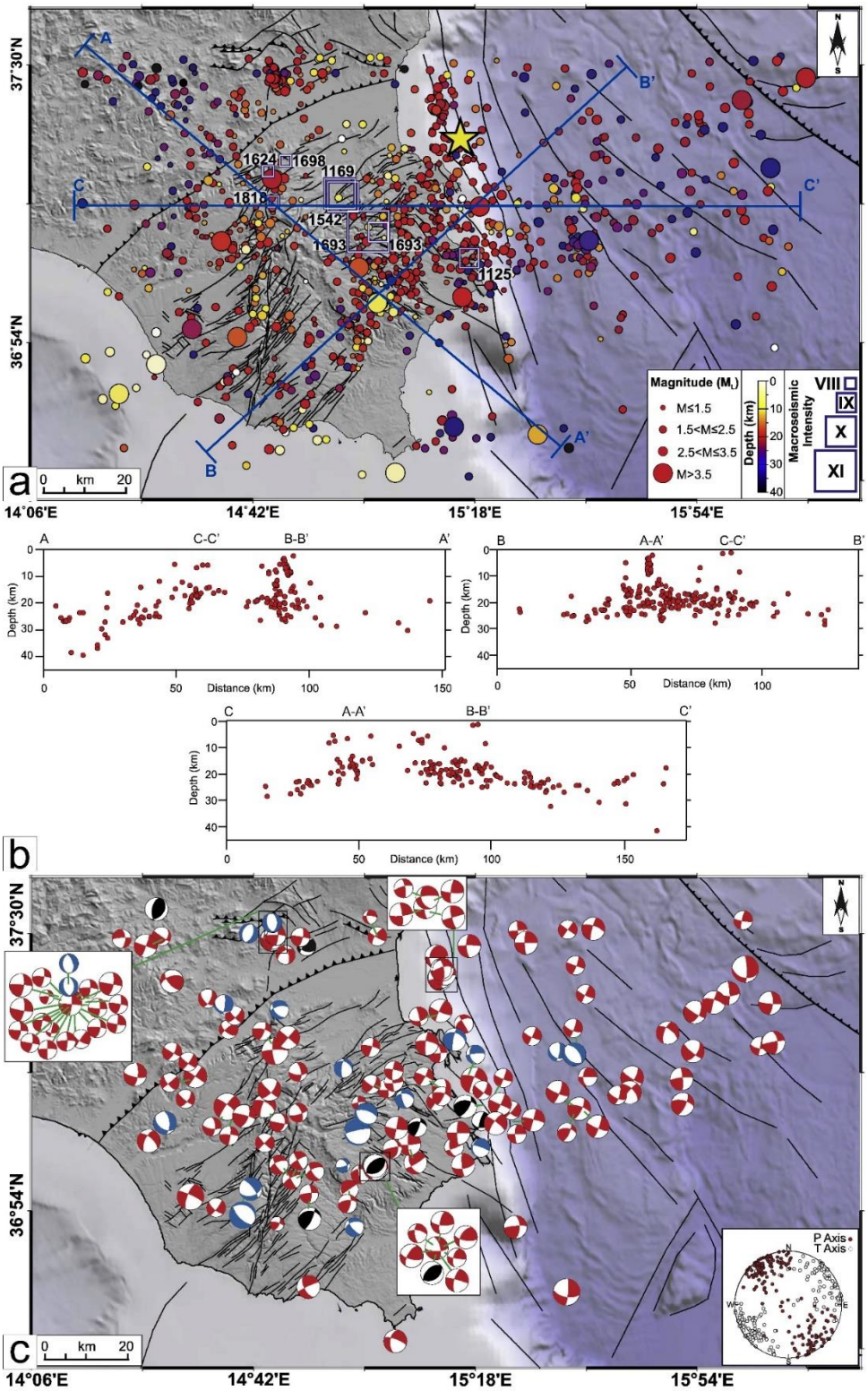

Figure 1.11. a) Earthquake locations (1994 to 2013) and inferred locations of historical earthquakes (Guidoboni et al., 2007). Star indicates the location of the 1990 earthquake (ML 5.4, Amato et al., 1995). b) Depth location of earthquakes in along the profile reported in the above figure. Faults and acronyms are shown in Fig. 1.9. c) Focal mechanisms of 165 selected earthquakes. The beach-balls colours indicate as follow: red, strike-slip fault; blue, normal fault; black, inverse fault (mod. after Musumeci et al., 2014).

To better depict a complete view of the historical seismicity and its effects on the study area, it is important to describe the main characteristics of the most destructive events as reported by coeval chronicles and report; the 1693 and the 1169 events.

The 1169 earthquake.

On 4 February 1169, a huge earthquake (estimated M≈6.8-7.3) struck the Eastern Sicily. Most of the damages were focused in the area of Catania, which was almost completely destroyed (Lombardo, 1985; Boschi et al., 1995a, b; Azzaro et al., 1999; Boschi and Guidoboni, 2001; Barbano et al., 2001). Other localities were severely damaged even though the scarcely documented reports and the scattered urbanization (at that time) provided limited indication for damage evaluation. The shock was felt on the entire eastern Sicily (as far as Messina). Syracuse was largely destroyed, accounting for more than 50-60% of buildings ruined. Estimated magnitude is not univocal due to the poor coeval description of the effects and ranges from M=6.8 (Barbano et al., 2001) to M= 7.3 (Azzaro et al., 1999; Tinti et al., 2001).

Only one coeval source reports tsunami effect (Ruggiero di Hoveden in Boschi and Guidoboni, 2001). The report describes a vertical sea retreat of about 5 m observed in Catania and Messina. The subsequent inundation involved the eastern coast of Sicily from Messina to the Simeto river (south of Catania) where a village (Casal Simeto) was devasted (Lombardo, 1985). In the area of Syracuse, variation of freshwater springs (some closed after the earthquake and new ones opened) were reported. Other permanent field effects were observed in in southeastern Sicily as far as Piazza Armerina (Enna).

The 1693 earthquake.

The January 1693 earthquake represents the most destructive event ever occurred in south-eastern Sicily. The main shock of January 11, with an estimated magnitude of 7.2-7.4 (Imax=XI, Fig. 1.13), impacted the entire eastern Sicily producing main damages in the areas of Catania and

Syracuse. It was preceded by the foreshock of January 9 (estimated M≈6.0), which strongly weakened the buildings before the devasting main shock (Barbano and Cosentino, 1981; Boschi et al., 2000). Damages involved more than 40 localities, 25 of them were flattened and some re-settled elsewhere (among which Noto, Avola, Grammichele, and partially Ragusa) and caused 60.000 casualties (Barbano et al., 1985; Boschi et al., 1995a). The earthquake was felt as far as Malta to the south and Messina to the north. In Catania, chronicles reported that only few buildings were left standing (Privitera, 1695; Boccone, 1697; Ferrara, 1829).

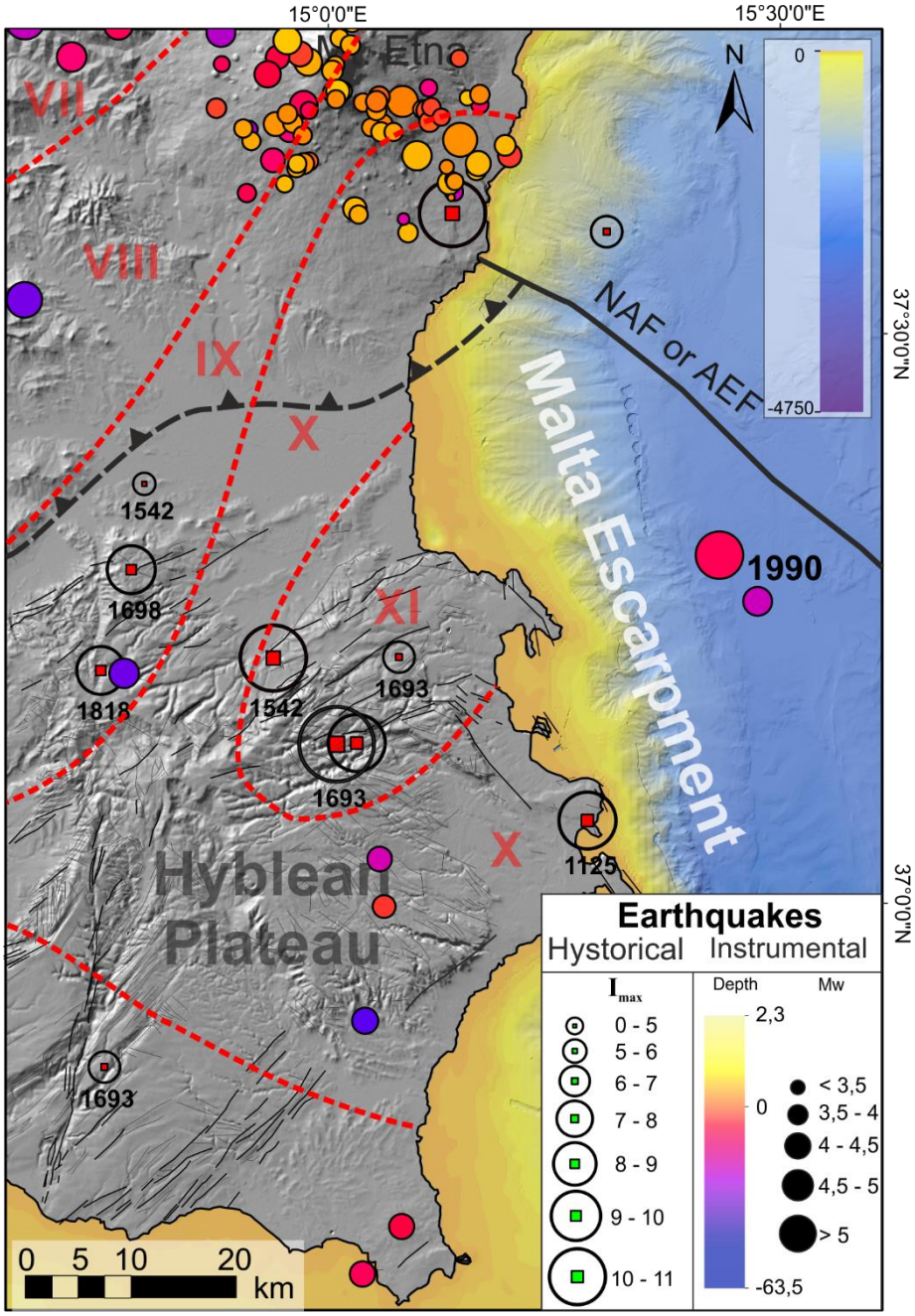

Figure 1.12. Hystorical (from CPTI 15, Rovida et al., 2016)earthquake and instrumental seismicity (M>2.5 events from1981 to 2014, http://istituto.ingv.it/index.php/it/archivi-e-banche-dati – see also Scarfi et al., 2018). Red dashed lines represent the isoseismal map of the January 11, 1693 earthquake by (Barbano, 1985).

Chronicles reported the occurrence of tsunami waves that devasted the coast from Syracuse to the straits of Messina and were felt as far as Malta and Aeolian islands (Tinti et al., 2001; Tinti et al., 2004 and references therein). However, there is no absolute consensus about the exact number of waves. Some authors indicate a double sea retreat (Boccone, 1697) which, locally, may have manifested with three waves (Boccone, 1697; Baratta, 1901). The amount of sea retreat is reported in ca 50 m (75 m at Siracusa, 37-45 m at Augusta, and 50 m at Messina) but locally (e.g., Mascali shore,

north of Catania) it was observed a retreat of up to 700-800 m (Boccone, 1697; Boschi and Guidoboni, 2001). The subsequent inundation penetrated in land with effects depending on bathymetry/topography and urbanization of the coastal area. Augusta underwent the major effects in terms of inundation (up to 150 m). The initial withdrawal (at the harbour) exposed the seafloor leaving the galleys of the Order of the Knights of Malta (at anchor) on the seafloor; the inundation, then, threw the galleys at the coast. In Catania, inundation was up to 350 m (Boccone, 1697; Boschi and Guidoboni, 2001) reaching the S. Filippo square (today called Mazzini square). In Mascali, water penetrated for about 1.5 km; such an inundation was likely favoured by the flat and lowered topography of the area at that time, occupied by swamps and protected by Quaternary dunes facing the coast, which could have acted as a dam.

1.4.3. Seismotectonics

Identification of seismic sources in southeastern Sicily and western Ionian Basin is a difficult task due to various factors such as the absence of instrumentally recorded large earthquakes, the geodynamic/tectonic framework and, the lack of clear Quaternary rupture surfaces (at least on land). Despite the available coeval reports (some detailed, some other approximative) relative to major historical earthquakes, the exact location of the involved seismic sources is still a matter of debate, particularly for the 1693 main shock. Based on macroseismic intensity map and geological data, potential on land sources include faults (MAFS in Fig.1.9) located within the ENE-WSW oriented Scordia-Lentini Graben (SLG in Fig. 1.9 - D'addezio and Valensise, 1991; Tinti and Armigliato, 2003), along the N-S Scicli Ragusa Fault System (SRFS in Fig. 1.9 - Sirovich and Pettenati, 1999; DISS Working Group, 2018) or along another N-S trending alignment in the eastern sector of the Hyblean Plateau (Pirrotta and Barbano, 2020). The 1693 earthquake intensity map (Fig. 1.13) proposed by Barbano et al. (1985) shows maximum intensity in the northeastern sector of the Hyblean Plateau (between Lentini and Augusta); moreover, isoseismal areas are elongated on a NE-SW direction and seems to validate the SLG as on land source. In addition, it has been observed (see

section 1.4.1 Seismicity) that this area represents a low-seismicity area (Musumeci et al., 2014), which can be due to the presence of a seismic gap related to a high return period (with consequent high seismic hazard). Nevertheless, the isolines are open toward the Ionian Sea (Barbano et al., 1985) and a possible offshore source between Catania and Augusta cannot be excluded. Similarities on the macroseismic fields and locations of 1169 and 1693 epicenters would suggest the same seismic source for the two earthquakes (Mulargia et al., 1985)

Other authors theorized a possible offshore source, located between Catania and Siracusa, which could explain the reported tsunami effects (Barbano, 1985; Camassi and Stucchi, 1997). Even though the hypothesis of an offshore source was accepted by some authors and supported by tectonic observation, seismic data and modelling, the proposed possible sources are not univocal. Proposed sources include the Malta Escarpment (Piatanesi and Tinti, 1998; Azzaro and Barbano, 2000; Argnani and Bonazzi, 2005; Bianca et al., 1999; Gambino et al., 2021a), and a locked subduction fault plane (Gutscher et al., 2006). In addition, the 60 km-long North Alfeo Fault (NAF), located about 30 km off the Ionian coast, is potentially capable (based on empirical relations, see Wells and Coppersmith, 1993 and Leonard, 2010) of generating earthquakes with magnitude exceeding 7. However, the strike-slip kinematic of the fault system is not compatible with the occurrence of the reported tsunami since the lack of vertical component of the slip would not disturb the sea surface.

2. Data and Methods

2.1. Overview

The seismic dataset consists of high-resolution seismic lines and bathymetry from distinct marine geophysical surveys. Interpretation, picking and elaboration of seismic data (3D modelling, stress analysis, 2D sequential restoration etc.) were performed using the MOVE geomodelling software package (Petex Ltd.). Field data were collected using mobile software (such as FieldMOVE and FieldMOVE Clino by Petex Ltd) and random checks (with classical approach using compass, clinometer etc.) were carried out to validate authenticity of data. Visualization (stereographic projection diagram) and analysis (stress inversion and pseudo-focal mechanisms) of field data (fault/fracture planes and kinematic indicators) were performed using Stereonet and Faultkin free software (Angelier, 1984; Marrett and Allmendinger, 1990; Allmendinger et al., 2012; Cardozo and Allmendinger, 2013).

2.2. Seismic reflection profiles

Seismic data consists of high-resolution profiles (both published and unpublished at the beginning of this PhD project) acquired in the frame of two distinct marine geophysical cruises: the CIRCEE-HR project (R/V le Suroît, October 2013, Gutscher et al., 2016) and the Poseidon POS496 (R/V Meteor, March-April 2016, Krastel, 2016). The dataset is schematised in Fig. 2.1, 2.2 and 2.3. Seismic profiles are characterized by a high resolution but a limited penetration (acoustic basement 3 sec TWT) for both datasets.

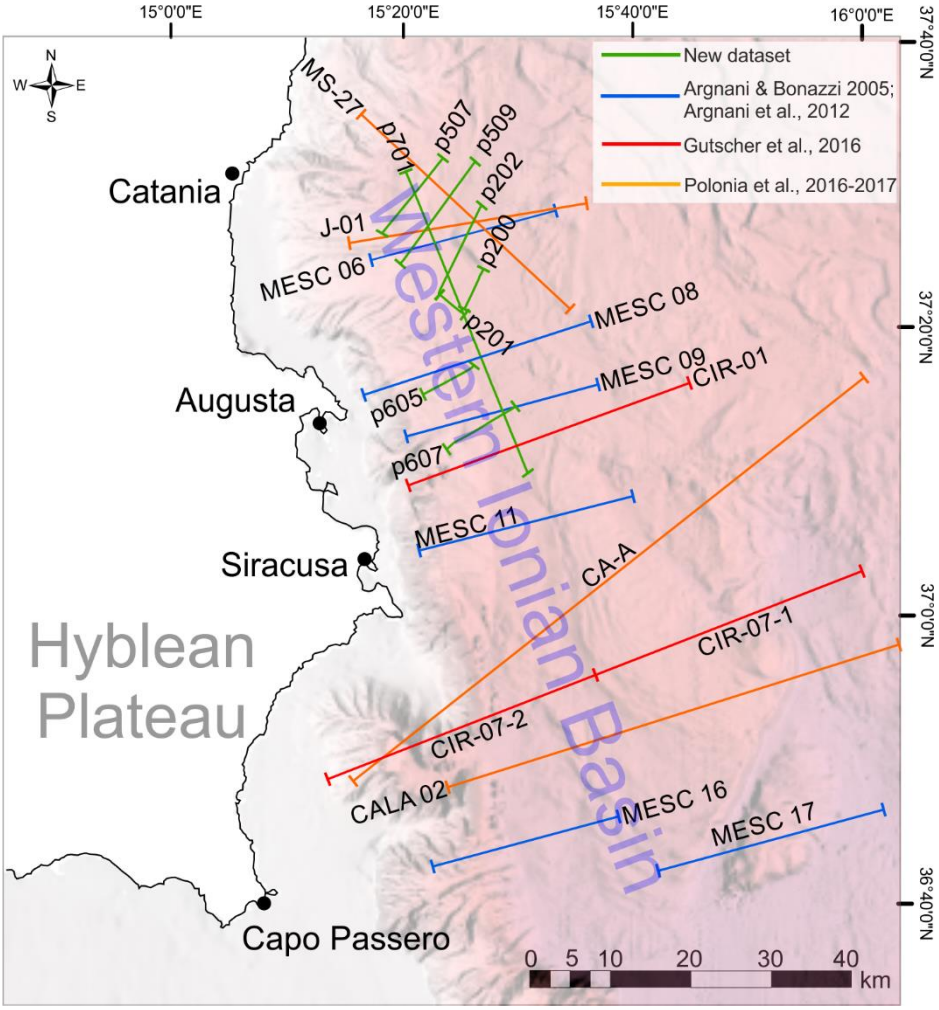

Figure 2.1. a) Map view showing locations of the seismic dataset, including new seismic profiles (green lines) and published geophysical data.

The CIRCEE-HR seismic data were acquired using a 450 m long, 72 channel Sercel seismic streamer with an average geophone spacing of 6.25 m and towed 150m behind the vessel. The seismic source was a six mini-GI airgun array with a total volume of 111 cubic inches (1.8 liters) fired at a cadence of once every 6 s, for an average shot spacing of 16 m and a 24-fold coverage for each common midpoint. Quality control of the seismic data, including processing of the navigation files (shot position and streamer geometry), was performed with the SISPEED software (Ifremer). The

seismic data were subsequently band-pass filtered (70–425 Hz), stacked and time migrated using a water velocity of 1500m/s, using the Seismic Unix software package" (Gutscher et al., 2016).

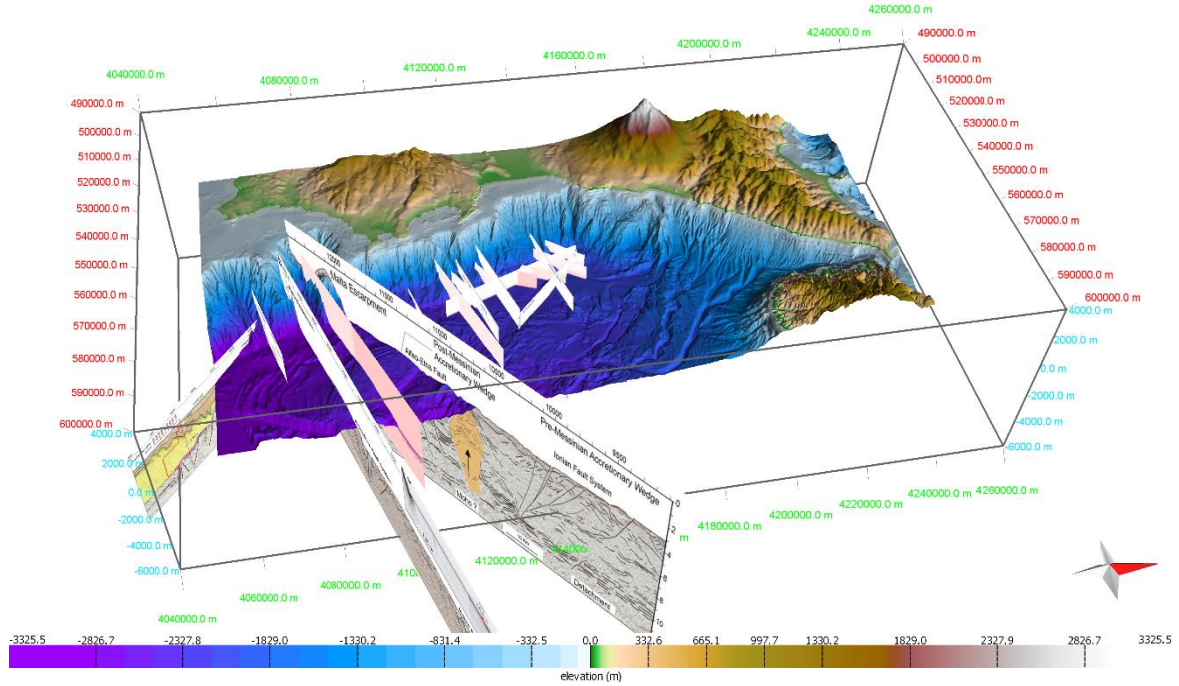

Figure 2.2. View of the 3D workspace (MOVE software, Petex) showing the location of interpreted seismic profiles (from Gambino et al., 2021).

The POS496 seismic profiles were acquired by mean of an 80-channel digital solid-state Geometrics GeoEel streamer (group interval of 1.5625 m). "A Sercel Mini GI-Gun seismic source, with a total volume of 0.4 L, was shot in a harmonic mode. The shot interval was set to 6 s, resulting in a shot distance of ~12 m at a ship's speed of four knots. The seismic profiles were processed using the commercial software package Schlumberger Vista Seismic Processing. The processing workflow includes bandpass filtering with corner frequencies of 40/80/600/1000 Hz, despiking, debias filtering,CMP binning, and normal-move-out (NMO) correction. All data were time migrated by using the software's finite difference migration. Due to the relatively short streamer and the high-water depths, no dedicated velocity analysis could be applied during NMO correction and migration. Hence, a constant velocity of 1500 m/s was applied." (Krastel, 2016).

In addition, previously published seismic profiles (Argnani and Bonazzi, 2002; Argnani and Bonazzi, 2005; Argnani et al., 2012; Polonia et al., 2016; Polonia et al., 2017) have been used. This

depends on the necessity to cover eventual gaps in our seismic dataset and to better detail the seismic interpretation as well as the development of the 3D model.

2.3. Bathymetry

A high-resolution (10-30m) bathymetry (Fig. 2.3) was used to better characterize the fault traces on the seafloor and to constrain the spatial extent of the faults and their longitudinal geometry. The bathymetry (Gutscher et al., 2016; Gutscher et al., 2017) consists of a compilation of several data acquired during marine surveys since 2010 (R/V Meteor cruise 86, 2010 PI – S. Krastel; MocoSed R/V PourquoiPas 2012 PI – T. Garlan; Circee R/V Suroît 2013 PI – M.-A. Gutscher; R/V Meteor cruise 111, 2014 PI's – H. Kopp, M.-A. Gutscher; R/V Meteor cruise 112, 2014 PI – G. Bohrmann; Chianti R/V Sarmiento di Gamboa, 2015 PI's – C. Ranero, V. Sallares).

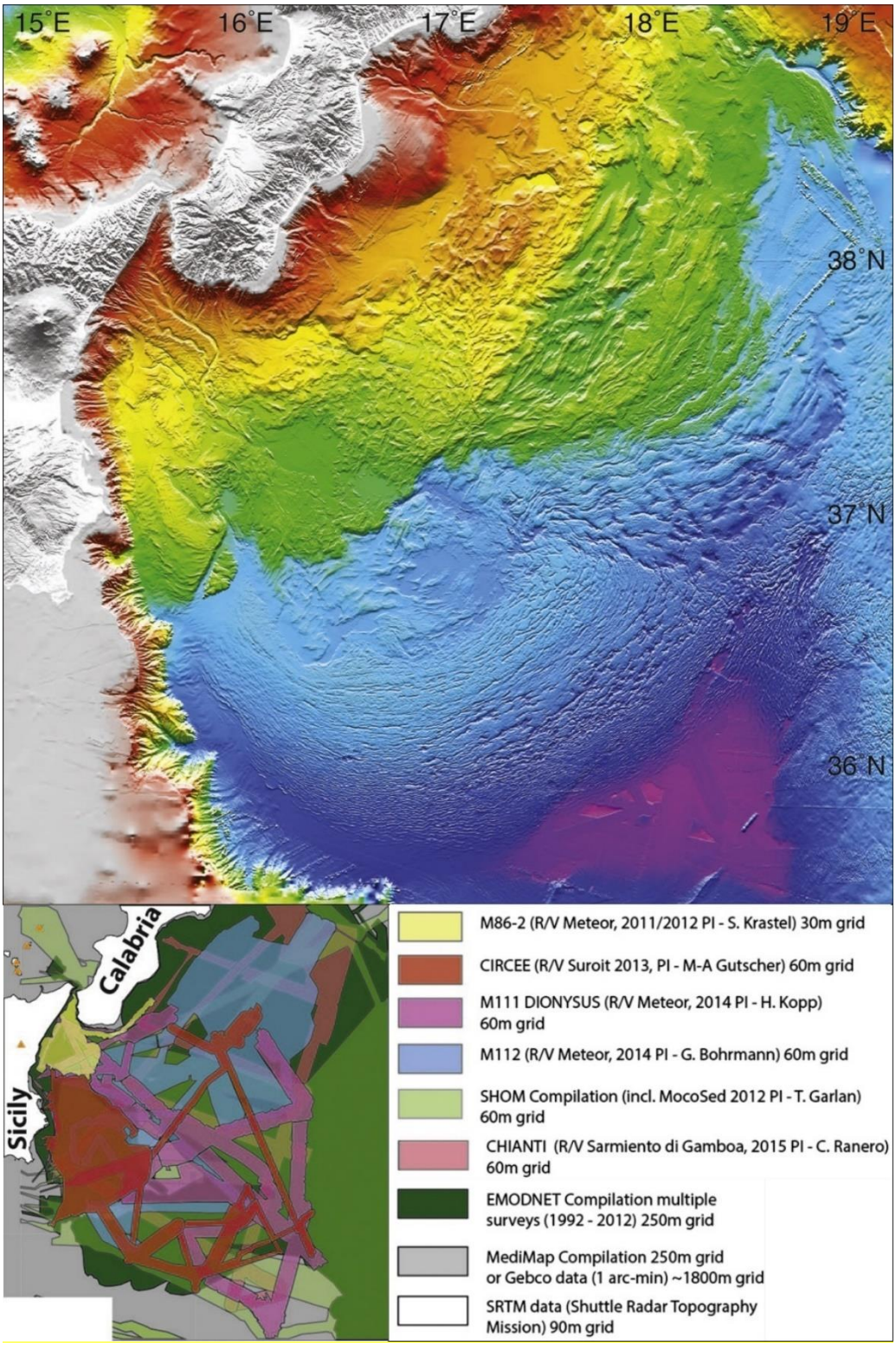

Figure 2.3. Hill-shaded bathymetric compilation. Inset shows the areal coverage of compiled data (from Gutscher et al., 2017).

3. Seismic interpretation

3.1. Basic concept of seismic imaging

Seismic data acquisition and processing were not performed during this Ph.D. project. For this reason, only a simplified explanation of basic concept is provided.

Seismic data are based on the propagation of seismic waves. Seismic waves propagate through the Earth at velocities that depend on the acoustic impedance and density of the medium (rock layer) through which they travel (Liner, 2004; Misra and Yadav, 2018). The acoustic impedance (Z) is expressed by:

$$Z = V \cdot \rho \qquad \text{(eq. 3.1)}$$

Where **V** is the seismic wave velocity and **ρ** is the rock density. From which:

$$V = \frac{Z}{\rho} \qquad \text{(eq. 3.2)}$$

Alternatively, velocity can be described by the following equation:

$$V = \sqrt{E/\rho} \qquad \text{(eq. 3.3)}$$

Where **E** is the Young's Modulus (elasticity) and **ρ** is the density of the considered rock layer.

Density commonly increases with depth (due to increase of lithostatic pressure), and its position at the equation denominator (eq. 3.3) should result in a velocity decrease with depth. However, the relatively higher increase with depth of E results in a general increase of seismic velocity with depth. This concept appears much clearer when the acoustic impedance Z (eq. 3.1) is taken into consideration. Acoustic impedance, in fact, commonly increases with depth. Acoustic impedance is an important property since its sudden change can indicate a change in lithology, fluid contrast or the presence of structural features (fault, fracture etc).

The intrinsic properties of a seismic wave (here we consider amplitude and velocity, but other attributes are shape, polarity, and frequency) are influenced by the properties of rocks through which it travels. The elasticity and density of rocks primarily determine the seismic amplitude and velocity. Such rock properties (density and elasticity) are strongly dependent on the rock internal structure (such as porosity, texture, fractures, fluid saturation, fluid viscosity, pressure, and temperature).

Seismic data acquisition is trivially performed by generating seismic waves by a 'disturbance' (a shot or vibration produced at the sea level or Earth surface) and recording the seismic echo (reflection) after the waves travelled through the rock and back to the hydrophones/geophones (Fig. 3.1). Every time the wave crosses a surface (boundary) separating two rock bodies with difference properties (i.e., density/elasticity), it undergoes physical phenomena such as reflection, refraction, diffraction, scattering, absorption etc. The reflective surface, called 'Reflector' can be a (real) discrete discontinuity (e.g., fault, stratigraphic contact etc.) or a transition zone through which rock properties change. Abrupt properties change commonly results in a stronger seismic reflection. Time required for a seismic wave to travel down to the reflector and back again to the hydrophone (or geophone) is called Two-Way-Time (TWT). Knowing the travel time from the waves source to the geophones, the wave pathway can be reconstructed, and the subsurface arrays of reflectors can be imaged (Fig.3.1). Resolution of seismic data is a function of wave frequency. Frequency is the only wave attributes not changing as waves propagate through the rocks, since it depends exclusively on the source of seismic signal. The higher the frequency of seismic signal, the higher the resolution of the seismic image. On the other hand, high frequency results in a lower depth penetration of the seismic waves compared to lower frequency signal (resolution is calculated in roughly a quarter of the wavelength of seismic wave).

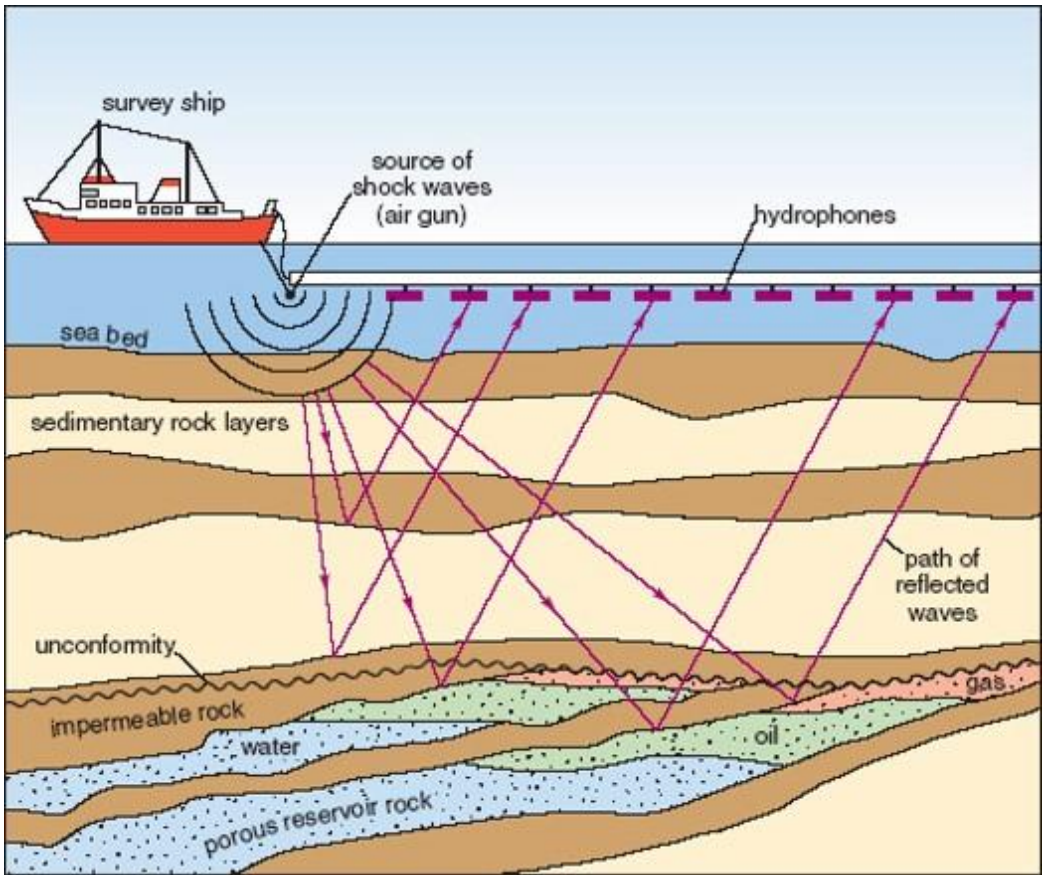

Figure 3.1. Schematic model of the reflection seismic data acquisition.

Seismic-stratigraphic interpretation is based on the assumption that seismic reflectors can be compared to stratigraphic features (e.g., strata, stratigraphic geometry etc.). With this in mind, geological stratigraphic principles are applicable to seismic reflectors.

Seismic-stratigraphic interpretation generally consists of analysis of seismic sequence (top and base bounding horizons, stratal terminations etc.) and analysis of seismic facies (parameters of seismic reflectors, such as amplitude, frequency, lateral continuity etc.).

3.2. Seismic-stratigraphic interpretation

Seismic profiles interpretation allowed the recognition of four main seismic units (named pre-MES, MES, PQ_1 and PQ_2) detectable throughout the entire seismic dataset; these four units are bounded by as many seismic discontinuities (S1 to S4 with S4 being the water/sediments interface)

representing erosional or angular unconformities (Fig. 3.2). Seismic interpretation in based on definition of seismic features (amplitude, frequency, lateral continuity etc.), internal architecture of seismic units, stratal terminations (onlap, downlap, erosional truncation etc.) and bounding discontinuity (Fig. 3.2, 3.3). In following rows are reported the seismic facies of four main seismic units detectable across all the seismic profiles.

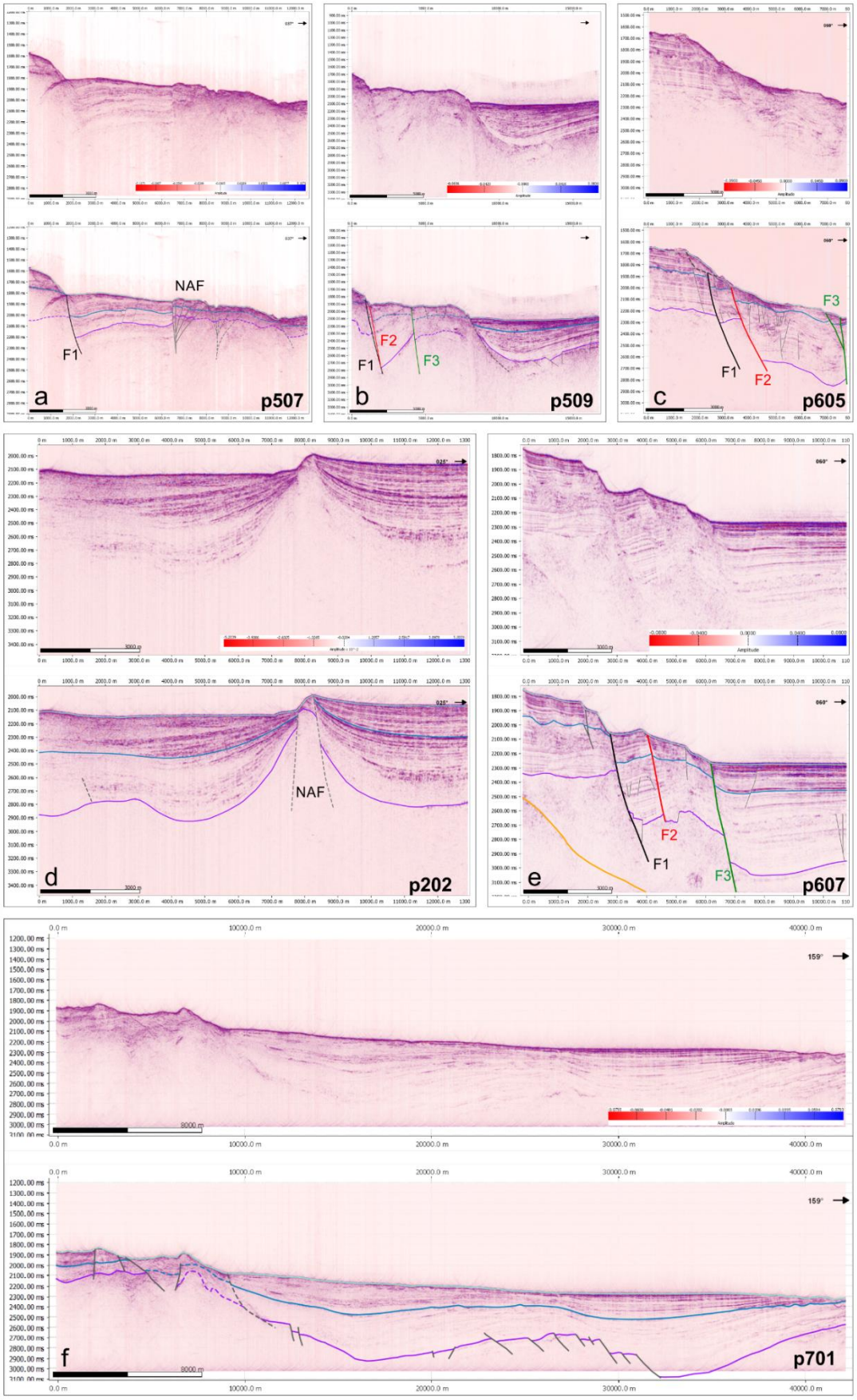

Figure 3.2. Interpretation of main seismic-stratigraphic reflectors and fault lineaments on selected POS496 seismic profiles (TWT). Yellow, purple and blue reflectors indicating S1, S2 and S3 horizons respectively. Main fault F1, F2 and F3 respectively black, red and green structures. a) POS496_p507. b) POS496_509. c) POS496_507. d) POS496_p202. e) POS496_607. f) POS496_p701 (Gambino et al., 2021a). For legend refer to fig. 3b.

Pre-MES unit is a chaotic, locally transparent unit, sporadically showing isolated and highly reflective bodies (Fig. 3.2e, 3.3). Its top horizon is represented by the marked and highly reflective S1 discontinuity, representing a paleo-slope (Malta Escarpment) on which younger sediments lay with on-lap geometry. Basal discontinuity is not visible due to the limited penetration of seismic data; the unit represents part of the acoustic basement.

MES unit consists of a low- to medium-amplitude, medium frequency, sub-parallel to chaotic, discontinuous reflectors showing local continuity. The unit locally manifests (especially where it rises to shallower depth) an internal portion characterized by sub-parallel, laterally continuous reflectors sandwiched between an upper chaotic portion and a lower transparent to chaotic one (Fig. 3.2-d4). This unit is bounded downward by the previously described S1 discontinuity while the upper limit (S2 horizon) is an irregular surface (erosive?) on which overlying reflectors locally rest in paraconformity. S2 discontinuity generally appears as a marked reflector commonly characterized by medium amplitude, however, where the S2 discontinuity deepens it results weakly detectable as the unit locally represents the acoustic basement (Fig. 3.2b).

PQ1 consists of low- to high-amplitude, low- to medium-frequency, subparallel and continuous reflectors. The unit has a highly variable thickness ranging from 0.45 s (TWT) at the base of the slope to 0.1 s in the distal part. The unit is limited downward by the S2 discontinuity, to the West it onlaps directly on pre-MES unit, while the upward limit is represented by S3 erosive truncation (Fig. 3.2b). At the base of the unit, a discontinuous, semi-transparent layer is observed (Fig. 3.2c). It is mostly found in structural depression or paleochannel. Within the unit are observed seismic lense-shaped '*enclaves*' and wedge-shaped bodies (Fig. 3.2c). The first inclusion shows a transparent to chaotic seismic facies and seems to have intruded within layers, thus resembling a sill-like body with intruding direction orthogonal to the seismic section. Even though the occurrence of volcanic intrusion has been reported in the area (Scandone et al., 1981; Patacca et al., 1979; Bianchi et al.,

1987; Grasso et al., 2004), the transparent facies of these bodies contrast with (but not ruling out) a possible volcanic nature of the inclusions. Alternatively, it can be the expression of sedimentary (mud/clay) intrusions which have been as well observed in the area (Manuella et al., 2012; Barreca et al., 2014). The other wedge-shaped bodies show chaotic facies and variable thickness thinning away toward the East. They have been interpreted as landslide deposits (possibly triggered by fault movement) since they occur preferentially adjacent to fault planes and having their thicker portions toward the faults (Fig. 3.2c).

PQ2 is the upper seismic unit and mostly represents the seafloor. It is characterized by high-amplitude, high-frequency horizontal, parallel and laterally continuous reflectors. The mean thickness is about 0.1 s at the base of the Malta Escarpment slope and gets thinner toward the East. The stratigraphic relation with the lower unit is mostly represented by a paraconformity, but locally PQ2 reflectors approach the underlying S3 discontinuity with onlap geometry (Fig. 3.2). The top reflector is represented by the seafloor.

3.3. Chrono-stratigraphic correlation

Due to the absence of drill-holes in the study area, lithological and chrono-stratigraphic interpretation of seismic units is based on their seismic facies, available literature, and correlation (if possible) with on-land geology.

Pre-MES unit is not well imaged in seismic data due to its deeper position and internal chaotic seismic facies. The strong top reflector (S1 reflector) and the internal seismic facies is consistent with fractured, carbonate-type lithology, which is widely represented on-land (Hyblean Plateau). Analysis of dredged samples from the MESC slope (Scandone et al., 1981) report the presence of Mesozoic to lower Miocene deposits comparable to coeval rocks cropping out on-land. including limestones and marls intercalated with and intruded by volcanic and/or mud bodies locally producing seamounts at the seafloor (Barreca et al., 2014; Gutscher et al., 2016).

MES unit reflective top horizon (S2 reflector) well correlates with the M-reflector representing the top Messinian limit, widely observed in the Mediterranean area (Ryan and Hsü., 1973; Ryan and Cita, 1978; Costa et al., 2004; Lofi et al., 2011). The typical Messinian 'trilogy' (Ryan, 1973; Butler et al., 2015; Roveri et al., 2014; Camerlenghi et al., 2019 and references there in) is not always detectable because of the deep position of MES unit close to the acoustic basement; however, it is locally visible where the unit reaches a shallower position (Fig.3.3-d4). Here, MES unit consists of an upper chaotic portion, a middle portion characterized by layered, parallel and continuous reflectors, and a lower transparent level. This arrangement well correlates with the Messinian internal subdivision broadly observed in the Mediterranean area (Ryan, 1973; Lofi et al., 2011; Butler et al., 2015; Roveri et al., 2014; Dal Cin et al., 2016; Camerlenghi et al., 2019). In particular, this threefold subdivision is in good agreement with the description of Messinian sequence provided by Butler et al. (2015) (≈70 km south of the study area). The authors interpreted the Messinian sequence counterparts (upper and lower units) as the first and second cycles observed on-land (Decima and Wezel, 1973) while the internal, layered level representing muddy sediments. For this reason, we correlate the MES unit to the Messinian Salinity Crisis (MSC - Ryan 2009; Roveri et al., 2014) occurred about 5.96-5.33 Ma (Gautier et al., 1994; Krijgsman et al., 1999, 2001).

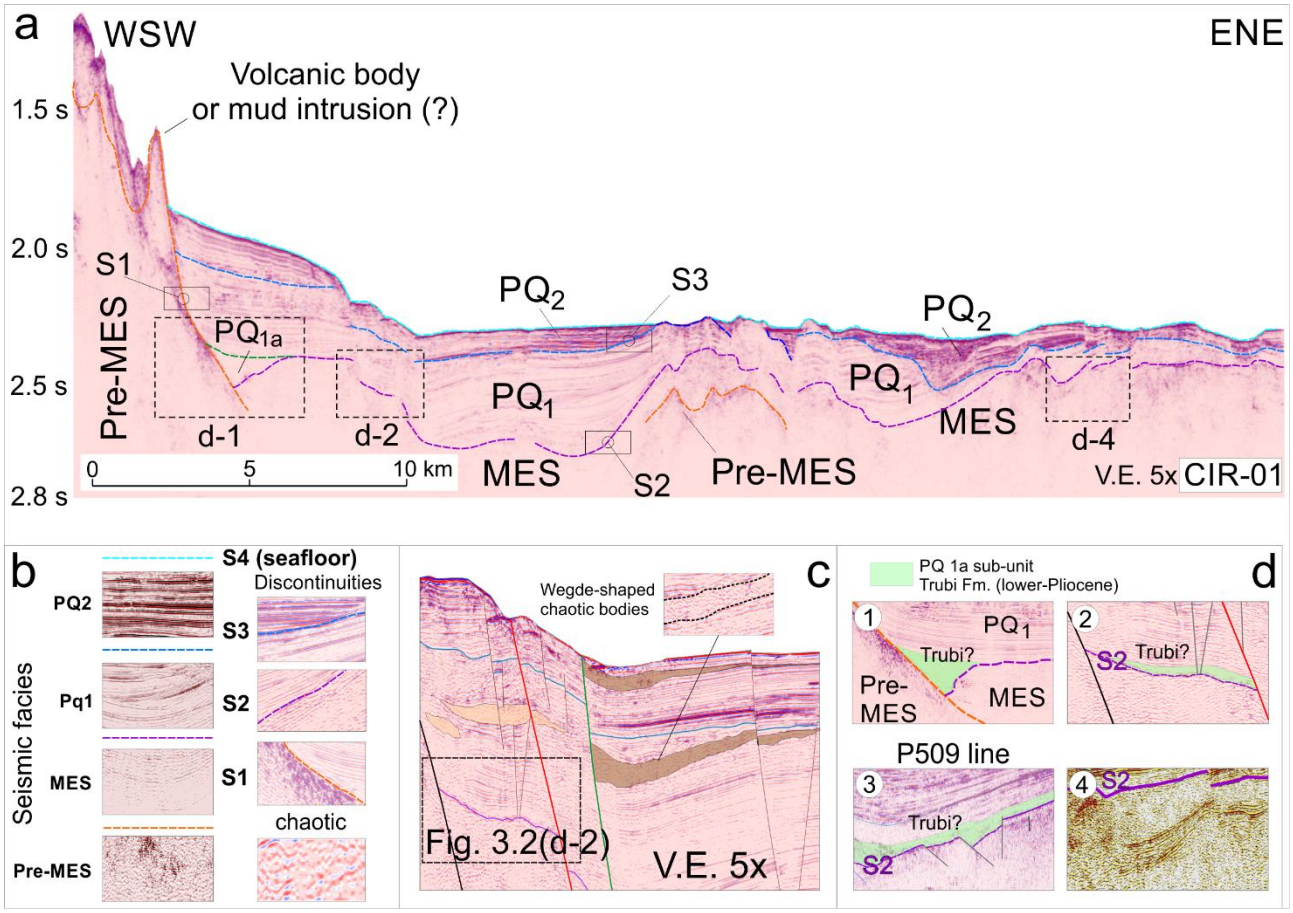

Figure 3.3. a) Highlights of seismic-stratigraphic interpretation on the representative CIR-01 profile (Gutscher et al., 2016). b) Main horizons bounding seismic units are shown. c) wedge-shaped chaotic bodies observed in proximity of faults planes within the Pliocene-Quaternary successions, suggesting landslides triggered by faults activity. d) Local and discontinuous ccurrence a semitransparent seismic unit observed at the base of PQ1 seismic unit interpreted as Zanclean in age (Trubi Fm?). From Gambino et al., 2021.

PQ_1 internal facies and stratigraphic position well correlates with the sub-units 'PQb' and 'PQc' described by Camerlenghi et al (2019) and partially with the 'Unit one' of Micallef et al., (2018) as shown in Fig. 3.3. Moreover, the basal portion of PQ_1 is characterized by a transparent level that, for its stratigraphic position and seismic facies, corresponds to the lower Pliocene (Zanclean) '*Trubi formation*' (Butler et al., 2015, Fig. 3.3d). This level provides a good age constraint for the lower boundary of PQ_1 while the upper age is not well defined. In consideration of PQ_2 inferred age (see further) PQ_1 unit is defined as Pliocene in age.

PQ_2 is the uppermost unit (mostly representing the seafloor) and shows, high-amplitude, high-frequency horizontal, parallel and laterally continuous reflectors suggesting a perfect correlation with the 'PQa' unit of Camerlenghi et al. (2019), whose basal erosive surface (S3) has been dated at 650

ka (from DSDP site 374 cores - Hsü et al., 1978). With this constraint, the PQ_2 unit age is inferred as Pleistocene-Holocene. In addition, the PQ_2 seismic facies indicates a marly–arenaceous nature of sediments which may find a possible analogue on shore, represented by the Middle-Late Pleistocene sands and biocalcarenites of the '*Panchina formation*' (Servizio Geologico d'Italia, 2011).

3.4. Seismic-structural description

A detailed analysis of seismic profiles aimed by observation on high-resolution bathymetry allowed to describe the architecture of subsurface offshore Eastern Sicily where a deformed Miocene-Quaternary basin occurs. Structural interpretation has been performed on TWT seismic profiles which were, then, converted in a later time following the conversion method described in section 3.4.

The most striking structures observed in the area are located at the base of the Malta Escarpment (MESC) slope. Here, a system of E-dipping, NNW-SSE trending, normal-slip (or oblique) faults extends in the near offshore between Catania and Syracuse for a total length of more than 60 km. Three major faults have been observed in all the seismic profiles crossing the MESC, here called F1, F2 and F3 (Fig. 3.4a, b), with F1 being the westernmost tectonic structure and F3 the Easternmost one. The three faults propagate through the entire illuminated subseafloor, offsetting the recognised seismic units with variable offset (see section 3.6).

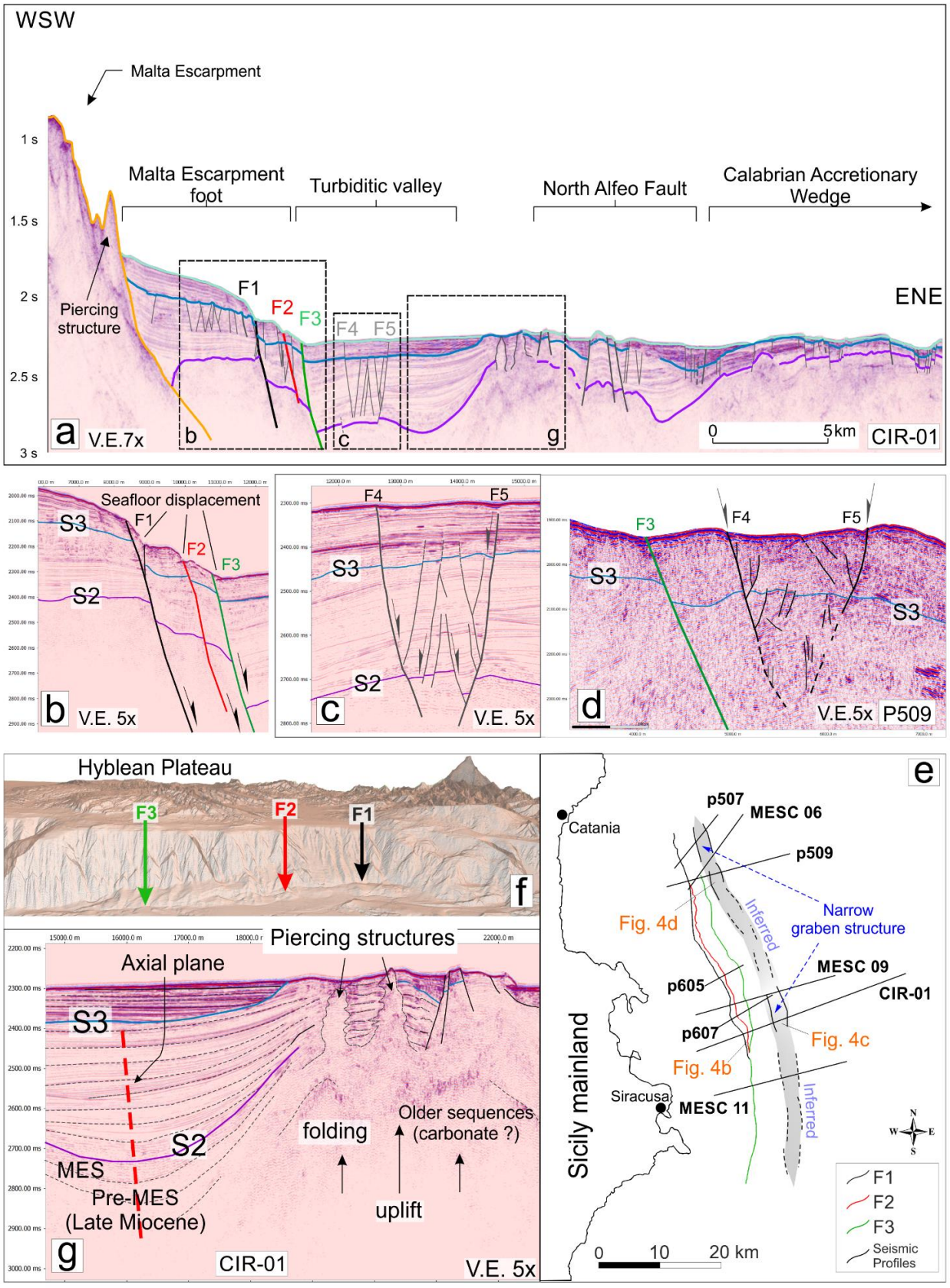

Figure 3.4. Structural interpretation of seismic data a) A system of faults (F1 to F5) deforms the lower MESC slope and the turbidite basin at its base. Further to the East, the NAF separates the basin from the contraction deformation of the CAW. b) Detail of the three main faults of the system and displaced horizons. c) Detail of the graben structure deforming the central part of the basin, observed in CIR-01 and d) p509 profiles. e) Map view of the study area with focus on MESC faults and related graben. f) Perspective 3D view of the bathymetric expression of MESC faults. g) PQ1 shows a subsidence-related folding (see red dashed axial plane) and related uplift to the east. The uplifted culmination is then crosscut by piercing structures.

Further East, a narrow (3.5 km wide) graben deforms the sedimentary basin here called '*Turbidite basin*' (Fig. 3.4a). The graben, bounded by F4 and F5 fault, is detectable in sections p507, p509, and Cir-01 (Fig. 3.4a, c, d). The last one, due to its clear reflectors, provides further details of the graben; besides F4 and F5 opposite dipping fault (Fig. 3.4c), other minor faults are observed within the down-faulted block. Almost all the faults forming the graben, are rooted within the MES unit, with F4 and F5 crosscutting the S2 horizon (top of MES unit) and disappearing within the acoustic basement. The easternmost F5 fault shows offsets increasing with depth, suggesting an extended activity overtime. Conversely, F4 shows relatively constant offset even for deeper reflectors, and a seafloor offset of about 3 m indicating its recent activity. Minor faults, instead dissipate upward within the PQ_2 unit, without any offset at the seafloor. On bathymetry, the graben is not visible due to their limited seafloor offsets, but seismic interpretation revealed its northward continuity indicating how it runs parallel to the fault system detected at the MESC slope base (F1, F2 and F3, Fig. 3.4e). Anyway, no evidence of the graben is observed to the South of Cir-01 (due to the lack of good quality seismic lines) where the graben is only inferred.

The turbidite basin is bounded to the east by a prominent morpho-structural culmination ('*the uplifted area*' of Argnani and Bonazzi, 2005). This is a ≈10 km-wide folded sector which has been variously interpreted by different authors; 1) as a positive flower structure resulted from the recent strike-slip activity of the North Alfeo Fault (NAF – Gutscher et al., 2016), 2) as a passive folding forced by an uplifting mantle-related serpentine diapirs (Polonia et al., 2017), or 3) as a folding uplift due to the shortening produced by the S-ward advancing front of CAW. Termination of seismic reflectors and geometry of the limbs of the folded area suggest the folding stage be active during Miocene-late Pliocene. During Quaternary, due to its structural and morphological elevated position, the uplifted area undergone strong erosion with subsequent formation of S3 horizon, which was, then, sealed by sub-horizontal Pleistocene sediments (PQ2 unit) and successively pierced by diapiric structures (Fig. 3.4g).

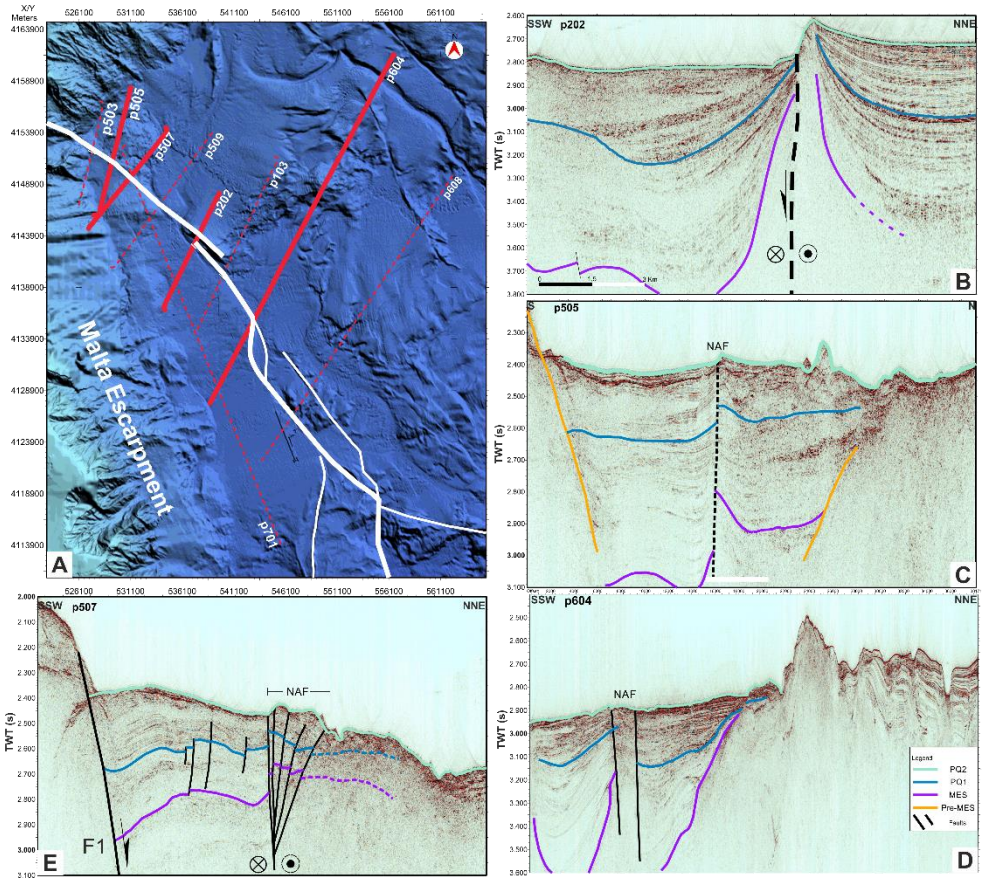

Figure 3.5. Detail of seismic profiles crossing the North Alfeo Fault. a) Map view and localization of seismic profiles. b) POS496-p202, c) POS496-505, d) POS496-604, e) POS496-507 profiles.

The transition to the Calabrian Accretionary Wedge (CAW) is marked by a system of subvertical, E- to W-dipping faults forming the North Alfeo Fault System (Gutscher et al., 2016 - Fig. 3.4a) which, in fact, separates the compressional domain of the CAW from the extensional domain of the Turbidite basin and MESC faults. The NAF faults also affect part of the uplifted area and show a clear vertical offset which is a minor component of mainly strike-slip kinematic of the fault system. In seismic profiles NAF appears both as a system of subvertical discrete faults (profiles p202, p604 and p505 Fig. 3.5) or as a system of faults forming push-up, flower (or palm tree) structure (profile p507, Fig. 3.5e, f). This array, along with the fault strike in relation to the dextral kinematic, produces domains of local extension and compression. In places where extension occurs (profiles p202, Fig. 3.5b, h), it is locally observed the development of diapirism rooted within the MES unit, which is known for its (partial) hyaline nature (Lofi et al., 2011; Butler et al., 2015; Micallef et al., 2019 and

refences therein). Conversely, compression domains result in an anticline-like morphology produced by the formation of positive flower structure (push-up, Fig. 3.5e, f).

Formation of the uplifted area attributed to the activity of NAF (Gutscher et al., 2016) or to the shortening caused by the advancing front of CAW (Argnani and Bonazzi, 2005) would pre-date its deformation to (at the most) lower/upper Pliocene (4 Ma) implying a more recent activity. This view does not find confirmation in seismic lines where onlap terminations of lower Pliocene reflectors on S2 horizon suggests an onset of deformation at Miocene-lower Pliocene transition, when the CAW front was ≈100 km far to the North of the study area (Gueguen et al., 1998; Faccenna et al., 2001a; Carminati et al., 2012; Gutscher et al., 2016; Mantovani et al., 2020). So, the uplift should have been produced firstly by another process related to an intra- or infra-MES deformation, which later could have been coupled with the NAF or CAW activity.

3.5. Bathymetric observation

Observation of high-resolution bathymetry allowed to define the spatial extension of faults and to detail their hierarchical relations and mutual terminations. The bathymetric expression of the Malta Escarpment (MESC) appears strongly marked, with mean slope gradient of ≈6° and a maximum of ≈12°. The bathymetric drop of MESC in the study area varies southward from ≈1200m in the norther part (Catania offshore) to ≈1700m in the southern part (Syracuse offshore). At the MESC base, the slope gradient decreases to ≈3° due to the presence of active faults previously described (F1, F2 and F3) which activated part of the Miocene-Quaternary basin down slope. This feature breaks, in fact, the MESC slope in two portions; an upper, steeper slope and a lower, gentler one which forms a toe-like morphology. Such an escarpment toe is not observed in the southern part (out of the study area) of MESC (see Micallef et al., 2019 for further detail) due to the lack of fault activity.

Within the slope base F1 and F3 faults show clear bathymetric expression fitting well with the sub-surface fault traces mapped in seismic profiles. Conversely, F2 shows an un-continuous, and

locally un-clear seafloor expression which had to be constrain by mean of seismic profiles. F1 shows a marked NNW-SSE, 45 km-long seafloor expression which terminates against the North Alfeo Fault (NAF) and F3 fault, respectively to the North and South. The F3 fault represents the main fault of the system, and its curved bathymetric expression runs roughly N-S in its southern part (about half of the length) and turns NNW-SSE in the northern part covering a total length of about 56 km. It terminates against the MESC to the South and dissipate to the North. The F2 fault occurs between F1 and F3 faults for a total length of ≈34 km. It terminates northward to F1 and southward to F3. This particular array would suggest F2 as a subordinated fault splay. It is worth noting that since the F1 and F2 faults converge to F3, the system is highly likely representing the shallower splay of a single fault developing in depth. Anyway, given that no proof of a single fault in depth is provided by our dataset, and considering that single splay could independently activate, in this study the three major faults are treated independently.

Bathymetric observation provides further insight on fault activity. The norther part of F3 fault scarp shows clear triangular facets (Cotton, 1950; Paliaga, 2015) testifying mutual interaction between erosion (canyons) and fault activity (Fig. 3.6b, d). Even though an oblique nature for the given faults is more reliable as inferred from seismological (Amato et al., 1995; Presti et al., 2013; Musumeci et al., 2014), field survey (Adam et al., 2000; Gambino et al., 2021a) and geodetic data (Mattia et al., 2012; Palano et al., 2012), no kinematic information about a possible oblique component can be obtain from bathymetry or seismic profiles. This implies that the long living debate about a left or right lateral component remain still unsolved (see section 1.3.2 for detail). Further East, no seafloor expression of graben is observed and its position (Fig. 3.4e) has been derived on the basis of seismic profiles.

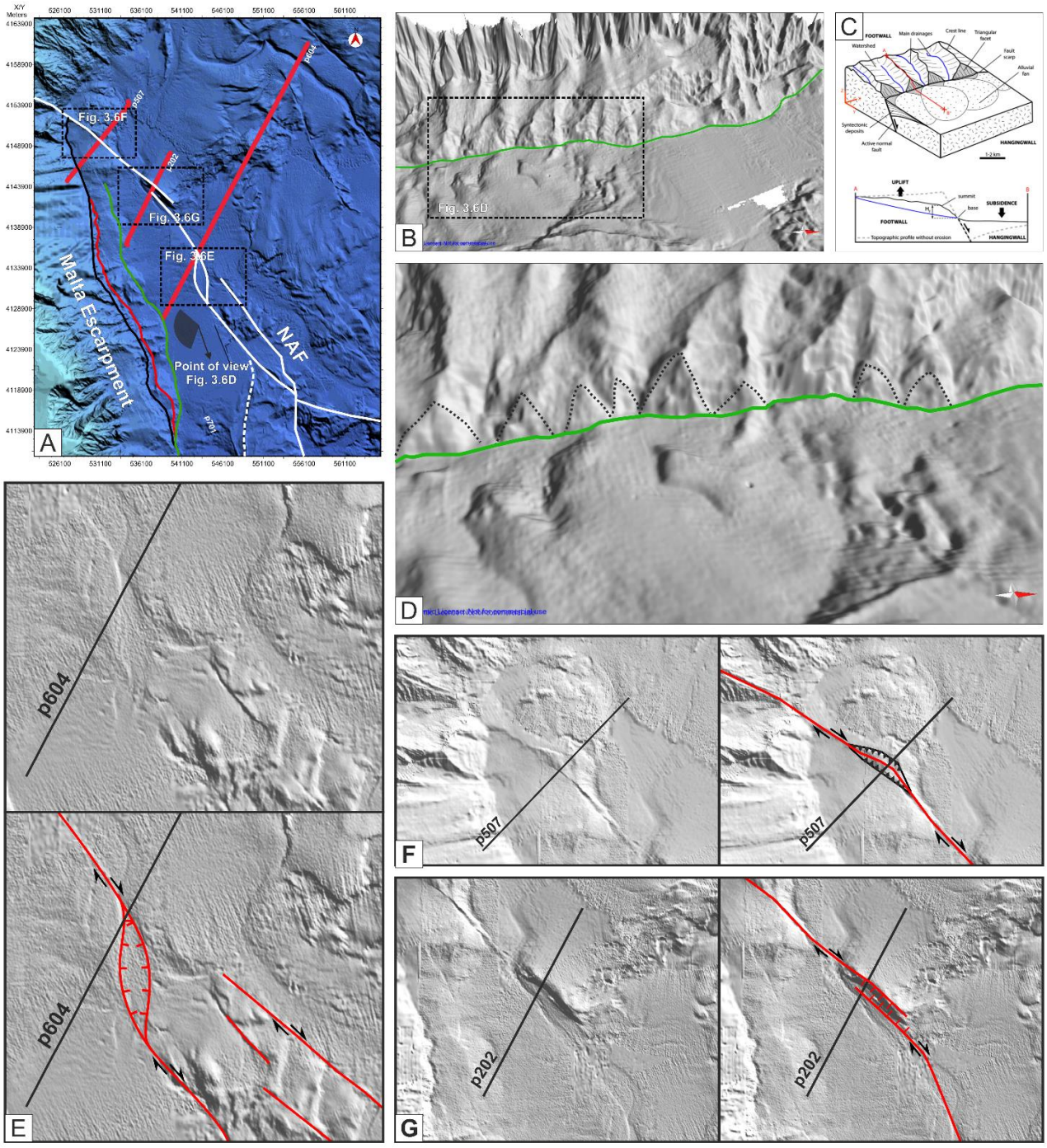

Figure 3.6. Bathymetric expression and interpretation of active fault deformation. a) Map view and localization of described spots. b) Perspective 3D of the triangular facets along the F3 fault. c) Analogue model simulating the formation of triangular facets (Strak et al., 2011). d) Detail of triangular facets of b. e) Bathymetric expression of a releasing band indicating dextral shear. f) Uplift compression related to a positive flower structure (see Fig. 3.5e). g) The positive bathymetric relief is interpreted as the result of an uprising diapir favoured by the releasing stepover of two branches of the NAF.

Another impressive structure observed in the study area is represented by the North Alfeo Fault (NAF – Gutscher et al., 2016, 2017). The morpho-bathymetric expression of NAF has been treated in detail by (Gutscher et al., 2016) who highlighted its dextral kinematic together with direct submarine scuba-diving observation of displaced basaltic lava flows (Chiocci et al., 2011). Here, we

confirm the dextral kinematic of NAF by providing a different explanation for some bathymetric features, in the light of further insight offered by seismic profiles. In correspondence of profile p202 (Fig. 3.5h) a narrow, sigmoidal-shaped, 5 km-long bathymetric height is observed. The culmination is the result of an uprising diapir favored by the presence of an extensional domain. Both bathymetry and seismic profile suggest that the sigmoidal-shaped, diapir-like, culmination is produced by the occurrence of a twofold branching of NAF with formation of a soft-linked, right-stepping, releasing-stepover (Sylvester, 1988; Cunningham and Mann, 2007 - Fig. 3.5b, h). Similarly, in correspondence of p507 profile another elevated, lozenge-shaped area occurs along the NAF. Here, the NAF trace bends (from N to S) firstly to left and then to the right. Accordingly with the dextral kinematic of NAF, this geometric configuration results in restraining bend and formation of a contractional domain. This is further confirmed by the presence of a positive flower (or palm tree) structure (Sylvester, 1988; Cunningham and Mann, 2007 - Fig. 3.5e, f) observed in seismic profiles (see section 3.5)

3.6. Analysis of seismic data

3.6.1. Time/Depth conversion

Time/Depth conversion is performed by mean of "2D Depth Conversion tool" of MOVE suite. In order to make conversion more reliable, the parameters of all seismic units have been defined (Tab. 3.1) rather that performed a fixed equation to the entire seismic line. Conversion has been applied separately to each interpreted profile (even the already published profiles which were used to fill the gap in our dataset).

Table 3.1. Parameters of interpreted seismic units. Seismic velocities are reported from literature. Sub-units PQ1 a, b, c are discussed in section 6.

Seismic Unit	Age		Age (Ma)	Lithology	Seismic Velocity (m/s)	Surface porosity	Density (kg/m^3)	Depth Coeff. (km^{-1})	Ref. seismic velocities
PQ2	Quaternary		0.65-0.012	Silt-sandstones	1760	0.4	2700	0.39	Micallef, et al. 2018.
PQ1 c	Pliocene	upper	3.6-2.58	Silt-sandstones	2280	0.4	2700	0.39	Micallef, et al. 2018; Camerlenghi et al., 2019.
PQ1 b			4.0-3.6	Silt-sandstones	2280	0.4	2700	0.39	
PQ1 a		lower	5.3-4.0	Silt-sandstones	2280	0.4	2700	0.39	
MES	Messinian		7.2-5.3	Evaporites	4000	0	2200	0.00	Butler et al., 2015; Maesano et al., 2017.
Pre-MES	Pre-Messinian		up to 7.2	Limestones	3250	0.7	2700	0.71	Gallais et al., 2011; Kokinou et al., 2013; Micallef et al., 2018.

The equation behind the Time/Depth conversion is the following:

$$Z = V_0(e^{kt} - 1)/k \qquad \text{(eq. 3.4)}$$

Where **Z** is the converted depth, $\mathbf{V_0}$ is the seismic velocity of a given unit, **e** is the natural logarithm base, **k** is the rate of velocity change with depth (given by default) and **t** is the one way travel time (OWTT) in seconds.

3.6.2. Fault displacement analysis

With the purpose of estimating the deformation-rate of faults forming the MESC, a fault offsets analysis was carried out on the time/depth-converted seismic profiles. Analysis has been carried out on the three major faults forming the Malta Escarpment reactivated portion (F1, F2, and F3 in Fig. 3.4a) since they represent the structures on which data coverage is more complete.

The F1 fault propagates through the entire (illuminated) subseafloor and displaces the main seismic units with variable offsets (Fig. 3.4b). Given the adopted time/depth conversion model (Tab. 3.1), F1 offsets the base of the PQ1 (S2 horizon) and PQ2 (S3 horizon) units, respectively, up to 460 and 260 m. Displacement reaches also the seafloor producing a vertical (average) offset of ≈70 m with a maximum value (≈150 m) observed in MESC09 line (Fig. 3.4b and Tab. 3.2).

Table 3.2a. Faults parameters measured on interpreted seismic profiles (yellow area indicating missing data)

Along-strike	seismic Profiles	Faults	S4 Throw	S4 Total Throw	S3 Throw	S3 Dipslip	S3 Total Throw	S2 Throw	S2 Dip-slip	S2 Total Throw
12942	**MESC 11**	F1		45200			48600			149800
		F2								
		F3	45200		48600	58900		149800	257600	
22857	**CIR-01**	F1	68300	123800	162100	167800	264300	223900	373800	607000
		F2	24100		46300	77200		121600	146800	
		F3	31400		55900	62900		261500	314800	
26232	**p607**	F1	68200	148500	235500	281700	352700	404700	596400	736400
		F2	50400		61800	79100		76900	106800	
		F3	29900		55400	73800		254800	310300	
28726	**MESC 09**	F1	146200	212200	259100	429300	349000	460900	1020300	670600
		F2								
		F3	66000		89900	132500		209700	321900	
34282	**p605**	F1	80200	179200	86300	104800	268400	90500	129600	396000
		F2	44700		122200	174500		305500	569800	
		F3	54300		59900	114100				
36183	**MESC 08**	F1	69500	145800	78800	84300	212800	129700	156400	470100
		F2	59200		90900	112300		266800	290800	
		F3	17100		43100	52000		73600	80000	
51786	**p509**	F1	41100	64300	241000	323000	374600	460000	665400	688000
		F2	5100		64600	82400		117000	148100	
		F3	18100		69000	77000		111000	125500	
52903	**MESC 06**	F1	100400	100400	127400	128300	127400	441900	504000	441900
		F2								
		F3								
56927	**p507**	F1	110000	110000	240800	314900	240800	282600	440400	282600
		F2								
		F3								

Table 3.2b. Summarized mean and maximum fault throws measured on interpreted seismic profiles.

	Mean Displacement (m)			Maximum Displacement		
	S2	S3	S4	S2	S3	S4
F1	249.42	143.10	68.39	460.90	259.10	146.20
F2	147.97	64.30	30.58	305.50	122.20	59.20
F3	151.30	46.87	29.11	261.50	89.90	66.00
Tot	417.49	203.51	102.67	736.40	374.60	212.20

The F2 fault activity displaced the S2 horizon of (in average) ≈150 m and the S3 horizon of ≈ 65 m, while the seafloor results displaced of ≈30 m (Fig. 3.4b and Tab. 3.2). F3 is the easternmost fault of the system controlling the lower MESC slope. It deformed the entire seismo-stratigraphic sequence displacing the S2 and S3 horizons of (in average) about 150 and 47 m, respectively (Fig. 3.4b, d and Tab. 2). Fig. 3.7 reports throw (vertical offsets) measured on seismic profiles crossing

each fault. Fault throws are related to the detected seismic horizons bounding main seismic units; S2 (top-MES), S3 (top-PQ1), and S4 (the seafloor).

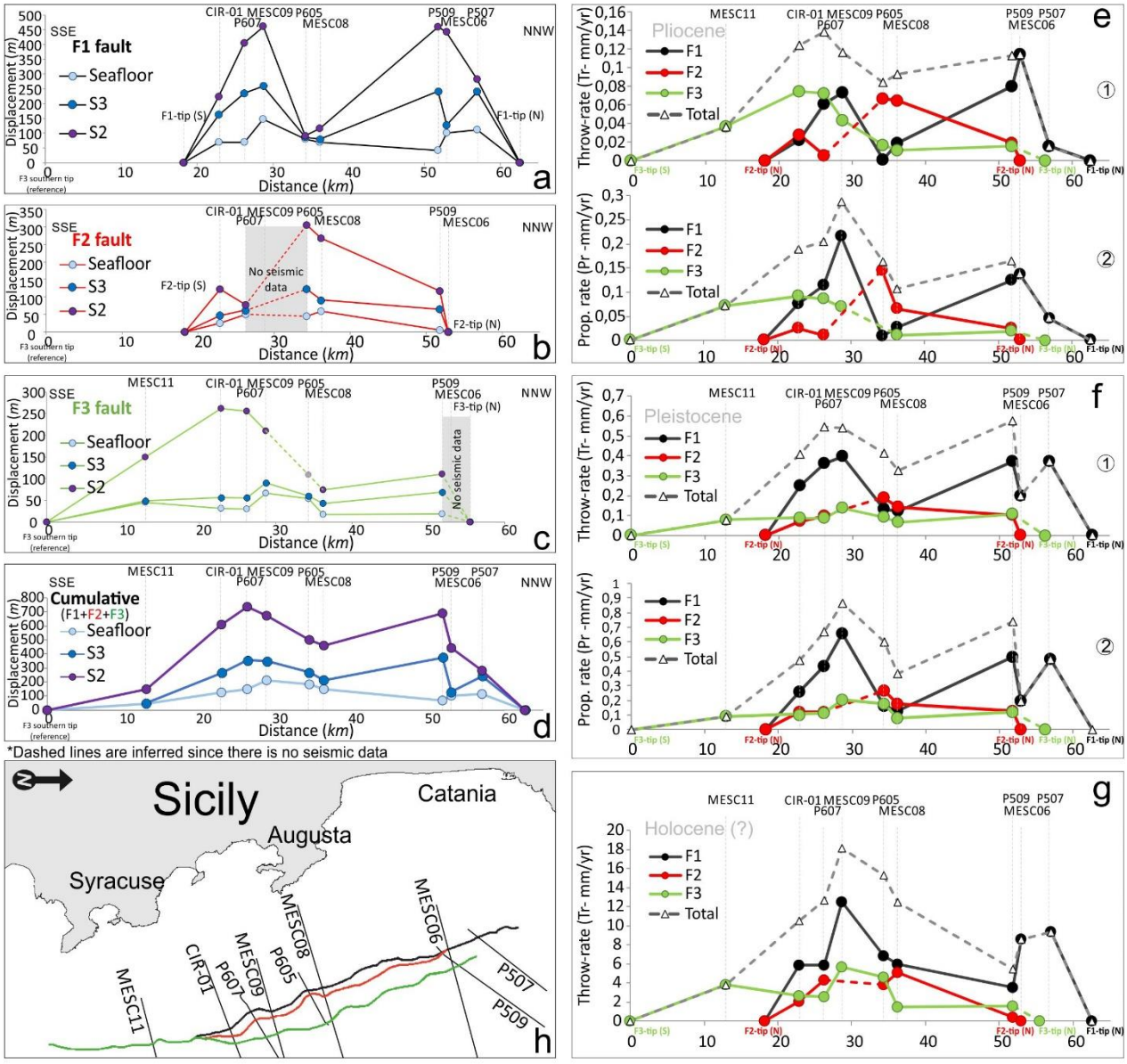

Figure 3.7. Vertical offsets (throw) measured on seismic profiles along the F1 (a), F2 (b), and F3 (c) with respect to reference timelines (S2, S3, and seafloor S4). Throw and propagation rate (relative to vertical and along-dip displacements respectively) have been calculated for the Pliocene (d), Pleistocene (e), and Holocene (f) time intervals.

Along-strike trends for all the faults define a general double-bell shape. F1 maintain the same shape for the three main horizons with relative maxima measured on profiles MESC09 and p509 (maxima values of 460.9 m, 259.1 m, and 146.2 m respectively for S2, S3 and S4 horizons). F2 shows a double-bell shape only for S2 horizon reaching its maximum in profile p 605 (305.5 m). Horizon offsets of S3 and S4 show, instead a single-bell trend with maxima of 122.2 m (profile p605) and

59.2 m (profile MESC08) respectively for S3 and S2. It is worth noting that no data is available for F2 in profile MESC09 (as reported in Fig. 3.7b) due to the low resolution of the seismic line in the central portion. Similarly, F3 outlines a double bell-shaped pattern only for the S2 surface, while S3 and the S4 horizons assume an irregular trend resembling a single-bell curve (Fig. 3.7c).

In Fig. 3.7d is reported the cumulative effect (sum of the offsets) of faults on the main seismic horizons. On cumulative trend, the double-bell shape persists for S2 and S3 horizon while a single trend curve is observed for the seafloor timeline. Cumulative trend of the S4 horizon (seafloor) was analysed in order to evaluate the recent deformation history of the MESC faults even though a large uncertainty could affect offsets estimation, due to the unknown nature (erosive or depositional) of the seafloor. The recent cumulative activity of faults produced a total seafloor offset of ~210 m (profile MESC09).

3.6.3. Fault-rate analysis

On the basis of vertical (throw) and along-dip offsets (slip) measured on the displaced S2 (top-MES), S3 (top-PQ1), and S4 horizons (seafloor) and assumed ages, the fault rate could be calculated. Nevertheless, some considerations need to be addressed. The assumed ages of considered horizons S2, S3 and S4 are respectively 5.33 Ma, 650 ka and 11.7 ka, (Tab. 3.1, see also section 3.3). However, S3 age does not correspond to the upper limit of PQ1 (Pliocene, 2.58 Myr), since S3 represents an erosional surface which truncated part of the upper PQ1. With this in mind, we can go further on calculating the fault rate. We know that the cumulative fault offset of seismic horizon increase with depth (S4<S3<S2). Since the S2 horizon has cumulated offset from its formation (5.33 Ma) to present day, the measured offset would represent the deformation experienced by S2 in the considered long-term. The PQ1 unit laying above S2, deposited over Pliocene time (from 5.33 Ma to 2.53 Ma). So, if we want to consider the offset that S2 experienced during Pliocene, we should consider the offset difference between the S2 and S3 horizon (which start cumulating offset after Pliocene together with S2 horizon). Consequently, the Pliocene rate would be the result of the following equation:

$$\boldsymbol{F_r} = \frac{\boldsymbol{DS_2 - DS_3}}{\Delta PQ1} \qquad \text{(eq. 3.5)}$$

Where **F**r is the fault rate, D**S**$_2$ and D**S**$_3$ are the displacement of S2 an S3 respectively, while ΔPQ1 is the time range of PQ1 (5.33-2.58= 2.75 Ma).

Similarly, Pleistocene rate is calculated taking into consideration S3 and S4 ages and PQ2 age interval (see Supp. Tab. 3.1). Differently, the Holocene rate (throw-rate only) calculation starts from the assumption that the seafloor offset is the result of Holocene fault activity. However, this assumption is rather speculative since, due to the lack of proper datation, the actual age of S4 horizon is unknown as well as the amount of erosion/sedimentation. Given these consideration, throw-rates (vertical fault rate) and propagation-rate (along-dip fault rate) have been calculated for Pliocene and Pleistocene interval, while only the throw-rate could be obtained for Holocene interval (as reported in Fig. 3.7e-g).

Diagrams in Fig.5 show that during the Pliocene, faults were simultaneously active even if with different rates. Accordingly, activity was higher (in average) for F1 (T_R~ 0.05 mm/yr and P_R~0.09 mm/yr) and lower for F2 and F3 (respectively, TR~0.04 mm/yr - PR~0.05 mm/yr and TR~0.04 mm/yr - PR~0.06 mm/yr, Figures 3.7e and Tab. 3.3). Pleistocene rates show faults acceleration compared to the Pliocene one. During this stage, F1 still moved faster (in average TR~0.27 and PR~0.4 mm/yr) than the other (F2, TR~ 0.12 and PR~0.16 mm/yr and F3, TR~0.04 and PR~0.12 mm/yr, Fig. 3.7f). In addition, F2 and F3, previously showing a double-bell shape, evolved into a single-bell trend, suggesting fault linkage and the development of well-defined structures. Holocene rates highlight a further faults acceleration reaching the high values of ~7.3 mm/yr, 3.2 mm/yr and 3.1 mm/yr respectively for F1, F3 and F2 (Fig. 3.7g). Such a high rate (not consistent with regional tectonic) found for Holocene fault rate could derive from uncertainties affecting the bathymetric throw measurement and age estimation of S4 or could also be the result of fault-rate amplification due to a non-tectonic process.

Table 3.3a. Faults rates calculated from faults parameters (Tab. 3.2a) and inferred ages (Tab. 3.1). Tr is the throw-rate (vertical rate), and Pr is the propagation-rate (along-slip rate).

Distance	Seismic lines	Holocene rate (mm/yr)			Middle-Pleistocene rate (mm/yr)					Pliocene rate (mm/yr)				
		Faults	Tr	Cumul. Tr	Faults	Tr	Cumul. Tr	Pr	Cumul. Pr	Faults	Tr	Cumul. Tr	Pr	Cumul. Pr
12942	MESC 11	F1		3.86	F1		0.07		0.09	F1		0.04		0.07
		F2			F2					F2				
		F3	3.86		F3	0.07		0.09		F3	0.04		0.07	
22857	CIR-01	F1	5.84	10.58	F1	0.25	0.41	0.26	0.47	F1	0.02	0.12	0.07	0.19
		F2	2.06		F2	0.07		0.12		F2	0.03		0.03	
		F3	2.68		F3	0.09		0.10		F3	0.07		0.09	
26232	p607	F1	5.83	12.69	F1	0.36	0.54	0.43	0.67	F1	0.06	0.14	0.11	0.21
		F2	4.31		F2	0.10		0.12		F2	0.01		0.01	
		F3	2.56		F3	0.09		0.11		F3	0.07		0.09	
28726	MESC 09	F1	12.50	18.14	F1	0.40	0.54	0.66	0.86	F1	0.07	0.12	0.21	0.28
		F2			F2					F2				
		F3	5.64		F3	0.14		0.20		F3	0.04		0.07	
34282	p605	F1	6.85	15.32	F1	0.13	0.41	0.16	0.61	F1	0.00	0.10	0.01	0.15
		F2	3.82		F2	0.19		0.27		F2	0.07		0.14	
		F3	4.64		F3	0.09		0.18		F3	0.03			
36183	MESC 08	F1	5.94	12.46	F1	0.12	0.33	0.13	0.38	F1	0.02	0.09	0.03	0.10
		F2	5.06		F2	0.14		0.17		F2	0.06		0.06	
		F3	1.46		F3	0.07		0.08		F3	0.01		0.01	
51786	p509	F1	3.51	5.50	F1	0.37	0.58	0.50	0.74	F1	0.08	0.11	0.12	0.17
		F2	0.44		F2	0.10		0.13		F2	0.02		0.02	
		F3	1.55		F3	0.11		0.12		F3	0.02		0.02	
52903	MESC 06	F1	8.58	8.58	F1	0.20	0.20	0.20	0.20	F1	0.11	0.11	0.14	0.14
		F2			F2					F2				
		F3			F3					F3				
56927	p507	F1	9.40	9.40	F1	0.37	0.37	0.48	0.48	F1	0.02	0.02	0.05	0.05
		F2			F2					F2				
		F3			F3					F3				

Table 3.3b. Mean and maximum throw rates.

	Throw rates (mm/yr)					
	Mean			Max		
	S2	S3	S4	S2	S3	S4
F1	0.05	0.28	7.31	0.11	0.40	12.50
F2	0.04	0.12	3.14	0.07	0.19	5.06
F3	0.04	0.08	3.20	0.07	0.14	5.64
Tot	0.10	0.38	10.73	0.14	0.58	18.14

4. 3D modelling methodology

4.1. Introduction

3D geological modelling basically consists of data positioning (wells, dips, cross-section etc.) in a 3D space in order to obtain a geometrical representation of geological features (stratigraphic surface, faults etc.). There is a large variety of methods for 3D modelling and the use of one or another depends on the kind and amount of data available. In the available literature, 3D geological modelling is performed using a variety of data, including well data, 2D sections, geophysical data, field data/geological maps and integrated multisource data.

3D methods are commonly grouped in two principal categories: deterministic and probabilistic (or stochastic) methods (Mencos, 2010). In the first group, uncertainty is qualitatively evaluated after the 3D model is developed. Conversely, in probabilistic methods the uncertainty is quantitatively determined by mean of geostatistical concepts (López-Mir, 2013).

Deterministic methods are mainly used for visualization of geological objects, which is the scope of this study. 3D modelling by deterministic methods can be based on reconstruction of surfaces (explicit deterministic methods) or volumes (implicit deterministic methods). Explicit methods are ideal for reconstruction based on scattered data which need to be interpolated. Implicit methods, instead, require a dense and continuous database (e.g., 3D seismic cubes (Mencos, 2010; López-Mir, 2013). Within the explicit deterministic methods, interpolation between cross-sections is a timesaving and relatively easy way for visualizing 3D geological structures particularly used in absence of dense data or with data not regularly spaced in the 3D working space. This method is used in this thesis as only seismic profiles are available for the given area due to the absence of geological constraints such as wells data, field data etc.

4.2. 3D digitalization

The workflow used to obtain the 3D reconstruction of faults and main horizon is simplified in Fig. 4.1. Interpreted and converted 2D seismic profiles (see chapter 3) have been interpolated allowing to build up a simplified but consistent 2½D model of the faults forming the active portion of MESC and two reference surfaces representing S2 and S3 horizon (Fig. 4.1 and 4.2). Fault bathymetric expression has been used to better constraint the along-strike fault geometry in order to reconstruct a more reliable fault plane.

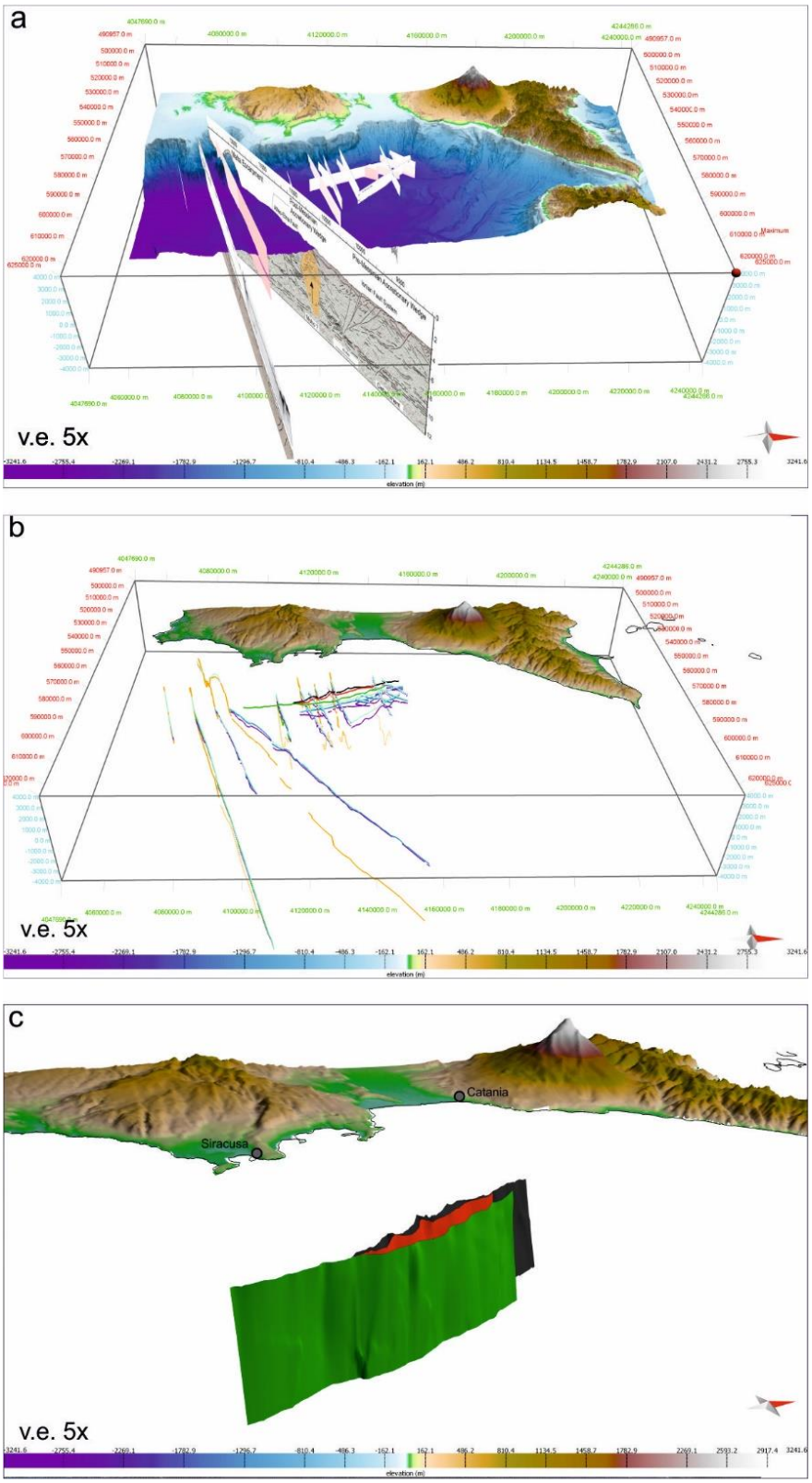

Figure 4.1. Workflow adopted for faults modelling a) Unpublished (POS496) and published seismic reflection profiles (Polonia et al., 2016, 2017; Argnani and Bonazzi, 2002, 2005, 2012; Gutscher et al., 2016) and a high-resolution bathymetry (Gutscher et al., 2016, 2017). b) Interpretation of main reflectors and faults (picking). c) Interpolation of picked lines and construction of a 2 ½ D-modelling of fault surfaces (c). From Gambino et al., 2021.

For creation of faults and horizon 3D surfaces, the 'create surface' tool of MOVE software has been used. Lines digitized in 2D seismic section have been interpolated using the 'Ordinary Kriging'

algorithm. It is a geostatistical calculation based on sparse input data, which predicts a value at a point of a region using data in the neighbourhood location. The algorithm is based on the principle of spatial continuity of data (Isaaks and Srivastrava, 1989).

Reconstruction of faults planes followed the hierarchical criterion observed in seismic lines and bathymetry. Since F3 represents the main fault on which F1 and F2 terminates, 3D faults planes have been manually conditioned in order to reproduce such a hierarchical relation. In fact, interpolation of fault trace in seismic sections produces a fault plane whose extension is predetermined by the user. After all the three faults are reconstructed, they show mutual cross-cutting relation. For this reason, manual adjustment is needed in order reproduce the actual faults termination. In particular, F1 terminates southward on F3, while F2 manifests its southern termination on F3 and northern termination on F1. The F1 northward termination on NAF is not performed since NAF is not taken into consideration for 3D reconstruction.

Reconstruction of stratigraphic horizon S2 and S3, have been performed by interpolating line objects (top units reflectors deriving from seismic sections), separately for the one placed on the footwall and the other on the hanging wall. This passage is performed for the purpose of creating offset between the same horizons on footwall and hanging wall. Interpolation of all line objects (for each stratigraphic surface) would have produced a single, continuous, mean surface cutting through the faults with no offset. Successively, they have been conditioned by mean of manual adjustments (cut and repair) in order constrain strata termination on fault planes.

4.3. Results of 3D modelling

The obtained model consists of 3 main fault planes (F1, F2 and F3, Fig. 4.2) and two stratigraphic surfaces (S2 and S3, respectively the top MES and the top PQ1, Fig. 4.2).

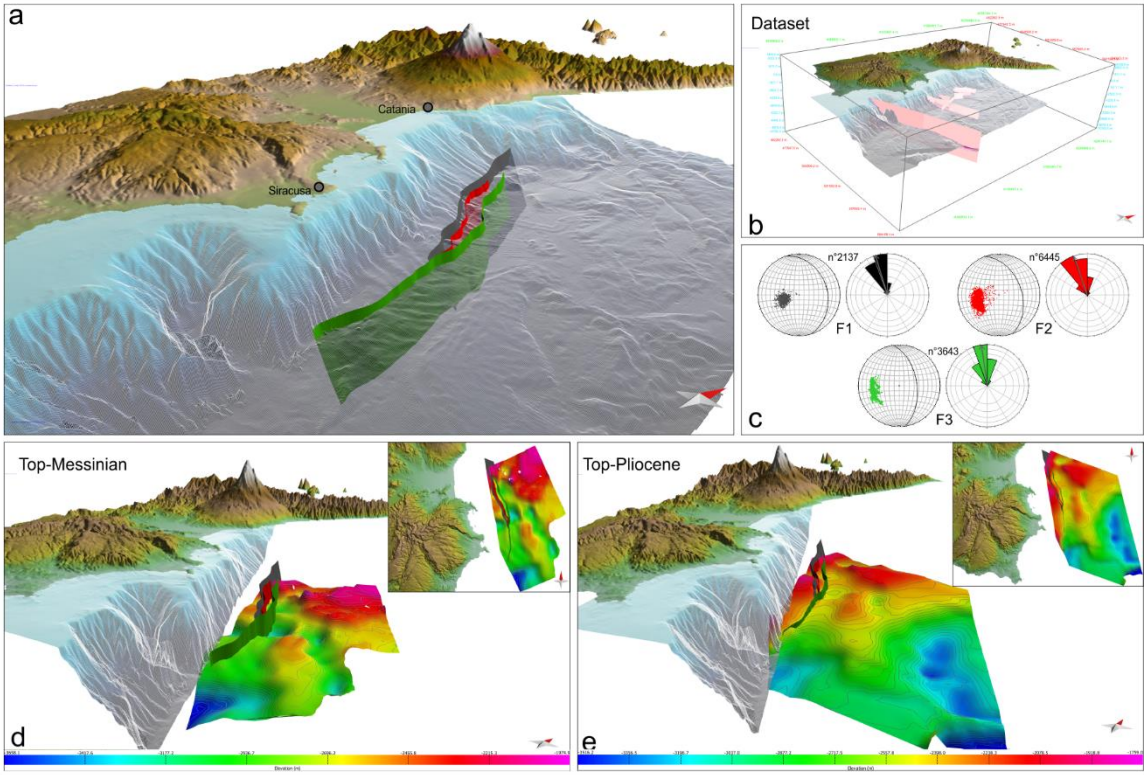

Figure 4.2. a) Modelled faults surfaces. b) 3D workspace. c) Stereographic projections (Schmidt lower hemisphere) of faults attitudes. d) Reconstruction of S2 and (e) S3 surfaces.

Even if depth-limited, due to the low-penetration/high-resolution of seismic profiles, the model provides a good estimation of faults geometric parameters (i.e., length, width, area, dip, and strike see Tab. 4.1) which are useful for estimation of their seismic potential (see section 5.2). According to the model, F1 is a roughly 45 km-long, N345E trending structure, ENE dipping at about 36°. F2 is a 35 km-long, N340E trending fault dipping toward the ENE at about 46°. Finally, F3 is a 60 km-long, N353E trending, fault dipping at 49° toward the ENE (see Fig.7). Faults parameters are summarized in Tab. 4.1).

Table 4.1. Geometric faults parameters and estimated maximum magnitude. Magnitude estimation is based on empirical scaling relations (Wells and Coppersmith, 1994; Leonard et al., 2010).

Geometric Parameters	**F1**			**F2**			**F3**		
Mean Strike		**N345E**			**N340E**			**N352E**	
Mean Dip (°)		**36**			**46**			**49**	
Lenght (km)		**44.44**			**33.72**			**56.46**	
	min	Width*	max*	min	Width*	max*	min	Width*	max*
Fault depth-range and Width (m)	-1813	**4337**	-6150.5	-1908	**3322**	-5230	-1854	**5275**	-7129
Area (km2)*		276.92			98.65			334.05	
	Expected Magnitude (Wells and Coppermisth, 1994)								
	min	*mean*	*max*	*min*	*mean*	*max*	*min*	*mean*	*max*
M based on Surface Rupture lenght (SRL)	6.27	**7.03**	7.80	6.14	**6.88**	7.61	6.38	**7.17**	7.97
M based on Rupture Area (RA)*	5.95	**6.42**	6.90	5.53	**5.96**	6.39	6.02	**6.50**	6.99
M based on downdip Rupture Width (RW)*	6.27	**7.04**	7.81	6.15	**6.89**	7.63	6.38	**7.17**	7.97

(*) understimated

Reconstructed S2 and S3 horizons are reported in Fig. 4.2. Both surfaces generally deepen toward the south, according to the general slope bathymetric gradient toward the Ionian abyssal plain depocenter (located SE-ward of the study area).

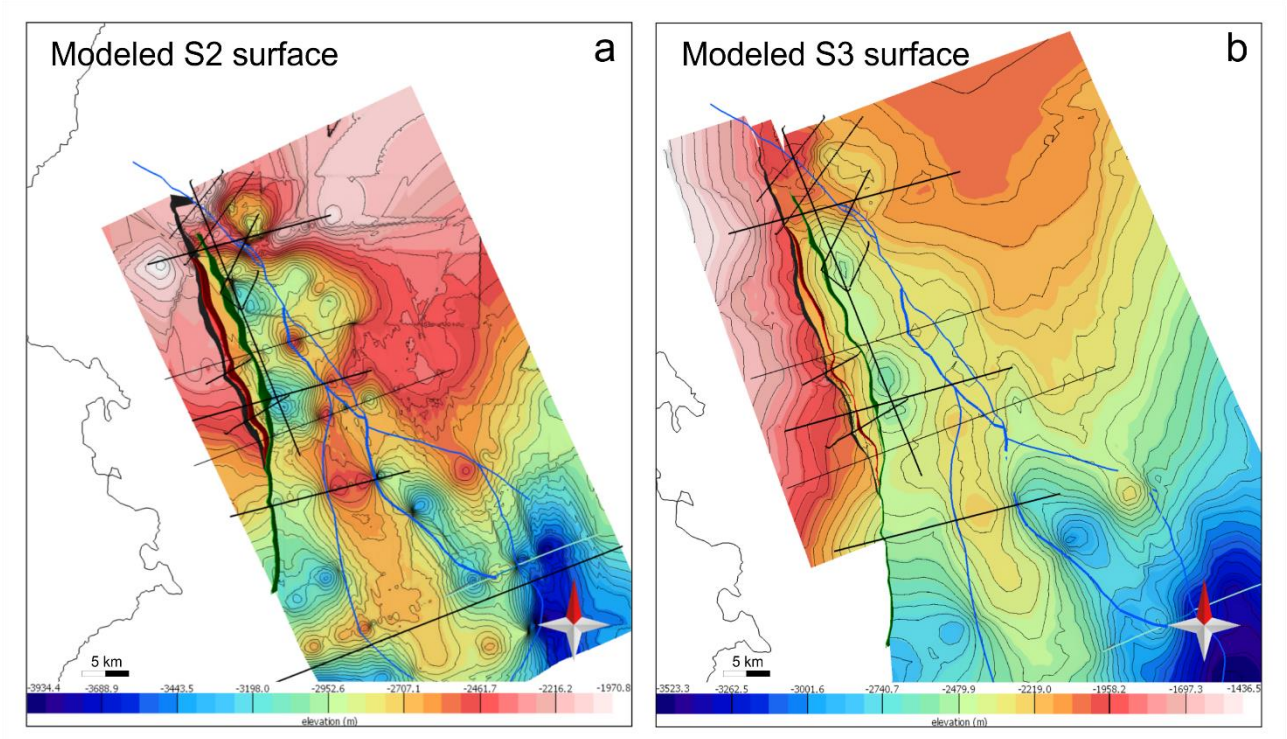

Figure 4.3. Map view of S2 (a) and S3 (b) modelled surface and their relations with MESC faults. Location of seismic lines (black lines) is also reported (see Fig. 2.1 for profiles names).

The surfaces show clear evidence of deformation driven by MESC fault. In fact, depocenters in both surfaces are localized in the central part of F3 fault, where higher offsets are expected. This is mainly visible for S3 surface. Conversely, S2 surface shows two depocenters along the MESC base, the first one, deeper and more evident located in the central part of F3 and roughly overlapping that

one observed in S3, and the second located northward (this is only slightly visible in S3, Fig.4.3). The first depocenter (in the central part of F3 fault) is likely the result of the fault activity which produced more accommodation space and consequently more sediment load. This view is further confirmed by the position of depocenter with respect to the throw diagram reported in Fig. 3.7. The depocenter is, in fact, located between profiles MESC09 and CIR-01 in S2 surface (Fig. 4.3a) which is where F3 and F1 reach their maximum throw with respect to S2 horizon (Fig. 3.7a, b). The same depocenter is located slightly further north in S3 (Fig. 4.3b) between profiles p605 and p607, that is where F1 and F3 manifest their maximum throw with respect to S3 horizon (Fig. 3.7a, b). The depocenter placed further north, between MESC08 and MESC06 is more evident in S2 surface, and it also associated with throw peaks of F1 and F3 diagram. The fact that two depocenters are clearly visible in S2 horizon (Fig. 4.3a) and only one in S3 could be the expression of a longer deformation experienced by S2 with respect to S3. It was noted (see section 3.6) that the three faults nucleated with segmented traces (double-bell shape of throw/distance curve, Fig. 3.7a-c) which then coalesced forming single faults traces; this transition is supposed to have occurred during Pliocene, so only a single depocenter could be recorded by horizon S3 (top of the Pliocene sequence PQ1).

5. Stress analysis and seismotectonic potential

5.1. Expected magnitude

Fault geometric parameters derived from 3D model have been used to estimate the maximum expected magnitude for potential earthquake generated by seismic slip along each fault plane. Many scaling relations among source parameters and magnitude have been proposed over time (Kanamori 1977, Hanks and Kanamori 1979; Wells & Coppersmith 1994; Leonard et al., 2010 among the others). Here, we refer to empirical scaling relations by Wells & Coppersmith, 1994 (WC94) and Leonard, 2010 (L10). The choice of these two references come from the fact that WC94 likely represents the most used and iconic reference for scaling earthquake magnitudes and source parameters, providing a complete range of fault parameters as well (rupture length, rupture area, width, maximum displacement etc.). On the other hand, L10 provides an updated database of earthquakes data even though scaling relations of parameters such as rupture length are not provided. There is a conceptual difference between the two approaches; WC94 put in relation earthquakes Moment Magnitude (M) and fault rupture parameters (rupture length, rupture area etc.), while L10 proposed a self-consistent scaling relation based on Seismic Moment (Mo) on which moment, rupture length, width, area, and displacement can be estimated from each other. We therefore apply both relations and compare the result deriving from WC94 and L10.

The basic concept behind the above-mentioned scaling relations is that a link exists between earthquake size and fault rupture parameters. This link is expressed by the equation:

$$Mo = \mu DLW = \mu DS \qquad \text{(eq. 5.1)}$$

Where **Mo** is the Moment Magnitude, **μ** is the Shear Modulus (commonly taken as 3×10^{11} dyne/cm^2, Hanks and Kanamori, 1979; Wells and Coppersmith, 1994), **D** is the fault average displacement, **L**, is the rupture length, **W** is the rupture width and **S** is the rupture surface.

At the same time, Mo is strictly related to earthquake Magnitude (M) through the equation proposed by Hanks and Kanamori (1979):

$$\boldsymbol{M} = 2/3 * log\ \boldsymbol{Mo} - 10.7 \qquad \text{(eq. 5.2)}$$

If Mo is expressed in [dyne*cm] or alternatively:

$$\boldsymbol{M} = 2/3 * log\ \boldsymbol{Mo} - 6.06 \qquad \text{(eq. 5.3)}$$

If Mo is expressed in [N*m].

It is therefore clear how fault parameters can give an estimation of potential magnitude. It is worth noting that, such an estimation represents the maximum expected magnitude only in the case the fault slip occurs over the entire considered parameter (i.e., rupture length, rupture area, displacement etc.).

Tab. 4.1 summarizes the results of magnitude calculation based on WC94 and L10. For calculation, equations related to normal fault have been used, even if the studied fault are supposed to be oblique. This comes from the fact that WC94 provides only equations related to normal, strike-slip and reverse faults, among which normal fault calculation produces the higher (even though slightly) magnitude estimation.

The results show that F1 and F3 are potentially and geometrically capable of producing earthquakes with magnitude in the range of 6.42-7.04 and 6.5-7.17, respectively. Conversely, the smaller F2 fault can produce M in the range of 5.96-6.89. It is worth noting that, equations based on Surface Rupture Length (SRL) and Rupture Width (RW), put forward comparable magnitudes (for the same fault), while Rupture Area (RA) based calculations give lower estimation of magnitude (both for WC94 and L10). This is probably due to the underestimation of faults area. Classical fault models are, in fact, circular or elliptical (Madariaga, 1976; Nicol et al.,1996; Dong and Papageorgiou, 2003; Kaneko and Shearer, 2015), whereas our faults are rectangular in shape due to the straight lateral

boundaries given by seismic profiles (continuation of fault surface beyond the bounding limit would be no further reliable, increasing therefore uncertainty). The concept of a possible 'missing area' leading to the underestimation of magnitude based on rupture area is explained in Fig. 5.1.

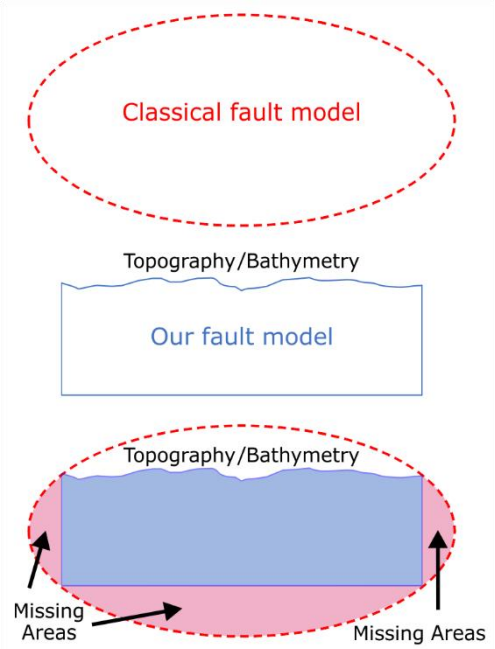

Figure 5.1. Schematic model showing the under-estimation of fault area of our fault model with respect to the classical ones (elliptical, or circular).

Comparison of results achieved by both WC94 and L10 scaling relations shows a good overlap, accounting for less than 0.5% of difference for F1 and F3 estimation and up to 1.23% for F2. In conclusion, estimation of potential earthquake magnitude individually generated by analysed faults, put forward a high seismic potential with F1 and F3 geometrically capable of generating earthquakes with M>7. This result may drive on considering the MESC fault system in the general framework of SE Sicily where historical great to major earthquakes occurred.

5.2. Field data and stress field evaluation

In order to derive the orientation of the main stresses of local stress field, geostructural/kinematic data were collected in six key locations along the Ionian coastal sector of the Hyblean plateau (between Augusta and Syracuse, Fig. 5.2).

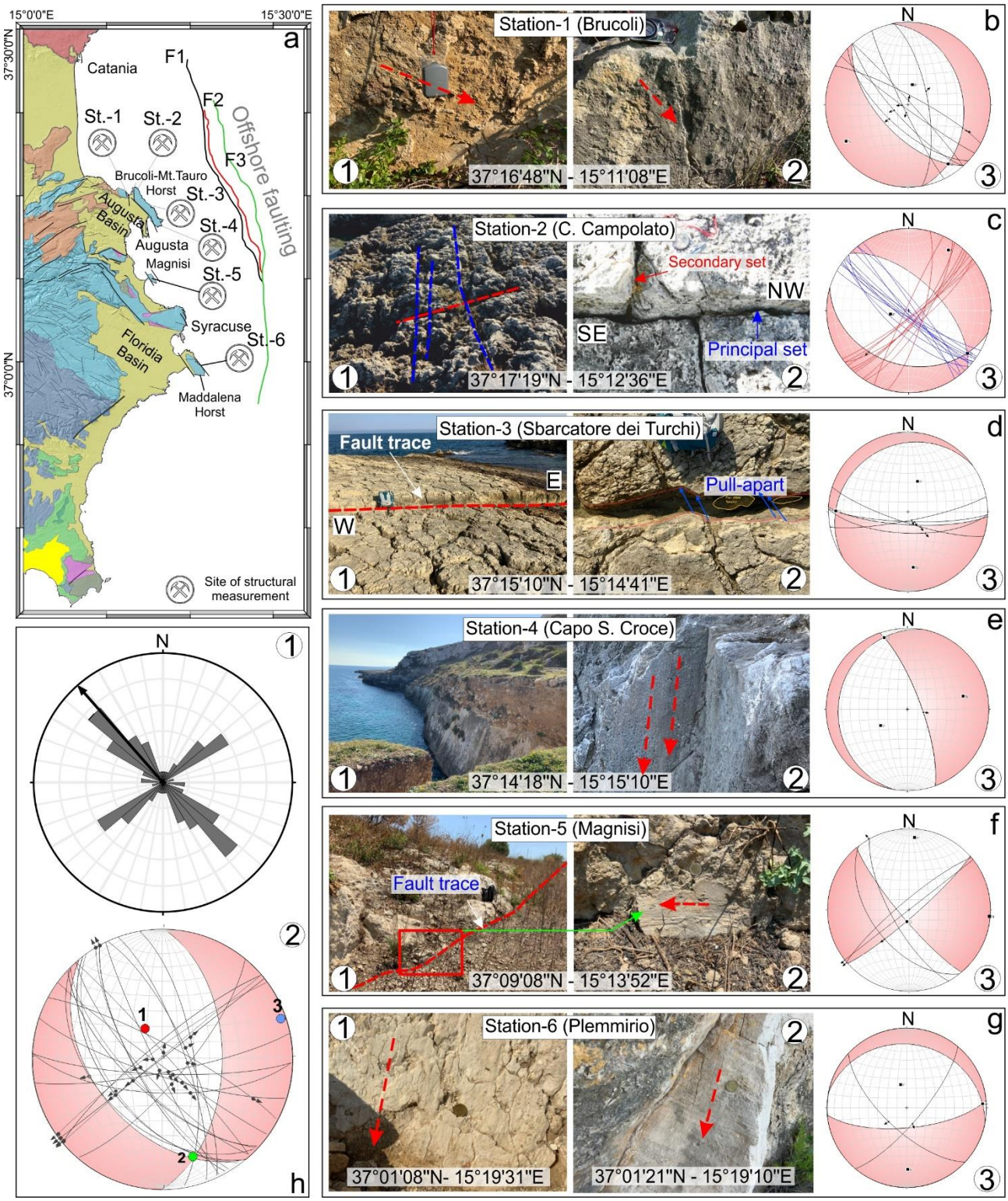

Figure 5.2. a) Map view showing locations of the field kinematic data collected along the coastal sector of eastern Sicily (Malta Escarpment footwall block. (B–G) Collected faults and fractures planes and kinematic indicators. On the right, related pseudo-focal mechanisms (Schmidt lower hemisphere stereographic projections) are also reported. h) Rose diagram of the entire meso-structural dataset (dominant strike N130–140E) and stress field derived from inversion of kinematic data. The latter suggests a slightly transtensional tectonic regime characterized by a ~70° plunging, NNW–SSE trending σ_{max}

The sites in Fig. 5.2 were chosen since they lay on the footwall of the offshore studied faults. As reported in the available geological maps (Carbone et al., 1984; Carbone et al., 1986; Servizio

Geologico d'Italia, 2011), Lower-Middle Miocene carbonates mostly outcrop in the area, unconformably topped by a regressive Quaternary marly-clays, sands, and calcarenites. The investigated sector is structurally controlled by an array of NNW–SSE trending, dip-slip to oblique faults (Fig. 5.2a) producing horsts (i.e., Brucoli–Mt. Tauro, Magnisi, and Maddalena) and grabens (i.e., Augusta and Floridia Basins). These faults are hypothesized to be associated to the offshore faults for their roughly coaxial orientation.

5.2.1. Structural data

The Brucoli-Mt. Tauro area reppresents a horst stucture made up of Miocene and Quaternary deposits deformed by oblique faulting and related fracturing (Fig. 5.2a). In Station 1 (Brucoli area) subvertical (70–80° dipping), NNW–SSE and NW–SE trending fault segments occurs. The faults planes show clear kinematic indicators such as slickenlines and rare tectogrooves (Fig. 5.2b) indicating oblique right-lateral component and dip-slip movement on NW-SE fault plane as well as rare left-lateral component on NNW-SSE fault planes. In Station 2 (Capo Campolato) outcropping limestone are pervasively cut by a system of extensional cross-joints (Fig. 5.2c). Fractures are organized in a ladder-like geometry consisting of a principal continuous set (blue fractures in Fig 5.2c) oriented NW-SE and an orthogonal secondary set NE-SW oriented, whose fractures terminates on the principal one. At Station 3 (Sbarcatore dei Turchi shore) a system of E-W trending, south-dipping faults occurs. The faults show an oblique-normal movement whose left-lateral component has been derived based on observation of piecing point by both sides of pull-apart structures related to fault bending (Fig. 5.2d). Reconstructed slip vector put forward a roughly 70°plunging toward the SE. At Station 4 (Capo Santa Croce) structural measurements were perfomed on a well exposed, 70° dipping, NNW trending fault structure bounding the eastern flank of Mt Tauro horst (Fig. 5.2e). Here, visible kinematic indicators consist of sub-vertical tecto-grooves plunging toward the ESE indicating an extensional slip associated with a slight right-lateral component. Station 5 is located within the Magnisi peninsula, a horst structure bounded by NNW-SSE trending faults. Here, the kinematic

indicators are represented by slickensides, pull-a-part basins and fractures related to strike-slip faults (Fig. 5.2f). Most of indicators (pull-a-part basins and fracture) only gave a qualitatively right-later sense of shear which is confirmed by the few collected slicken-sides (Fig. 5.2f). At station 6 most of the fault planes (mainly NW-SE trending with associated structures oriented NE-SW) did not record kinematic indicators and very few slicken-sides were collected. The poorly constrained structural style indicates normal movement on NW-SE trending, SW dipping faults and oblique, right-lateral sense on NE-SW trending, SE dipping fault planes (Fig. 5.2g).

5.2.2. Derived stress field

Principal (paleo)stress axes (σ1, σ2 and σ3, Fig. 5.2h) were derived from inversion of on-land kinematic structural data (slickensides and tecto-grooves) by mean of directional statistics (e.g., Linked Bingham Analysis, Bingham, 1974) performed using software for stereographic plot analysis (Fautkin, Stereoplot etc., Marret and Allmendinger, 1990; Allmendinger et al., 2011; Cardozo and Allmendinger, 2013)

Main stress tensors from extensional cross-joints (Station 2, Fig. 5.2a, c) were derived considering the orientation of principal and secondary sets. It was observed (Bai and Pollard, 2000; Bai et al., 2002), in fact, how in ladder-like joints system, the direction of the principal set coincides with the direction of main stress axis (σ1) while the direction of secondary joints set overlaps the direction of the least stress axis (σ3, which is therefore perpendicular to the principal joints set). Therefore, we consider the joints as pure extensional structures whose poles represent the spatial orientation of σ1 and σ3 respectively for the secondary and principal sets.

Data analysis revealed for the coastal area a structural stile controlled by slightly (right-lateral) oblique faults generally oriented NNW–SSE (18.75% between N131 and 140E as defined by rose diagram in Fig.5.2h). This fault system developed under a stress field consisting of a N332E oriented, ≈70° plunging σ 1 and a sub-horizontal (4°), E–W oriented (71°) σ3 (Fig. 5.2h and Tab. 5.1).

Inversion of slip data also provides a pseudo-focal mechanism characterized by P-axis and T-axis plunging toward N332E at about 70° and by a sub-horizontal T-axis-oriented N70E (Fig. 5.2h).

Table 5.1. Derived stress field (section 5.2) and mechanical parameters.

Fault	σ_1			σ_2			σ_3			Pore pressure (Mpa)	Cohesion (Mpa)	Friction angle (°)	Young Modulus (Mpa)	Poisson ratio	Friction coeff.
	magnitude (Mpa)	azimuth (°)	dip (°)	magnitude (Mpa)	azimuth (°)	dip (°)	magnitude (Mpa)	azimuth (°)	dip (°)						
F1	63.4	332.3	68.2	36.9	162.8	21.5	25.6	71.4	3.6	26.7	0	30			
F2	42.4	332.3	68.2	27.5	162.8	21.5	17.1	71.4	3.6	16	0	30	27,000	0.25	0.58
F3	67.3	332.3	68.2	43.7	162.8	21.5	27.2	71.4	3.6	28.3	0	30			

Although field data from on-land faults indicate a slight transtensional tectonics deformation, the actual involvement of Quaternary sequences on tectonic deformation remains doubtful; accordingly, the age of last deformation events is not fully determinable due to the lack of clear evidence of faulted Holocene rocks. For this reason, the results here presented, are compared with other published data regarding local stress tensors. The stress field derived (Fig. 5.2h) is consistent with the regional recent kinematic of SE Sicily. In detail the ENE-WSW trending σ3 matches with a good approximation with a) the regional NE–SW to ESE-WNW extension derived from inversion of kinematic data on fault planes (Adam et al., 2000; Monaco and Tortorici, 2000; De Guidi et al., 2013), b) geodetic data (D'Agostino and Selvaggi, 2004; Mattia et al., 2012; Palano et al., 2012), and 3) the local ENE–WSW oriented minimum stress (σh_{min}) deriving from boreholes breakout data from the eastern Hyblean Plateau (Ragg et al., 1999; Montone et al., 2012).

5.3. Slip Tendency analysis

Fault reactivation generally depends upon a variety of parameters including fault cohesion, friction on fault plane, fluid pressure. Nevertheless, a rapid assessment of fault propensity to reactivation can be estimated by the '*Slip Tendency*' analysis (Morris et al., 1996). Slip Tendency defines how a fault surface is close to be reactivated in relation of fault attitudes and applied stress. This analysis derives from the Amonton's law governing the slip movement on a cohesionless plane. Mathematically it is given by the ration between shear and the normal stress acting on a plane, as expressed by the following equation:

$$Ts = \tau/\sigma_n \qquad \text{(eq. 5.4)}$$

Where **Ts** is the *Slip Tendency*, **τ** is shear stress acting on plane and **σ_n** is the effective normal stress ((i.e., the normal stress minus fluid pressure) acting on the plane. In agreement with the assumptions proposed in the Wallace–Bott hypothesis (Wallace, 1951; Bott, 1959) and by mean of the stress analysis tools of Move software 2019.1 (Petex Ltd.), the stress field (σ1, σ2 and σ3) previously derived (see section 5.2.2) was applied to the modeled fault surfaces (Fig. 4.2a) in the 3D MOVE space. The stress magnitude has been defined assuming σ1 as the lithostatic stress (density of rocks and seawater respectively 2600 and 1050 kg/m^3) and confining stress defined at the average depth of each fault (see pressure profiles in Fig. 5.3). Stress field magnitude and elastic parameters are summarized in Tab. 5.1). Results of the Slip Tendency computation indicate the F3 as the fault with the highest tendency to undergo to reactivation along its entire length with a mean Ts of 0.90 homogeneously distributed on the entire fault surface (Fig. 5.3a). F2 also shows a high Ts (mean Ts=0.83) with very high values (red to violet in Fig. 5.3b) occurring over a large portion (but not entire) of the fault plane. Conversely, F1 shows the lowest mean Ts (0.71) with the highest values focused on a limited shallow portion of its fault plane (Fig. 5.3c).

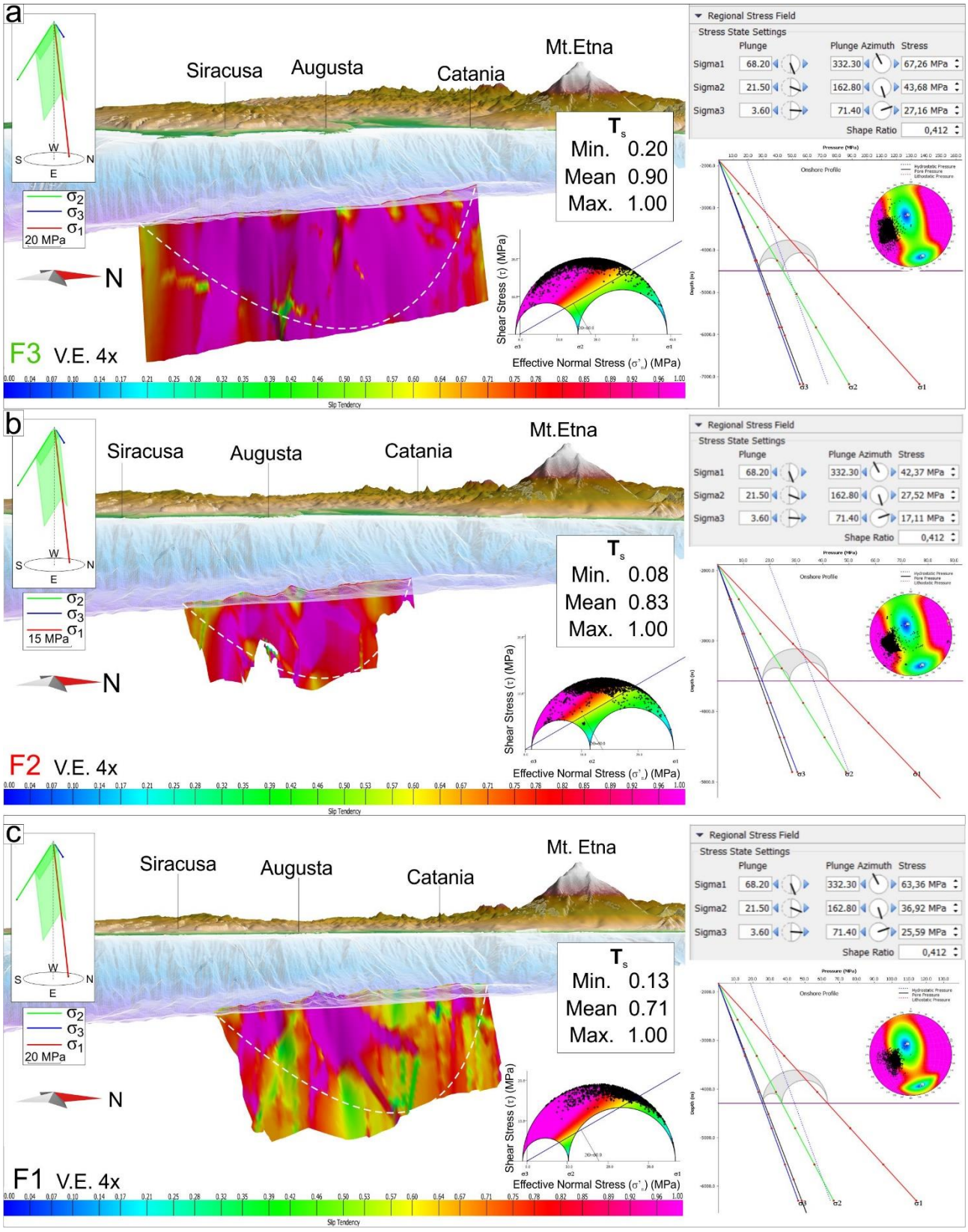

Figure 5.3. Slip tendency analysis carried out on the modelled fault planes (F1, F2 and F3 respectively in a, b, c) by applying the stress field orientation shown in Fig. 5.2h (stress parameters reported in the right panel).

It is worth to note that, in the light of the Slip Tendency analysis, all the three faults are to be considered prone to reactivation, since their mean Ts>0.7. However, the maximum expected

magnitude estimated in section 5.1 could be reached only for fault reactivation occurring over the entire fault segment. In this view, only F3 is potentially capable of generating seismic events with $M \geq 7.0$.

6. Sequential restoration

6.1. Introduction

The sequential restoration (also known as Back-Restoration) is an analytical approach whose scope is to retrace the evolution history of basins or any other geologic/structural context. The restoration concept embraces various methods (structural restoration, cross-sections balancing/validation, back-stripping etc.), whose application is performed to validate previous structural interpretations or to recover basin evolution (deformation, subsidence or other geological process is to be analysed). Since seismic profiles are commonly not associated with borehole data, application of restoration methods provides a powerful approach for the validation of seismic interpretation (Jamaludin et al., 2015; Jitmahantakul et al., 2020), and construction of kinematic structural models (Lopez-Mir et al., 2014; Suppe, 1983; Suppe & Medwedeff, 1990). Restoration methods are commonly based on the 'balanced cross-sections' of Dahlstrom (1969) and Elliot (1983). The term "balanced" refers to the fact that bed length and/or area should be preserved during deformation. Restoration methods are useful for the prediction of geometry at depth (Bally et al., 1966; Chamberlin, 1910; Dahlstrom, 1969; Groshong, 1990; Wang et al., 2017; White et al., 1986; Williams & Vann, 1987), and for analysing available data in order to validate whether they are geometrically plausible and geologically consistent. These methods are usually based on assumptions about the pre-deformation setting and rocks behaviour during deformation in a given tectonic context (Dahlstrom, 1969). Since the early studies of Bally et al. (1966) and Dahlstrom (1969), cross sections balancing was applied to restoration of seismic section for validating structural interpretation and for predicting the geometry at depth in both extensional (Gibbs, 1983, 1984; Groshong, 1990; White et al., 1986; Williams & Vann, 1987) and contractional settings (Boyer & Elliot, 1982; Hossack, 1979; Suppe, 1983; Suppe & Medwedeff, 1990). Recently, due to the increasing computational power of modern computer, significant acceleration occurred in section modelling and restorations (Gratier et al., 1991; Maerten, 2007, among many others). The technological progress, led to application of

methods such as structural balancing and horizon flattening to rectify or to validate seismic interpretation in extensional settings (Jamaludin et al., 2015) or to calculate extension in various rift phases (Jitmahantakul et al., 2020). The above summary demonstrates how these methods represent powerful approaches for analysis of basin deformation. Moreover, they provide further information on how deformation has evolved through time in various tectonic contexts (extensional, compressional, or composite).

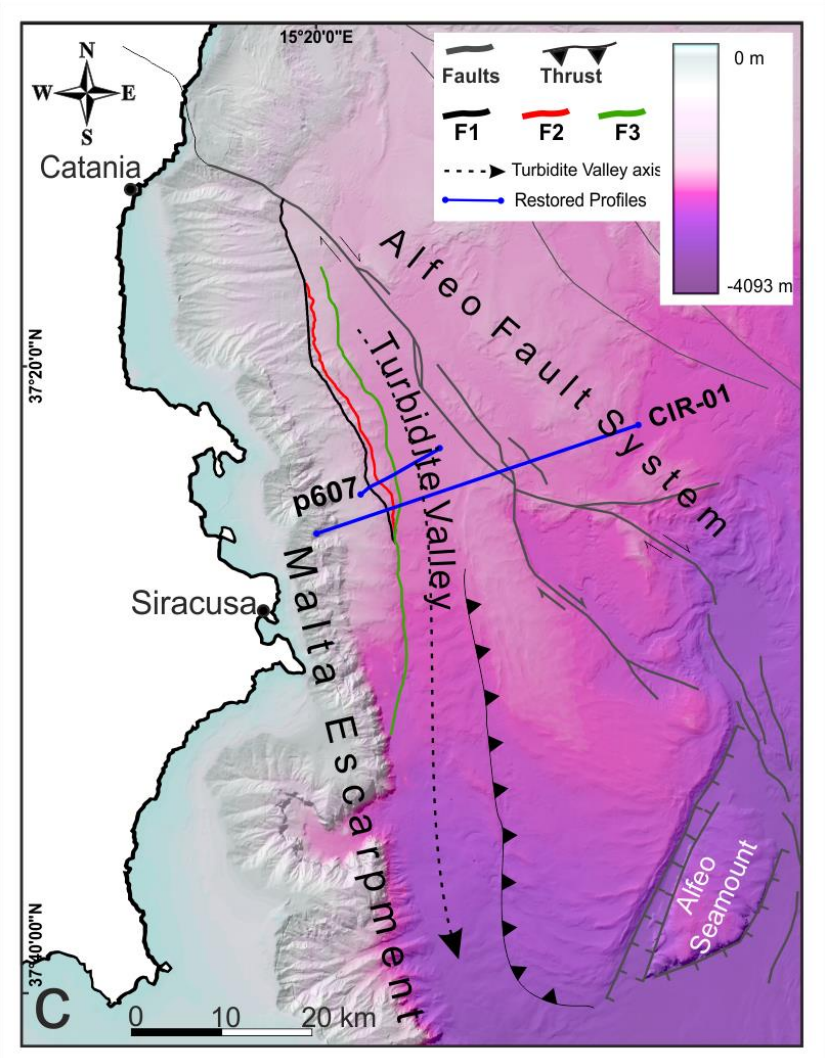

Figure 6.1. Location of Seismic profiles selected for the sequential restoration (blue lines). Mod. after Gambino et al. (2021b).

In the following, sequential restoration methods were applied on two Time/Depth converted, high-resolution seismic profiles (See section 3 and Gambino et al., 2021b - Fig. 6.1 and 6.2) appropriately chosen. The choice is based on their high-resolution and since they transversally cross the MESC faults in the central part of F3 fault, considered to be the main and most active fault of the

MESC system (see section 3). The goal of the sequential restoration is threefold, (1) validate/correct the previous seismic interpretation, (2) analyse fault activity, associated extension and slip rates through-time, and (3) analyse basin deformation history to get a deeper view on processes involved. Restoration methods performed on modelled profiles include various steps, such as sediment unloading and decompaction (Fig. 6.3c), isostatic adjustments (Tab. 6.1), erosion restoration (Fig. 6.3a, b), structural restoration and unfolding which are discussed in detail in the following section.

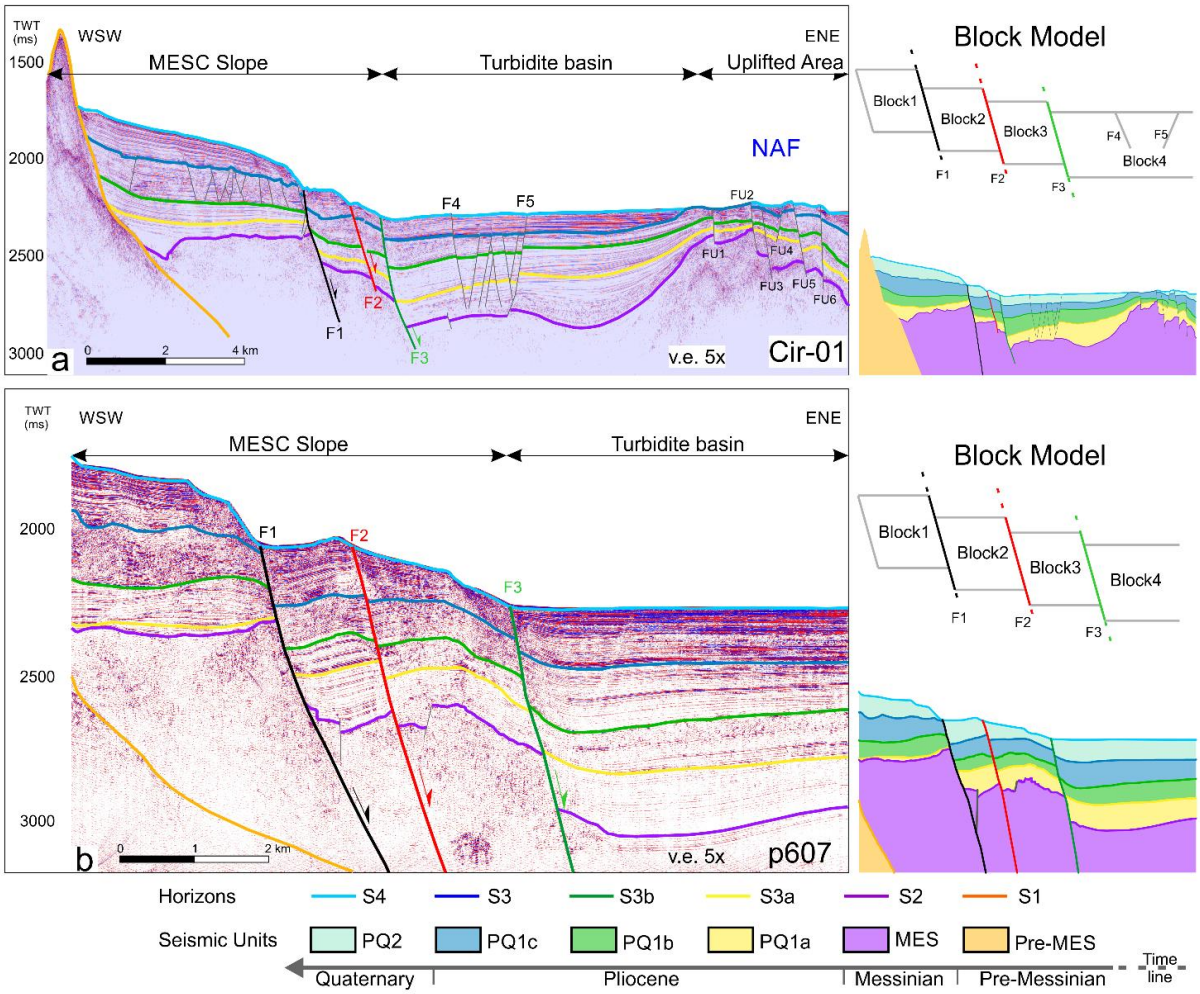

Figure 6.2. Tectono-stratigraphic models of (a) CIR-01 and (b) P607 profile. Three sectors are identified within the models: MESC slope, turbidite basin and uplifted area (corresponding to the North Alfeo Fault system). From Gambino et al. (2021b).

6.2. Methods and workflow

The Back-Restoration has been carried on two high-resolution seismic lines (Cir-01 and p607 profiles, see Fig. 6.1c for location) properly chosen from our dataset (see section 2). These profiles have been chosen as they cross the central part of the F3 fault, the main and most active fault of the

system (see section 3 - Gambino et al., 2021b). For its structural/geometric complexities and according to Schultz-Ela, (1992), the interpreted tectono-stratigraphic model (see section 4) has been simplified into four continuous blocks bounded by the F1, F2, and F3 faults (Fig. 6.2 right panel). Block 1 is the footwall of the F1 fault, Block2 represents both the F1 hanging wall and the F2 footwall, Block 3 is both the F2 footwall and the F3 hanging wall and, finally, Block4 represents the F3 hanging wall.

The workflow here presented consists of the following 7 steps applied for each restoration cycle (for each seismic unit):

a) Seismic-stratigraphic and Structural interpretation of seismic profiles (already performed and discussed in section 3)

b) Time-depth conversion of seismic profiles (performed and discussed in section 3)

c) Unloading of top horizon and Decompaction of underlying units

d) Restoration of isostatic response to the unloading of upper layer (Isostasy Balancing)

e) Replacement of erosion (if any)

f) Structural restoration (Fault restoration)

g) Unfolding of horizons to a given Datum (regional or local)

Steps c-g represent one restoration cycle. At each cycle, steps are referred to the uppermost unit. Unloading (c) and isostacy balancing (d) refer to the load of the upper unit on the lower ones. Erosion restoration (e) and unfolding refer to basal surface of the top unit. Finally, structural restoration (f) is performed by moving the fault footwall and hangin wall with respect of the upper bounding surface of the top unit. Faults parameters (throw and heave) are the vertical and horizontal components of the restored fault slip.

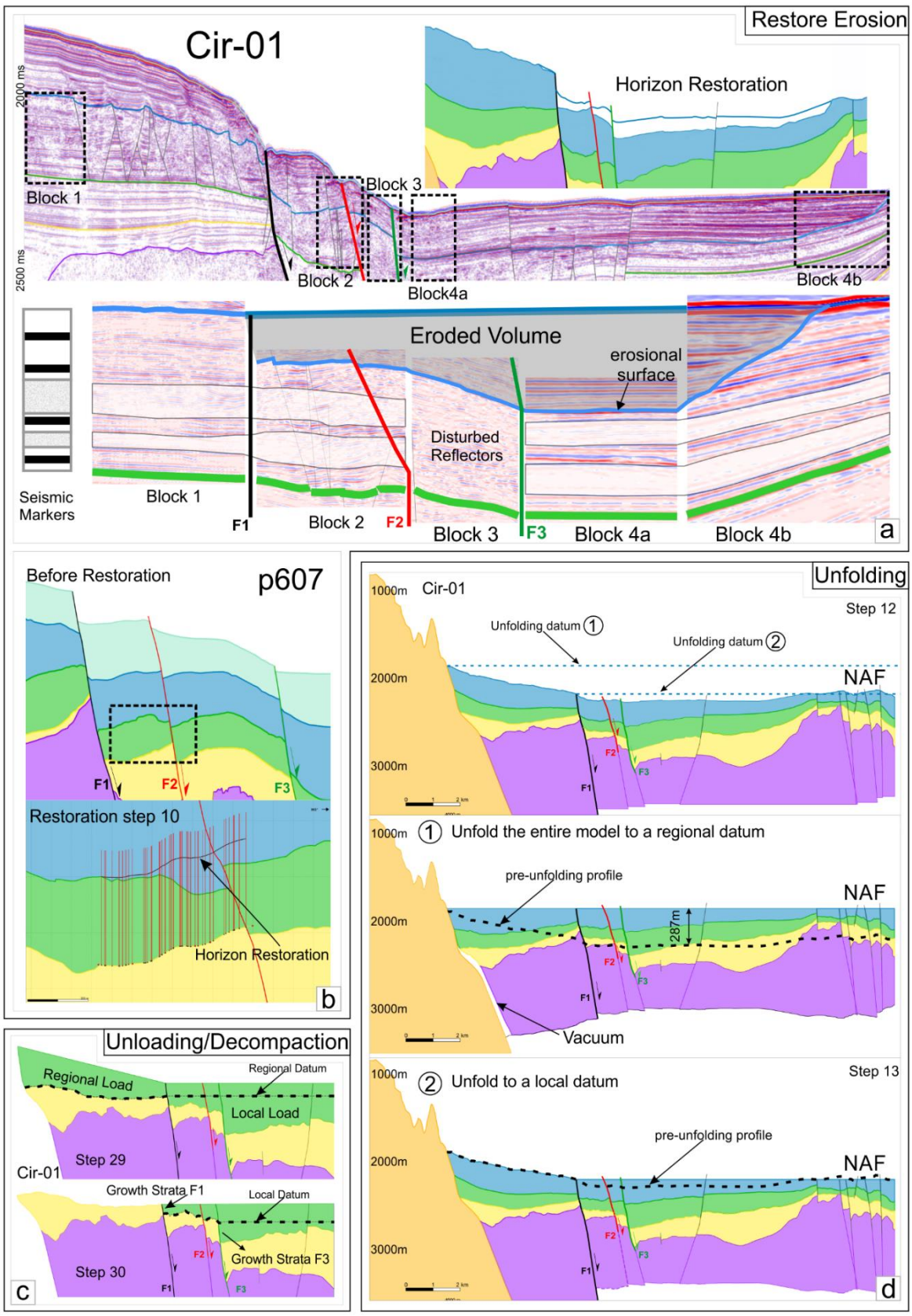

Figure 6.2. Main highlights of restoration. (a) Restoration of erosion of the PQ1c unit (CIR-01 line). (b) Restoration of erosion of the PQ1b unit (P607 profile). (c) Unloading of the upper unit and decompaction of underlying ones. For units with variable thickness across-fault (growth-strata) a regional load (acting on both the FWl and HW of the fault) have been considered, while a local load (only on the hangingwall) has been considered for the growth package (see text). (d) Unfolding of seismic units (CIR-01). Two data have been tested since no paleo-bathymetric information is available. Datum 2 is considered the most reliable (see text for description).

6.2.1. Unloading/Drcempaction

Unloading and decompaction are performed in a single step using the 'Decompaction tool' (Move software, Petex ™).

While sediments accumulate above older rock units, the latter undergo burial compaction. During restoration, unloading by removing the top unit means removing also the part of the burial load. To simulate this, underlying units must be decompact honouring, so, the actual sedimentary evolution. At every restoration step, the sedimentary units (underlying the upper one) are decompact by removing the top unit. The amount of decompression is strictly dependent on density (i.e., weight) of the top unit but it also depends on porosity, depth and depth coeff. (Sclater and Christie, 1980) of the underlying horizon that is to be decompressed. For this reason, some rock properties have to be defined. Since no well data is available for the studied area, rock properties are inferred from the lithological interpretation achieved from seismic stratigraphy and correlations with literature (Scandone et al., 1981; Micallef et al., 2019; Gambino et al., 2021a). Rock types and related geotechnical parameters (surface porosity, porosity at depth, density etc.) are reported in Tab. 3.1. Decompression is based on the equation provided by Sclater and Christie (1980) and represents the porosity difference between the porosity of a rock at the surface and the porosity that the same rocks would have at a given depth. This relation is expressed by the equation:

$$f = f_0(e^{-cz})$$

Where:

- **f** is the porosity at depth
- $\mathbf{f_0}$ is the porosity of rock at surface.
- $\boldsymbol{e}$ is the base of natural logarithms
- **c** is the depth coefficient (km^{-1})

- **z** is the depth (m)

For units with a relatively constant thickness across a fault, decompaction generally refers to a regional datum (usually the base of the top unit). For units with variable thickness across a fault (i.e., growth strata, Fig. 6.3c), the differential loading between the footwall and the hanging-wall should be considered. This means that growth packages would produce a greater load on the hanging-wall than on the footwall with a consequent difference in compaction. Indeed, as a fault slips, the increasing accommodation space on the hanging-wall lead to a thicker sedimentary infilling whose load has not effects on the footwall (Lopez-Mir et al., 2014 and reference therein). Consequently, the decompaction of units showing growth strata is achieved in two steps (Fig. 6.3c); 1) decompaction of a unique regional loading for both the footwall and the hanging wall blocks, and 2) decompaction of loading related to the remaining growth package affecting only the hanging-wall. For the first step, I considered a regional datum coherent with the base of the top unit in the footwall. Sediments above this datum produce the general loading affecting footwall and hanging wall. On the other hand, sediments below the given datum (growth strata) would weigh only on the hanging-wall with any effect on the footwall (Fig. 6.3c).

Units without consistent thickness variation across-fault are unloaded in a single step using only a regional datum.

Commonly, units representing salt deposits are removed from the model before the restoration because salt may be deformed (if under loading) in a ductile way that could include migration out of the section. This does not respect the rule of area conservation and, so, restoration cannot be performed. In our profiles, the MES unit represents the Messinian sequence, which incorporates salt layers (Lofi et al., 2011; Butler et al., 2015; Micallef et al., 2019). To avoid decompaction of such a layer, I attributed it a porosity value of zero (see Tab. 1) and MES unit was not removed during restoration. In fact, since MES unit is the lowest unit of the model, it does not compromise the

restoration of the upper units, providing, in addition, a reference for comparison between pre- and post-restoration.

6.2.2. Isostasy Balancing

The vertical isostatic response due to crustal buoyancy should be evaluated, in order to compensate the vertical position due to unload. For short sections (our section are only 23 and 11 km respectively for Cir-01 and p607) "Airy isostasy algorithm" (Airy, 1855) is preferred rather that the "flexural isostacy" since it represents the easiest model of isostatic compensation. The mean isostasy value is calculated by the software on the basis of unit density. Isostatic compensation consists of a vertical shift of the entire model after unloading of the top horizons is applied (stripping). Non-application (or erroneous estimation) isostacy do not compromise the model restoration but only its vertical position. The advantage of isostatic balancing is to offer a consistent restoration of basin providing additional paleo-bathymetric information. Isostatic parameters applied for each unload are reported in Tab. 6.1.

Table 6.1. Isostatic adjustment correction performed after unloading of top unit at each restoration step.

	Isostatic Response (m)			
	PQ2	PQ1c	PQ1b	PQ1a
Cir-01	28.5	74.2	66.4	74.8
p607	47.5	63.4	55.9	64.9

6.2.3. Restoration of eroded horizons

Since it has been observed that some units are truncated by an erosional surface (e.g., S3, see section 3), it is important to take into consideration the amount of lacking portion, in order to provide a consistent restoration. In this respect, important information are provided by the analysis of internal seismic stratigraphy (reflectors) of the considered unit. PQ1c shows, in fact, evidence of erosional truncation of Block4a (Fig. 6.3a) where almost half of the unit is eroded. Conversely, in Block1 the sequence seems to be rather complete and, no reconstruction is needed. In addition, this feature

indicate that erosion occurred mostly at the MESC base likely suggesting it is the result of the turbiditic nature of the basin filling sediments.

To reconstruct the PQ1c unit, we used the lower PQ1b top reflector (S3b) as a refence and a further constraint given by the truncated reflectors observed at the culmination of the uplifted area (Block4b). This reconstruction could be underestimated as erosion could have removed a portion larger than the reconstructed one with its seismic stratigraphic record being no longer visible.

6.2.4. Structural restoration

At this stage, fault activity is restored using the 'Move-on-fault' tool. Due to the non-planar fault plane geometry (dips get less steep downward) and considering the horizons termination toward the F3 fault (slight roll-over anticline), a 'simple shear algorithm' has been applied for restoration of extensional faults. The shear vector (representing the linear connectio of each point on the hanging-wall to the fault plane) is empirically defined in order to maintain the hanging-wall as flat as possible; this is consistent, since the sediments are theoretically horizontal before the deformation induced by the fault slip.

6.2.5. Unfolding

This tool is used to unfold horizons to a pre-deformation state (horizontal or inclined). The residual folding related to fault activity or to gravitational accommodation, is restored using the 2D Unfolding tool. A simple shear algorithm is used since the study area has been deformed by extension. At each step, the top horizon is taken as a reference for the unfolding datum (Fig. 6.3d). Since no paleo-bathymetric data is available, and due to the turbiditic nature of the sedimentary unit (Gutscher et al., 2016), a flat regional datum is used.

The F1 footwall (Block1) manifests horizons dipping toward the basin (Fig. 6.2). In addition, horizons (especially, PQ1a, PQ1b, PQ1c) show an upward concavity, which gets more evident downwards (from S3 to S3a – Fig. 6.2). Two processes have likely occurred producing such a

deformation: 1) sediments originally deposited horizontally were bent by deep-seated instability (Gambino et al., 2021a, b) and/or a slip along the S1 surface caused a drag fold, or 2) sediment supply from the MESC slope (Fig. 6.1) produced strata slightly dipping toward the basin, then, accumulation and compaction deformed lower units.

To consider both possibilities and compare results, two different restorations are performed for Cir-01 profile. The first one is performed considering a flat datum for the entire sequence (Fig. 6.3d). The second one is performed by dividing the sedimentary sequence in two portions, which are 1) the basal MESC slope (westward of F1) and 2) the proper turbidite basin (eastward of F1) as described in Fig. 6.3d.

Since the first restoration (datum 1 in Fig. 6.3d) would account for a vertical component (up to 287 m) geologically not reliable we tend to the second restoration. The sediments source for Block1 is, in fact, partially upslope (Fig. 6.1c) as testified by scars and canyons across the slope, admitting inclined deposition. For this reason, units placed on the Block1 have been unfolded using an inclined datum (Fig. 6.3-d2).

6.2.6. Limitations

As described in section 3, chrono-stratigraphy is not well constrained. Even if some seismic reflectors are strongly recognizable (S2 and S3) and an abundant literature is available (e.g. Messinian sequence, Lofi et al., 2011; Butler et al., 2015; Micallef et al., 2019; Camerlenghi et al., 2019), some uncertainties still persist about ages and correlation of other units (PQ2 and PQ1a, b see section 3.1 of the text).

6.3. Tectonic-stratigraphic model

The seismic stratigraphy described in section 3 consists of four main seismic units (Pre-MES, MES, PQ1 and PQ2) bounded by four stratigraphic limits (S1, S2, S3 and S4 representing the seafloor). To better constrain the sequential restoration, providing more details on deformation

evolution, the PQ1 was further subdivided in three sub-units (PQ1a, PQ1b and PQ1c respectively from the base to the top of the unit). Accordingly, two additional discontinuities have been detected (S3a and S3b). Stratigraphy and related units' parameters (as discussed in section 3) are reported in Fig. 6.2 and 6.1.

Although the further subdivision of PQ1 unit allows increasing the resolution on basin evolution analysis, on the other hand, their actual age intervals are totally unknow. Being the PQ1 unit Pliocene in age, the sub-units PQ1a, PQ1b and PQ1c have been discretionary attributed to lower, lower-upper, and upper Pliocene time respectively (Tab. 3.1). For its stratigraphic position, the sub-units are correlated with the Pliocene sedimentary sequence defined by other authors (Camerlenghi et al., 2019; Micallef et al., 2018). According to the literature and in the light of the internal seismic facies, the sub-units are imaged as a stratigraphic succession of siltstone, silty sandstones, calcilutites and marls.

The structural setting of model extensional belt consists of three main faults representing the active portion of the Malta Escarpment (F1, F2, and F3), the graben faults affecting the proper turbidite basin, and a set six faults representing part of the strike-slip NAF system resulting in an elevated bathymetry (uplifted area of Argnani and Bonazzi, 2005).

6.4. Sequential restoration

The workflow described in section 6.2 has been applied to the tectonic-stratigraphic model in order to stripping back the experienced basin deformation. Fault parameters (throw and heave, being the vertical and horizontal components of fault respectively) have been quantified at each restoration cycle (Tab. 6.2a and Tab. 6.2b for CIR-01 and p607 respectively). Then, the sum of faults throws (cumulative throw) and heaves (cumulative extension) is calculated to indicate the total vertical and horizontal variation experienced by the whole section.

Table 6.2a. Recalibrated faults displacement parameters (CIR-01 modelled section) by mean of sequential restoration. Cumulative extension experienced by the entire section in also reported.

Cir-01

Restoration Step	Name	F1			F2			F3			MESC Extension	MESC Throw (m)	Cumulative Extension (m)
		Heave	Slip	Throw	Heave	Slip	Throw	Heave	Slip	Throw			
03	PQ2	50.72		68.30	27.40		24.10	26.79		31.40	104.92	123.80	NONE
	PQ1c	77.75	165.66	146.20	54.92	64.57	33.74	16.97	36.97	32.85	149.63	212.79	
	PQ1b	142.26	211.89	153.89	44.59	61.43	42.15	46.93	76.44	60.08	233.78	256.12	
	PQ1a	222.64	295.11	190.95	53.84	67.41	40.38	114.89	198.92	160.94	391.38	392.27	
	MES	283.69	392.69	268.79	109.95	165.89	119.13	282.63	365.62	224.56	676.26	612.48	
07-12	PQ1c	36.63	78.40	69.23	26.27	33.24	20.36	20.22	37.79	31.92	83.12	121.51	126.8
	PQ1b	109.50	168.31	125.34	45.16	63.56	44.61	46.29	77.14	61.47	200.96	231.42	
	PQ1a	222.66	294.86	190.56	48.77	61.59	37.48	117.44	206.65	168.39	388.86	396.43	
	MES	283.69	392.95	268.89	109.93	166.68	120.15	282.63	366.21	225.45	676.25	614.49	
20-27	PQ1b	25.77	49.76	42.54	21.47	32.67	24.58	16.03	27.72	22.61	63.27	89.73	206
	PQ1a	107.87	149.11	101.34	28.66	37.46	24.12	81.40	144.80	118.85	217.94	244.31	
	MES	191.87	255.50	166.65	90.01	133.96	94.37	238.54	317.55	203.68	520.43	464.69	
35-42	PQ1a	56.37	77.67	51.62	3.32	4.38	2.86	62.75	121.74	103.78	122.44	158.27	368.8
	MES	145.92	189.58	120.91	74.41	106.64	71.13	207.08	285.39	190.92	427.41	382.96	
43-48	MES	85.61	114.38	75.77	84.75	109.41	64.32	87.93	142.43	111.52	258.29	251.62	784.3

Table 6.2b. Recalibrated faults displacement parameters (p607 modelled section) by mean of sequential restoration. Cumulative extension experienced by the entire section in also reported.

p607

Restoration Step	Name	F1			F2			F3			Corrected Heave (m)				Corrected Throw (m)				Cumulative Extension (m)
		Heave	Slip	Throw	Heave	Slip	Throw	Heave	Slip	Throw	F1	F2	F3	Tot	F1	F2	F3	Tot	
05	PQ2	69.89		68.20	38.86		50.40	22.94		29.90	69.89	38.86	22.94	131.69	68.20	50.40	29.90	148.50	NONE
	PQ1c	199.41	310.20	235.63	48.56	78.66	61.84	35.30	65.73	55.39	120.73	48.56	35.30	204.59	117.82	61.84	55.39	235.05	
	PQ1b	210.04	324.84	245.36	11.84	19.52	15.52	71.29	128.89	105.88	210.04	11.84	71.29	293.17	245.36	15.52	105.88	366.77	
	PQ1a	244.09	363.43	267.23	56.84	93.55	74.30	156.50	222.85	158.46	244.09	56.84	156.50	457.43	267.23	74.30	158.46	499.99	
	MES	429.09	593.85	404.69	73.33	106.33	76.92	155.07	300.23	254.85	429.09	73.33	155.07	657.49	404.69	76.92	254.85	736.45	
06-08	PQ1c	199.40	307.37	231.69	48.56	78.26	61.31	35.24	63.99	53.36	118.71	48.56	35.24	202.51	115.84	61.31	53.36	230.52	158
	PQ1b	210.02	327.23	248.34	11.84	20.47	16.70	71.28	134.23	112.14	210.02	11.84	71.28	293.14	248.34	16.70	112.14	377.18	
	PQ1a	244.06	364.90	268.87	56.84	97.10	78.73	156.49	228.19	165.87	244.06	56.84	156.49	457.40	268.87	78.73	165.87	513.47	
	MES	429.05	595.73	407.22	73.33	106.81	77.59	155.11	300.85	255.11	429.05	73.33	155.11	657.49	407.22	77.59	255.11	739.92	
12-13	PQ1b	22.64	38.08	30.53	44.05	51.46	26.18	23.17	41.63	34.55	22.64	44.05	23.17	89.86	30.53	26.18	34.55	91.26	297.5
	PQ1a	47.28	95.55	82.55	15.70	21.81	15.14	72.57	103.59	73.92	47.28	15.70	72.57	135.54	82.55	15.14	73.92	171.61	
	MES	190.18	319.06	254.60	16.31	27.33	21.93	103.64	192.26	159.42	190.18	16.31	103.64	310.13	254.60	21.93	159.42	435.95	
15-16	PQ1a	45.29	58.28	36.56	0.00	0.00	0.00	45.29	58.28	36.56	45.29	0.00	45.29	90.57	36.56	0.00	36.56	73.12	342
	MES	170.75	287.74	229.57	0.00	0.00	0.00	87.86	150.49	119.50	170.75	0.00	87.86	258.61	229.57	0.00	119.50	349.07	
17-19	MES	132.80	228.00	183.50	0.00	0.00	0.00	62.30	91.40	66.40	132.80	0.00	62.30	195.10	183.50	0.00	66.40	249.90	506.4

6.4.1. CIR-01 restoration

Restoration of CIR-01 seismic section involved 48 steps among which the salient ones (described in the following rows) are summarized in Fig. 6.4 and Tab.6.2a.

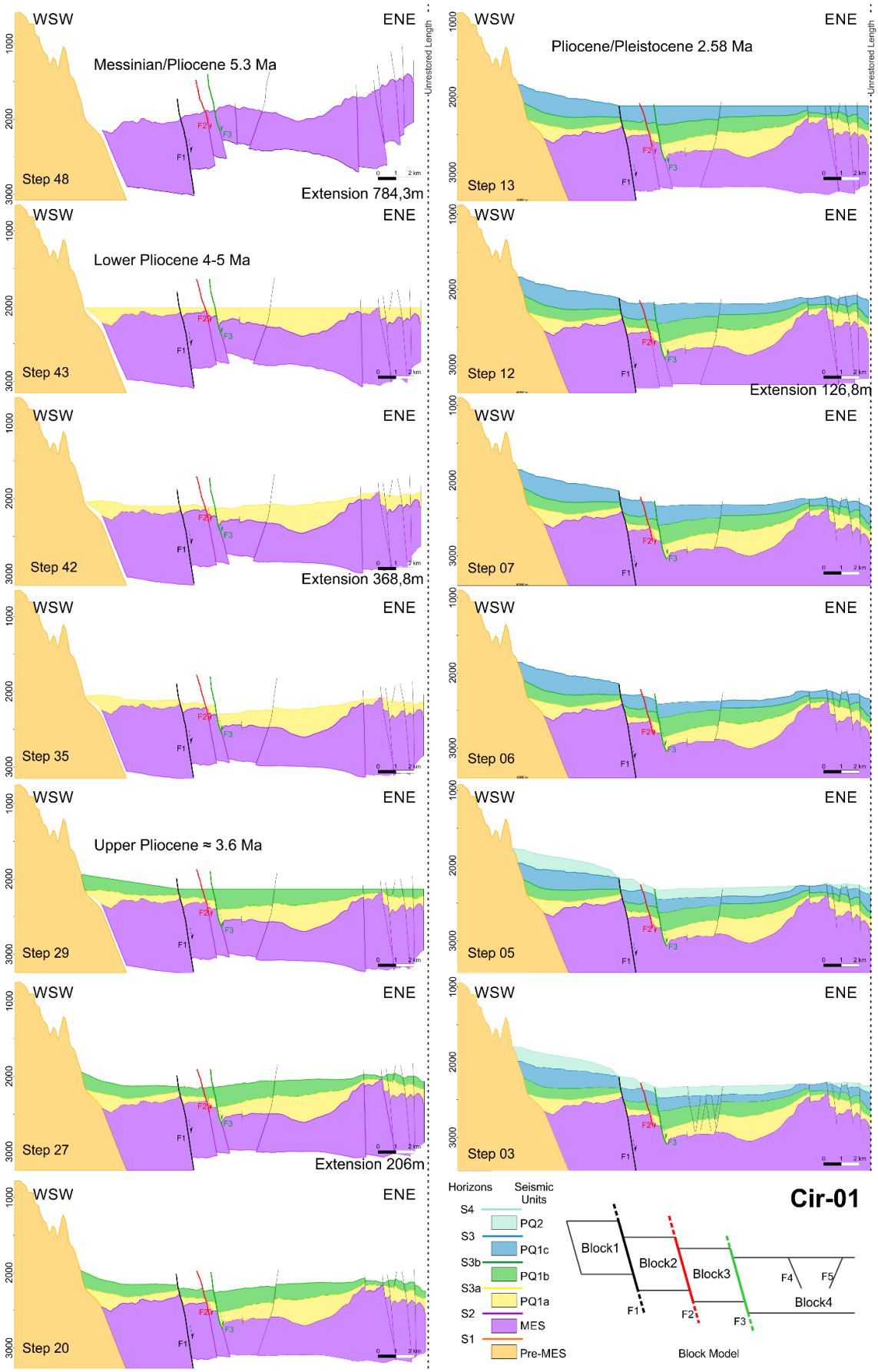

Figure 6.4. Restoration sequence of CIR-01 model. Bottom-right is the present-day configuration. Inferred ages and amount of extension are reported (Gambino et la., 2021b).

After section preparation (interpretation and time/depth conversion, step-01 and step-02 respectively), restoration starts at step-03 representing the current configuration. At this step, the model shows block4 being deformed by the graben structure and NAF fault in the uplifted area (Fig. 6.2 and 6.4). The graben is the youngest structure (see section 3 and Gambino et al., 2021a) since the forming faults show a general constant offset with depth. Instead, F5 (the easternmost fault of the graben) increases its offsets with depth, suggesting its older activity. That is why after the first structural restoration all the graben faults disappear except F5 (see step-05 in Fig. 6.4). At step-06 PQ2 unit was unloaded, and lower units have been decompact accordingly.

In step-07 erosion of PQ1c was estimated by analysing its internal seismic reflectors (Fig. 6.3b). In Fig. 6.3b, seismic stratigraphy of block1 and block4b compared to that of block2, block3 and block4a points to a partial lacking the sedimentary sequence relative to blocks 2, 3 and 4a. Block4a results the portion which undergone greater truncation, estimated in about one third of the original thickness. Within block3, the reflectors are not continuous due to its local chaotic seismic facies, so, erosion has been estimated also with respect of the adjacent blocks 2 and 4a. Block1 and block4b are instead considered complete sequences since no erosion can be inferred. On this basis, restoration of S3 horizon have been performed considering, as well, the geometry of the basal PQ1c horizon (S3a).

In step-12, faults are restored referring to the S3 horizon. Some of the faults located on the uplifted area (FU2, FU3 and FU5) show offsets matching also for S3a and S3b (Fig. 6.2a and 6.4). This indicates that their Pliocene-Quarternary succession has been (vertically) displaced after the formation of S3 (likely in the last 650 ka, see section 3.3 and Camerlenghi et al., 2019). At this stage total extension experienced by the section is about 127. At step-13 unfolding is applied to all the units with respect to the S3 horizon. Two data have been used to define the better unfolding approach for the inclined units of block1, adjacent to the MESC slope (Fig. 6.3d). Finally, the second approach is preferred since it is geologically more reliable (Fig. 6.3-d2). In step-20, PQ1c were unload and underlying units have been decompressed accordingly. In step-27, faults were restored relatively to

S3b horizon achieving a total extension of 206m. In step-29, unfolding is performed for S3 horizon. It is to note that unfolding results in decoupling of seismic units from the lower S1 horizon (and pre-MES unit). This effect is related to the concept of 'area/length conservation' (described in section 6.1 and 6.2 – Chamberlin, 1910). This feature could be related to sediments accommodation due to progressive loading. This interpretation also explains the upward concavity (in Step-03, Fig. 6.4) of S3a, S3b and (slightly visible) S3 horizons within block1. Otherwise, decoupling can be charged to a layer-parallel extension producing a volume loss due to an out-of-section deformation (Bahroudi et al., 2003). In step-35, PQ1b unit was unloaded, and underlying units decompressed. Fault restoration at step-42 resulted in a total section extension of about 369 m. Any noteworthy effect has been observed after, unfolding (with respect to S3a horizon) at step-43. Finally, fault restoration at step-48 pointed out to a total extension recovery of about 784 m for the modelled section. Moreover, the final stage of restoration shows a strongly curved S2 horizon and related MES unit. This feature (discussed below) should be the result of a possible ductile deformation experienced by MES units due to its (partial) hyaline nature.

6.4.2. P607 restoration

Restoration of p607 profile involved 19 steps, among which the most remarkable are reported in Fig. 6.5.

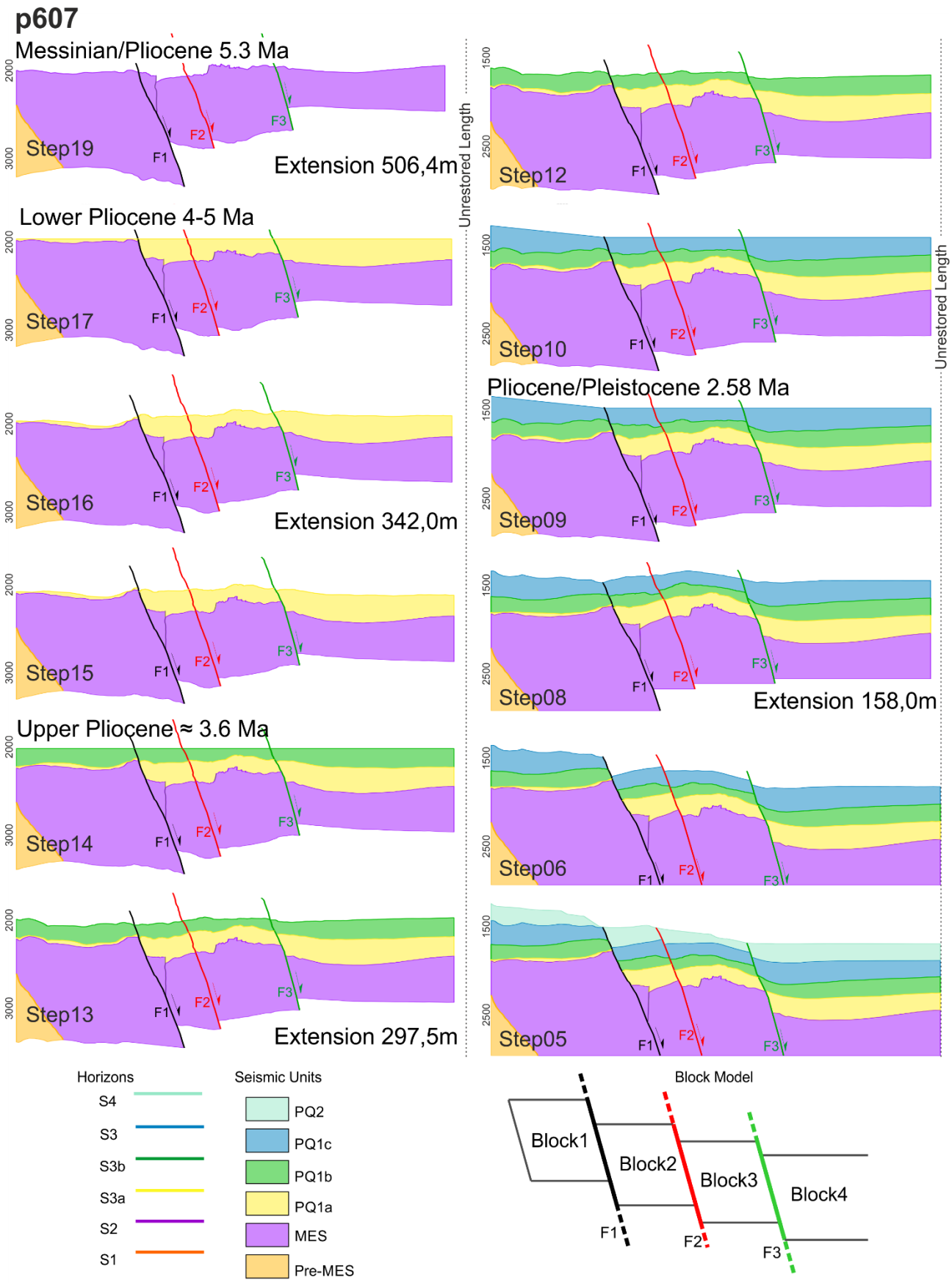

Figure 6.5. Figure 6.4. Restoration sequence of p607 model. Bottom-right is the present-day configuration. Inferred ages and amount of extension are reported (Gambino et la., 2021b).

The proper restoration starts with step-05 (after profile preparation and conditioning). At step-06 top unit PQ2 is unloaded, and lower units decompressed accordingly. As described in section 6.2, unloading of growth strata is performed separately from the regional load. No erosional restoration has been performed on S3 horizon since no truncation is detectable on seismic reflectors. This can be charged to the presence of a paraconformity hiding the erosional surface (see Fig. 6.2b), or also to the absence of an actual erosional surface. P607, in fact, has been acquired in proximity of a ridge bounding a canyon perpendicular to the MESC slope. Conversely, CIR-01 lays within the above-mentioned canyon, possibly implying a different amount of erosion for the relatively close (2-3 km) sub-parallel seismic lines. Fault restoration performed at step-08 pointed out to the inconsistency of S3b horizon (green) in block 2 (which is corrected at step 10) as shown in Fig. 6.3b. Here, the offset of F2 relatively to S3b horizon is not consistent with a normal fault kinematic (footwall is lower than the hanging wall). Since this feature is not observed for others horizon, it is likely due to local erosion (fault scarp instability). At this stage the amount of section extension is 158 m. At step-10 restoration of eroded S3b is performed using the lower S3a horizon as a template (Fig. 6.3b). Unloading/decompaction, faults restoration, and unfolding are performed respectively at steps 12, 13 and 14. At step-15, PQ1b unit is unloaded, and lower units decompressed. At step-16 faults are restored with respect to S3a horizon accounting for a total section restoration of 342 m. It is worth to note that F2 does not produce offset in S3a reference line, suggesting that it likely nucleated after deposition of PQ1a unit. No important information is to be mentioned for the following step-17. At step-19, representing the final stage, the cumulative extension account to about 506 m.

6.5. Analysis of faults parameters

The step-by-step analysis during sequential restoration allowed the evaluation of parameters (throw and heave) of all the faults within the section, accounting for the total (cumulative) extension experienced by each section. For each restoration stage (before structural restoration) fault throw and heave were collected and compared with fault parameters from unrestored profiles (Fig. 6.6). As

shown in Fig. 6.6, after the restoration process both CIR-01 and p607 profiles exhibit a flattened trend when compared with the unrestored one, resulting from a significant reduction of the vertical displacement of considered horizons. In CIR-01 the reduction is observed for all the given reference lines (horizons), resulting in a rather flat trend of throw values accounting for about 50 m in average (Fig. 6.6b). A similar throw decrease is observed for p607 except for F1value (up to 250 m) related to the PQ1c unit (Fig 6.6d). Since this value differs much from the other value related to the same fault, it may derive from an error in assessment of throw. In the previous section it has been described as the erosion of S3 horizon (top of PQ1c sub-unit) were not restored due to a paraconformity hiding the actual amount of erosion. This produced an over-estimation of F1 throw relative to PQ1c sub-unit. In order to correct such an error, the erosion restoration of CIR-01 is taken as a reference. In CIR-01, erosion restoration accounted for a throw reduction of roughly a half of the unrestored one (Fig. 6.6a, b). Therefore, the same reduction was applied to F1 in p607 profile as a correction factor (see dashed line in Fig. 6.6d), resulting in a more reliable F1 throw of about 100 m. The revised fault throws were then used for evaluation of vertical rate over the considered time interval (lower Pliocene – present day). In this time span, faults rate is estimated in an average of 0.15 mm/yr (0.18 mm/yr and 0.14 mm/yr respectively for CIR-01 and p607 – Fig. 6.7a and Tab. 6.3a, b) with maximum values at the lower-upper Pliocene transition (up to 0.40 mm/yr and 0.20 mm/yr for CIR-01 and p607 respectively). In the upper Pliocene – Pleistocene interval throw-rates decreased to 0.05 mm/yr and 0.1 mm/yr (CIR-01 and p607, respectively).

Table 6.3a. Comparison between the cumulative parameters of all the fault within the CIR-01 profile (throw, extension and relative rates) and the MESC faults.

Cir-01										
Step	Unit	Cumulative Throw (m)	MESC Throw (m)	% Throw	MESC throw rate (mm/yr)	Cumulative Extension (m)	MESC Extension (m)	% Extension	Total Ext. Rate (mm/yr)	MESC Ext. Rate (mm/yr)
03	PQ2	127.00	123.80	97.48	12.38		104.92			10.49
07 -12	PQ1c	190.89	121.51	63.65	0.05	126.80	83.12	65.55	0.05	0.03
20 - 27	PQ1b	196.80	89.73	45.59	0.09	206.00	63.27	30.71	0.21	0.06
35 - 42	PQ1a	259.38	158.27	61.02	0.40	368.80	122.44	33.20	0.92	0.31
43 - 48	MES	644.62	251.62	39.03	0.19	784.30	258.29	32.93	0.60	0.20

Table 6.3b. Faults parameters and relative rates calculated for the p607 profile

p607					
Step	Unit	MESC Throw (m)	MESC Throwrate (m)	MESC Extension (m)	MESC Ext. Rate (mm/yr)
05	PQ2	148.50	14.85	131.69	13.17
06 - 08	PQ1c	230.52	0.09	202.51	0.08
12 - 13	PQ1b	91.26	0.09	89.86	0.09
15 - 16	PQ1a	73.12	0.18	90.57	0.23
17 - 19	MES	249.90	0.19	195.10	0.15

The CIR-01 profile allowed to discriminate the contribution of MESC faults (F1, F2 and F3) to the overall basin deformation, with respect to the other faults observed within the section. In Fig. 6.7b, MESC throw, and heave (blue and red dashed lines respectively) represent the vertical and horizontal deformation charged to F1, F2 and F2. Conversely, cumulative throw and cumulative heave represent the sum of throw and heave of all the faults within the section (including MESC faults).

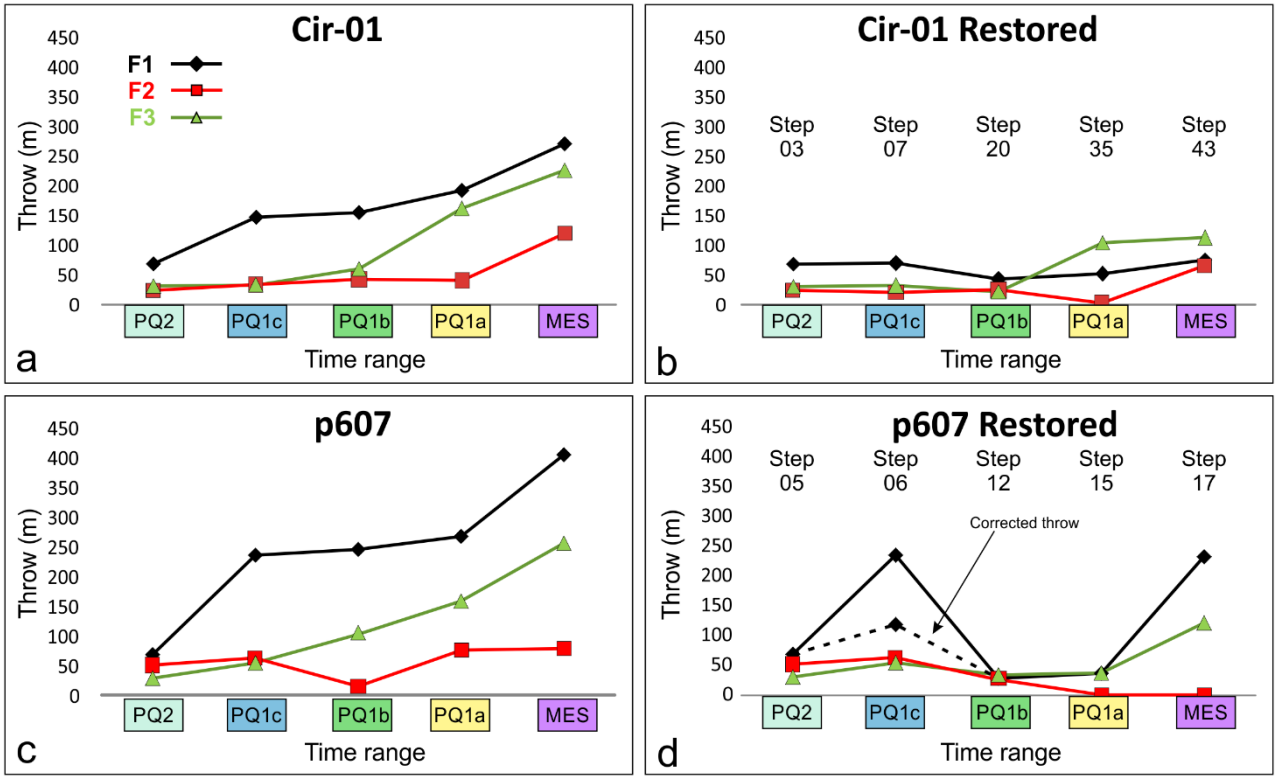

Figure 6.6. Faults throws measured on tectono-stratigraphic models before (a, c) and after (b, d) the application of sequential restoration. References for the given restoration steps are also reported (Gambino et al., 2021b).

At step-48 (undeformed stage), the restored cumulative faults activity (Fig. 6.4 and 6.7b) is measured in ca. 800 m and 640 m, respectively for cumulative extension and throw. At this stage,

MESC faults activity accounted for 258 m of extension and 251 m of throw resulting in a contribution of about 33% and 39% of the total extensional and vertical deformation (Tab. 6.3a). The vertical and horizontal component of cumulative deformation (blue and red solid lines in Fig. 6.7b) decrease toward the present-day setting, converging to trend of MESC faults (blue and red dashed line). This indicates that in the earlier stage (MES-PQ1a transition) the basin deformation was diffuse and distributed over all the faults detected within the section while, approaching the present-day, deformation progressively decrease getting charged almost completely to MESC faults (97.48% of the total deformation, Tab. 6.3a).

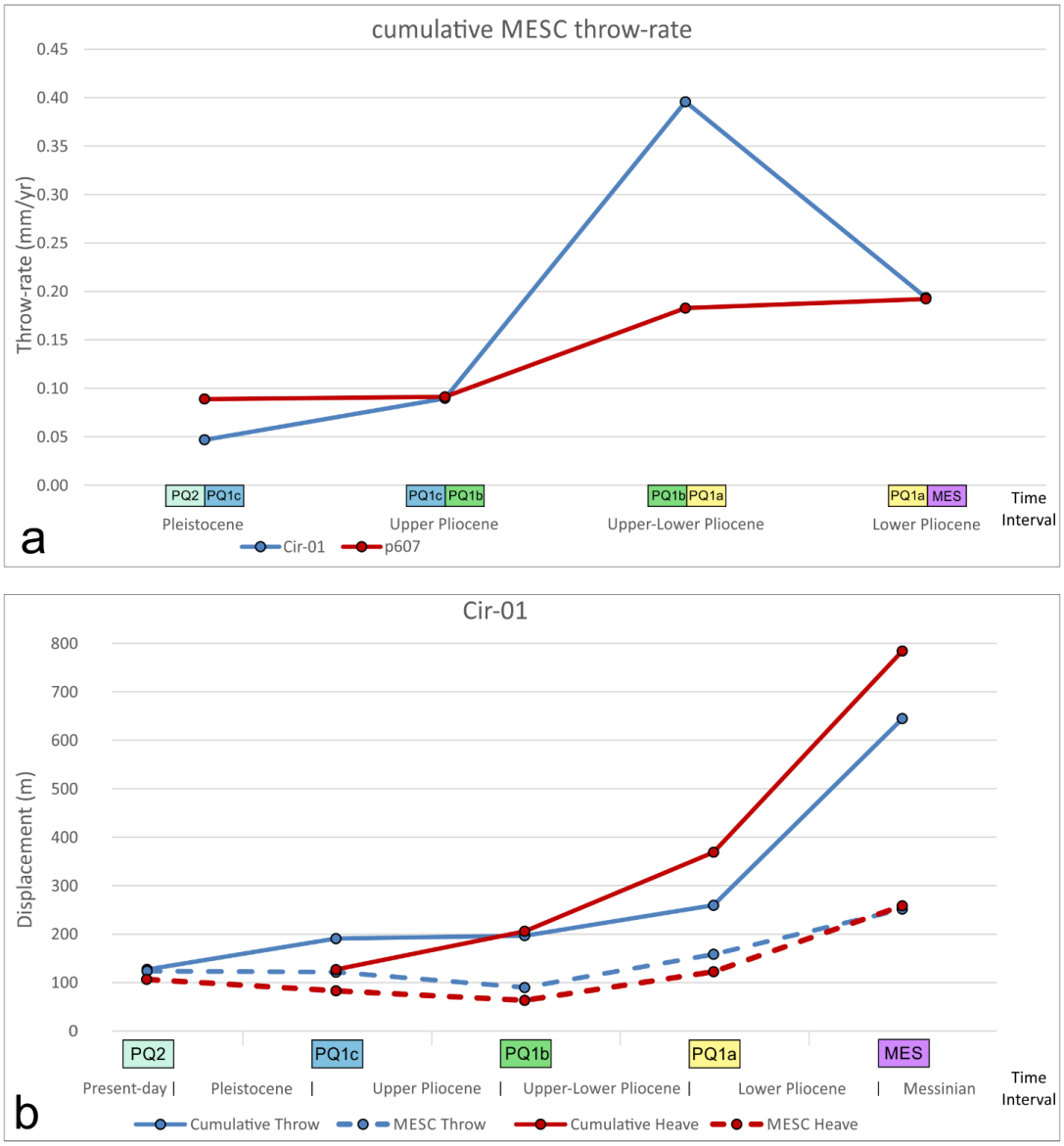

Figure 6.7. (a) MESC faults throw-rate (F1, F2 and F3 faults) relatively to CIR-01 (blue line) and P607 (red line). Value are relative to the time interval between the seismic units reported (inferred ages in Tab. 3.1). b) Displacement components (vertical and horizontal) measured during the restoration of the CIR-01 profile. Dotted lines represent MESC faults parameters (throw and heave,

respectively blue and red) and solid lines represent the cumulative parameters (throw and extension respectively blue and red) of all faults within the seismic model (Gambino et al., 2021b).

6.6. Discussion

The sequential restoration already discussed aims to a better characterization of the tectonic evolution of the studied basin. Recognition and quantification of the erosion affecting the PQ1c unit (S3 top horizon) provided additional information on performing the sequential restoration and on re-calibrating the vertical deformation rate. Reconstruction of the amount of erosion of PQ1c (in CIR-01, see Fig. 6.3a) pointed out to about one third of the original sub-unit is lacking, resulting in a reduction of S3 offset of roughly a half (Fig. 6.6 a, b). Maximum erosion (ca. 70 m deep) has been estimated at the base of F3 (MESC slope base) where the turbidity basin depocenter occurs. Precise erosion estimation was not possible in p607 profile, due to a paraconformity, resulting in an over-estimation (≈250 m) of F1 vertical offset; therefore, erosion of S3 on p607 profile has been estimated with respect to the CIR-01 section (where the throw decreased from 146.20 m to 69.23 m, see Tab. 6.2a and Fig. 6.6b), providing a review of the previously defined F1 throw.

Conversely to F1 and F3, F2 does not show any throw for PQ1a and MES along p607 (Fig. 6.6d) and for PQ1a along CIR-01 (Fig. 6.6b). This evidence suggests that F2 possibly nucleated after sedimentation of PQ1a (lower/upper Pliocene) while F1 and F3 where already active after deposition of MES (Messinian).

According to the inferred ages of seismic units (see section 3.3 and Tab. 3.1) fault rate have been estimated in order to analyse the overtime basin evolution and experienced deformation.

A comparison between the MESC faults parameters and cumulative parameters of all faults (Fig. 6.7b) indicates that deformation was modulated through time. MESC faults activity shows comparable values of both throw and heave for each restoration step (as expected since the fault dip at an average 45° of angle). Instead, cumulative deformation decreased over time from high values of the early stage (800 m and 640 m, respectively extensional and vertical) to the present-day mature

stage (being almost completely represented by the MESC faults activity, Fig. 6.7b). This trend suggests a diffuse (mainly extensional) deformation affecting the basin in the early stage, when MESC faults contributed to 33% and 39% of the cumulative extension and throw respectively. The more deformation continued the more cumulative extensional and vertical components decreased being (at present-day) mostly accommodated (97.48%) by the MESC faults activity (Fig. 6.7b and Tab. 6.3a). In addition, at the early stage of deformation extension was the main component of cumulative deformation (see red solid line) being higher than the cumulative throw. Successively, (from PQ1b onwards) a change occurs with the vertical component being the predominant one. According with this evidence, we infer that two process would be working simultaneously: 1) a purely tectonic process mainly responsible for the MESC faults activity; 2) a mainly extensional process responsible for the diffuse deformation affecting the early stage, which ended its activity during deposition of PQ1c (upper Pliocene). In this view, the second early diffuse deformation observed in Fig. 6.7b can be the result of a ductile level located within (or below) the Messinian unit; in fact, the presence of an underlying detachment layer (frictional or ductile) plays an important role on developing localized or diffuse faulting in the overlying sedimentary cover (Bahroudi et al., 2003). The extensional deformation, produced by the migrating ductile layer underneath, progressively decreased due to thickness reduction of the ductile layer (possibly eastward and/or out of the section) favouring faulting localization of MESC faults.

The final Step-43 and Step-48 (CIR-01, Fig. 6.4), show that the S2 horizon (and related MES unit) stayed strongly bent along Block 4. Taking into consideration the hyaline nature of the lower MES unit and that no extensional fault can explain such a bending, the S2 curvature is likely the result of ductile deformation. Lateral escape of the ductile evaporites, stressed by the sediments vertical load, is therefore invoked to explain the irregular bending of the MES unit. In fact, ductile salt deformation cannot be restored through classical restoration methods (the concept of area conservation is therefore not respected, see section 3) since salt commonly assumes three-dimensional

escape directions and dissolution (Rowan & Ratliff, 2012). In addition, it has been seen how salt migration under sediments load may produce similar effects of local subsidence and uplift (Rojo et al., 2020), explaining, then, the non-horizontal attitude of the S2 horizon.

7. Salt tectonics implication

The hypothesis of a migrating ductile layer inferred by the analysis of basin deformation evolution, may find confirmation in the seismic architecture of the Pliocene deposits and in the deformation pattern of the underlying S2 surface.

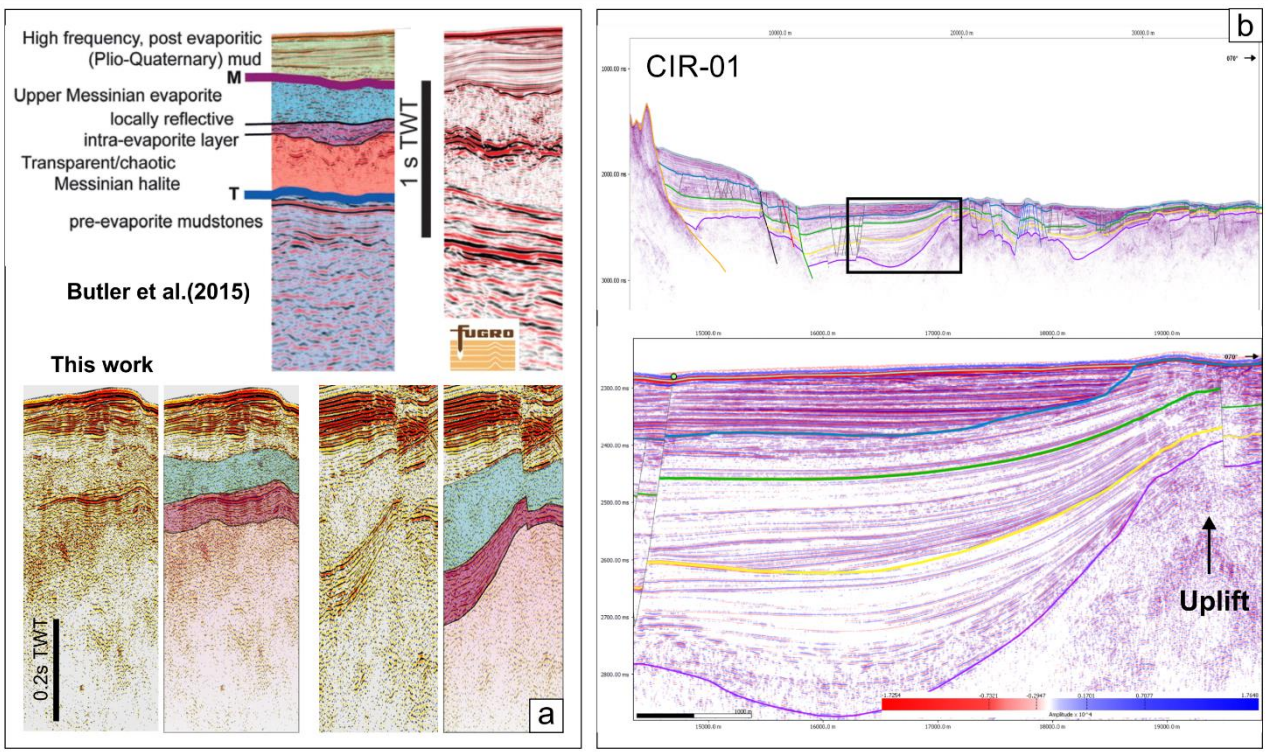

Figure 7.1. a) Comparison of seismic markers of MES unit (Butler et al., 2015, and this study). b) Detail of the internal stratigraphic array within the Pliocene succession. Note the reflectors onlapping on the S3a surface (yellow line) and the subsidence experienced by the central portion of the basin.

Within the CIR-01 profile, the internal stratigraphy of PQ1a and PQ1b units in the turbidite valley shows westward down-lap geometry and layering convergence approaching the uplifted area to the east (Fig. 7.1). This setting suggests two possible evolutions: 1) sediment supply from the east indicating the uplifted area as a possible source for the onlapping sediments or 2) sediment source perpendicular to the section (N-S direction) with syn-uplift sedimentation. Since the characteristics of the turbidite valley basin are consistent with the sediment source mainly from the north, as evidenced by flow erosion and sediment waves (Micallef, 2019; Rebesco et al., 2021), we tend towards the second option. However, the age inferred for the deposits (5-3 Ma, lower to upper

Pliocene) in not consistent with an E-W oriented tectonic compression. Indeed, the thrust front of the Calabrian Accretionary wedge at that time was farther north (Faccenna et al., 2011; Gallais et al., 2013; Barreca et al., 2016), not implying a E-W contraction.

Moreover, the sedimentary units show syncline geometry and thickening (depocenters) localised in the central part of the basin (Fig. 7.1) rather than toward the active fault F3 as expected for growth-strata. Since no compression is observed within the basin, the stratigraphic and geometric setting would suggest a syn-sedimentary subsidence of such units. This internal seismic-stratigraphic pattern of PQ1b (Fig.7b), coupled with the partial hyaline nature of the underlying MES unit and the uplifted area observed further east (uplifted area Fig. 6.2a), could be consistent with salt driven subsidence (and related uplift to east). It is observed that similar structures, known in literature as "expulsion rollovers", are produced by underlying withdrawal of ductile layeyer (salt) on syn-kinematic deposits (Ge et al., 1997; Krézsek et al., 2007; Goteti et al., 2012; Rojo et al., 2020). It is known that salt deposits (in the passive margins) overlie by sediment load would experience lateral spreading/gravity gliding (Ramberg, 1981a; Rey et al., 2001; Platt, 1986; Peel, 2014a) or would give rise to salt withdrawal basins (Brewer& Kenyon, 1996; Peel, 2014b; Rojo et al., 2020). Due to i) its plasticity/ductility, ii) its weaker nature compared to other lithologies and iii) its essential absence of porosity, salt does not undergo compaction but indeed migrates apart. For this reason, salt is generally found to be a detachment layer (Brun & Front, 2011) as observed also for the Calabrian Accretionary Wedge (Polonia et al., 2008, 2011). The correlation between subsidence and related uplift driven by underlying salt migration due to the increasing sediment load has been observed in outcropping area (Lopez-Mir et al., 2014), seismic profiles (Ge et al., 2019) and simulations (Rojo et al., 2020).

Rojo et al. (2020) simulated the evolution of a confined basin with underlying salt layer (model 1, Fig. 7.2). In this model, a sedimentary basin confined between two converging, opposite dipping faults is simulated. The authors show how salt migration (due to sediment load aggrading from the proximal part toward the distal one) may cause withdrawal and expulsion of salt from the proximal

sector towards the distal part of the basin (following the direction of sediment supply), causing salt inflation. Such a salt migration provokes the formation of a rollover syncline in the proximal part of the basin and the formation of a plateau (or elevated area) in the distal one. No diapir occurs in the proximal part but, instead, they occur on the distal bounding fault (see Fig. 7.2). The diapir strike is the same as the bounding distal fault.

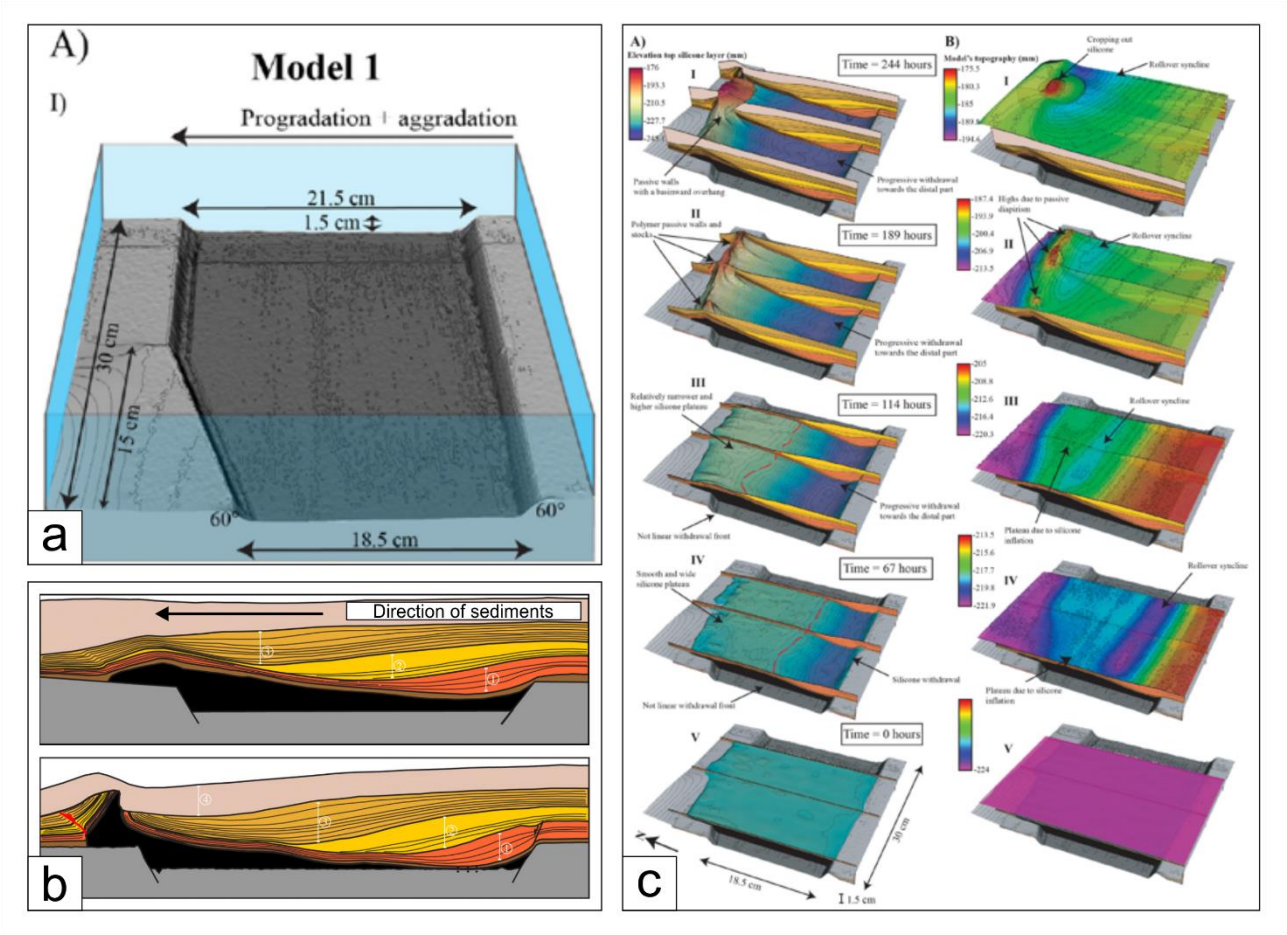

Figure 7.2. Analogue model and simulation by Rojo et al. (2020). a) Model setup; the basin is bounded by two converging faults. b) section views of the final stage. c) Aerial overtime view of the simulation.

This model reflects very well what observed in our seismic data (Fig. 7.3). The sedimentary basin here studied (turbidite valley, fig. 6.1c and 7.3) is confined between two faults systems: the reactivated, proximal MESC (F1, F2 and F3) and the sub-vertical, distal North Alfeo Fault (NAF).

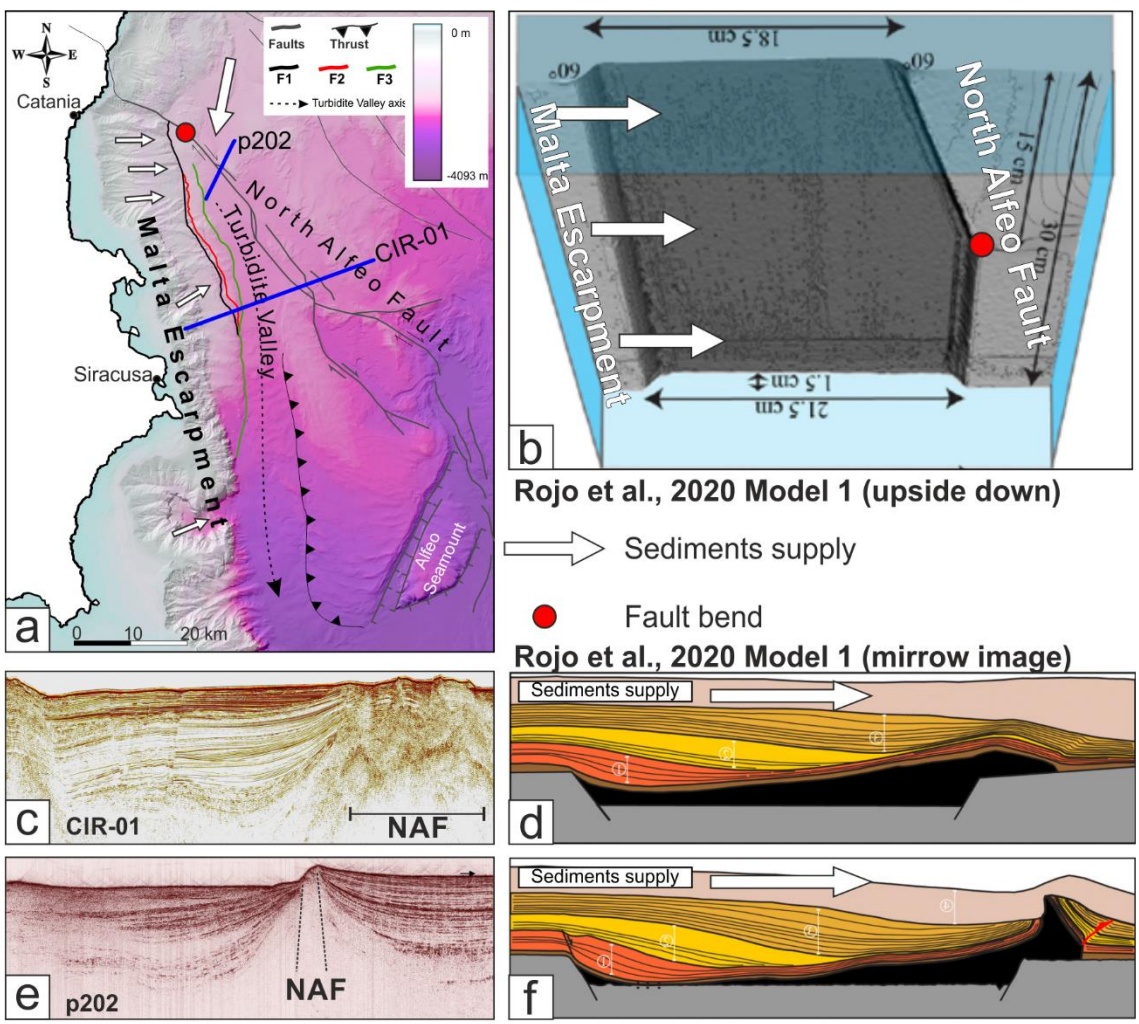

Figure 7.3. Comparison between the deformation observed in the study area and the analogue simulation by Rojo et al (2020). a) Location of the selected seismic profile. b) Rojo et al (2020) model (upside down) reproduces a geometric setting similar to the study area. c) Detail of CIR-01 profile. d) Detail of the simulation showing similarity with c. e) p202 profile showing an uprising diapir. f) Detail of the simulation showing similarity with e. In top-right of Fig.7.2 is reported the position of the diapir (red) adjacent to the distal fault. White arrows indicate the direction of sediments supply.

These two fault systems converge toward the North (see Fig. 7.3a, b) and diapirs are observed along the distal NAF (Fig. 7.3e, f). However, some differences can be found between the model (Rojo et al., 2020) and the actual setting of the studied basin:

1) the basin-bounding faults in the model are considered to be inactive while the MESC and the NAF are active extensional and strike-slip faults, respectively.

2) the distal fault of the model is an inactive, buried fault dipping toward the proximal one, resulting in a graben-like geometry of the basin; conversely, the NAF is an active, subvertical, crustal-

scale, dextral fault system with clear bathymetric expression (Gutscher et al., 2016; Polonia et al., 2016).

3) Lastly, sediments aggradation (in the model) starts from the proximal part of the basin to the distal fault with direction perpendicular to the faults. On the contrary, in our model, sediments are mainly transported from N to S (Rebesco et al., 2021) and subordinately from the MESC slope, as testified by scars and canyons crossing the slope (Micaleff et al., 2019). The twofold sediment source results in an oblique aggradation of sediments on the analysed basin.

It is worth noting that the above hypothesis well explains the irregular and highly bent MES unit, as resulted at the final stage of CIR-01 restoration (step 48 in Fig. 6.4). It is observed, in fact, how the original vertical difference of 595 m measured at the onset of the restoration is reduced to 334 m at the final stages of restoration. This would suggest that the amount of subsidence is consistent with uplift occurred to the east.

Another confirmation of this hypothesis may come from the analysis of the modelled S2 surface, representing the MES top horizon. The contour (Fig. 4.3) highlights a highly deformed S2 horizon characterized by circular depressed and elevated area. The subsided circular areas were attributed to the fault activity (see section 4). In fact, fault activity produces area of increasing accommodation space (where throw is higher) and consequently increasing sediments load, thereby activating salt migration. In this view it is interesting to observe the association of depressed area and uplifted ones located immediately to the SE (Fig. 7.4). The pattern suggests a south-eastwards salt migration, which is in agreement with the resultant direction of sediments supply (as for the model by Rojo et al., 2020).

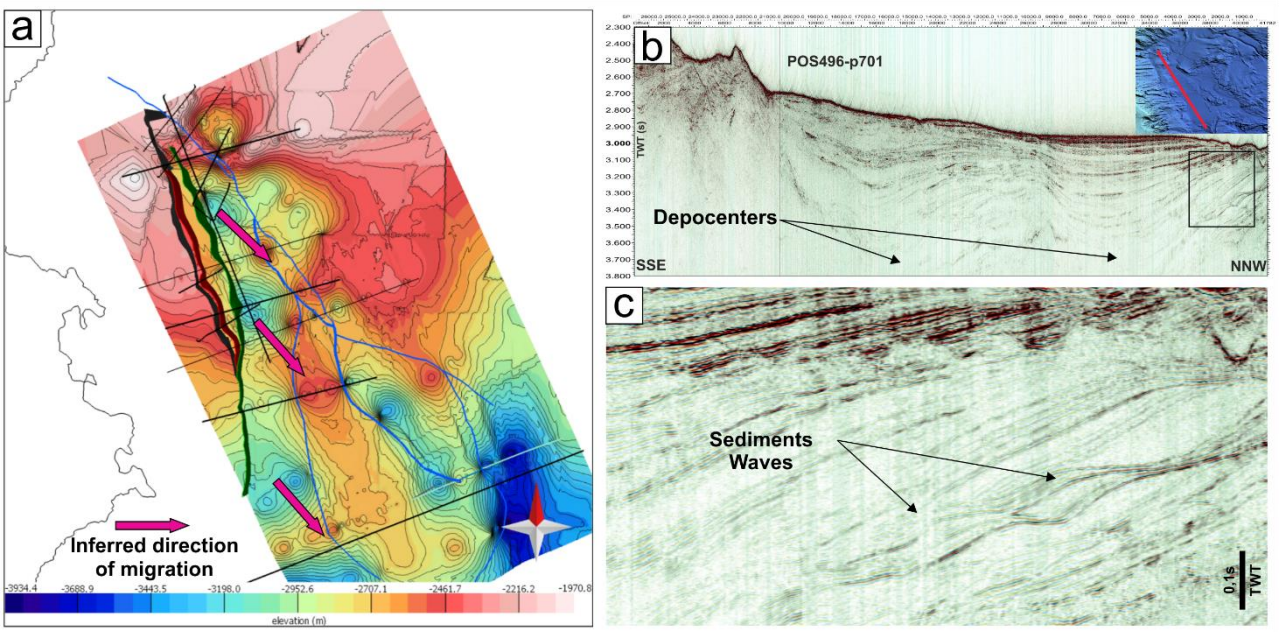

Figure 7.4. a) Colour-shaded S2 surface. Pink arrows indicate the inferred direction of ductile migration. b) p701 profile and detail (c) showing the subsidence experienced due to sediment load and underlying migration of ductile layer (salt?). In c, the presence of sediments waves indicates the direction of sedimentation in agreement with the inferred direction of migration (a).

Anyhow, the sub-horizontal geometry of the PQ2 unit indicates that salt deformation may no longer be active in correspondence of the CIR-01 profile. Evidence of active salt kinematic is, however, still detectable in areas of (high?) extensional deformation, where salt diapirism can be enhanced, as for example, along the NAF realising bends (see p202 profile in Fig. 7.3e).

Such a deformation process involving the Plio-Quaternary sedimentary sequence does not seem to influence, the activity of MESC faults (F1, F2 and F3). In fact, deeper seismic profiles available in literature (Argnani & Bonazzi, 2003, 2005; Polonia et al., 2016; Maesano et al., 2020) show how the abovementioned faults crosscut the Messinian sequence. Conversely, faults generated by the extension related to an underlying salt deformation would have likely been rooted within the salt detachment level. In addition, it has been seen how the interaction between tectonic (MESC fault activity) and sedimentation may be the driving process for salt migration.

8. Possible implication for tsunami triggering

8.1. Introduction

The Western Ionian basin due to its steep margins (Malta Escarpment, Calabrian accretionary wedge, and Apulia Escarpment), its active tectonics and volcanic activity (Mt. Etna and Aegean volcanoes) has been the place of tsunami waves (Papadopoulos and Fokaefs, 2005; Billi et al. 2008, 2010). In southeastern Sicily, historical seismic events have been associated with tsunami waves, among which the most representative are those of 11 January 1693 and 4 February 1169. For both earthquakes (and others) the seismic source as well as the tsunami source (if different) are still under debate.

Recently, Argnani et al. (2012) identified the so called 'Augusta slide' some 20 km offshore the SE Sicily coastline. The landslide deposit covers the (here called) F1 fault segment and represents a very recent mobilisation of the seafloor as it lacks sedimentary cover. However, the 5 km^3 of volume and the 40 km^2 of area estimated (with a single seismic line and very low-resolution bathymetry) by Argnani et al. (2012) for this deposit are definitely poorly constrained and apparently overestimated. The definition of well-constrained volume and vertical drop of a submarine landslide represents, in fact, essential input parameters for possible numerical simulations of tsunamis scenarios and subsequent assessment/management of coastal tsunami risks.

8.2. Methods

Here, a new estimation of the landslide volume is performed on the basis of sub-parallel seismic profiles p605 and MESC08 (Fig. 8.1) that are the high-resolution section of the presented dataset and the Argnani et al. (2012) section, respectively. Then, identification (picking) of the landslide lower surface of rupture and high-resolution bathymetry allowed to better constraining the depth and horizontal spatial extension of the landslide. Bathymetric pseudo-profiles crossing the deposit (sub-parallel and orthogonal to seismic sections) were also used as reference. In order to obtain a realistic

3D model of the volume and relative parameters, the sections were time/depth converted using the velocity model by Gambino et al. (2021a), as reported in section 3. Interpolation of linear features (ordinary Kriging algorithm), picked in seismic and pseudo-profiles (i.e., landslide basal rupture surface), allowed to produce the 2½D surface rupture (Mesh surface). Finally, the landslide volume (TetraVolume) has been created (using MOVE software™, Petex) by the mutual intersection between the lower rupture surface and the high-resolution bathymetry representing the landslide top surface.

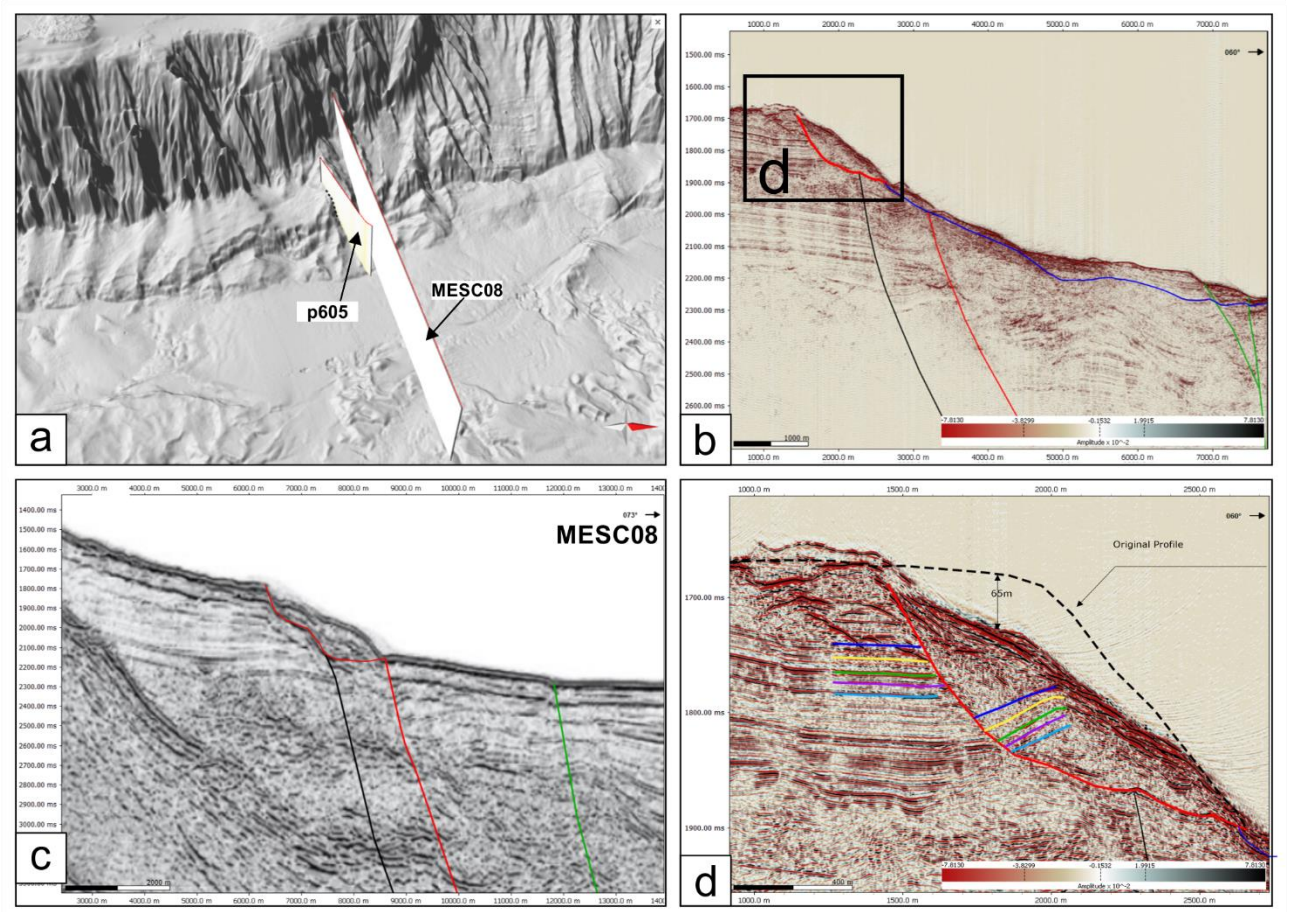

Figure 8.1. a) Seismic profiles p605 and MESC08 (Argnani et al., 2012) crossing the recognised landslide deposits. Interpretation of the landslide basal surface in p605 (b) and MESC08 (c). d) Reconstruction of paleo-bathymetric profile and correlation of the internal stratification.

8.3. Results

From the analysis of the high-resolution p607 profile, two deposits have been defined, deposit 1 and deposit 2, bounded by the red and blue lower surfaces, respectively, in Fig. 8.2. Deposit 1-modelled volume accounted for 0.45 km^3 while the estimated volume of deposit 2 is 0.95 km^3. The covered area is 7.65 km^2 and 21.09 km^2 for deposit 1 and 2, respectively.

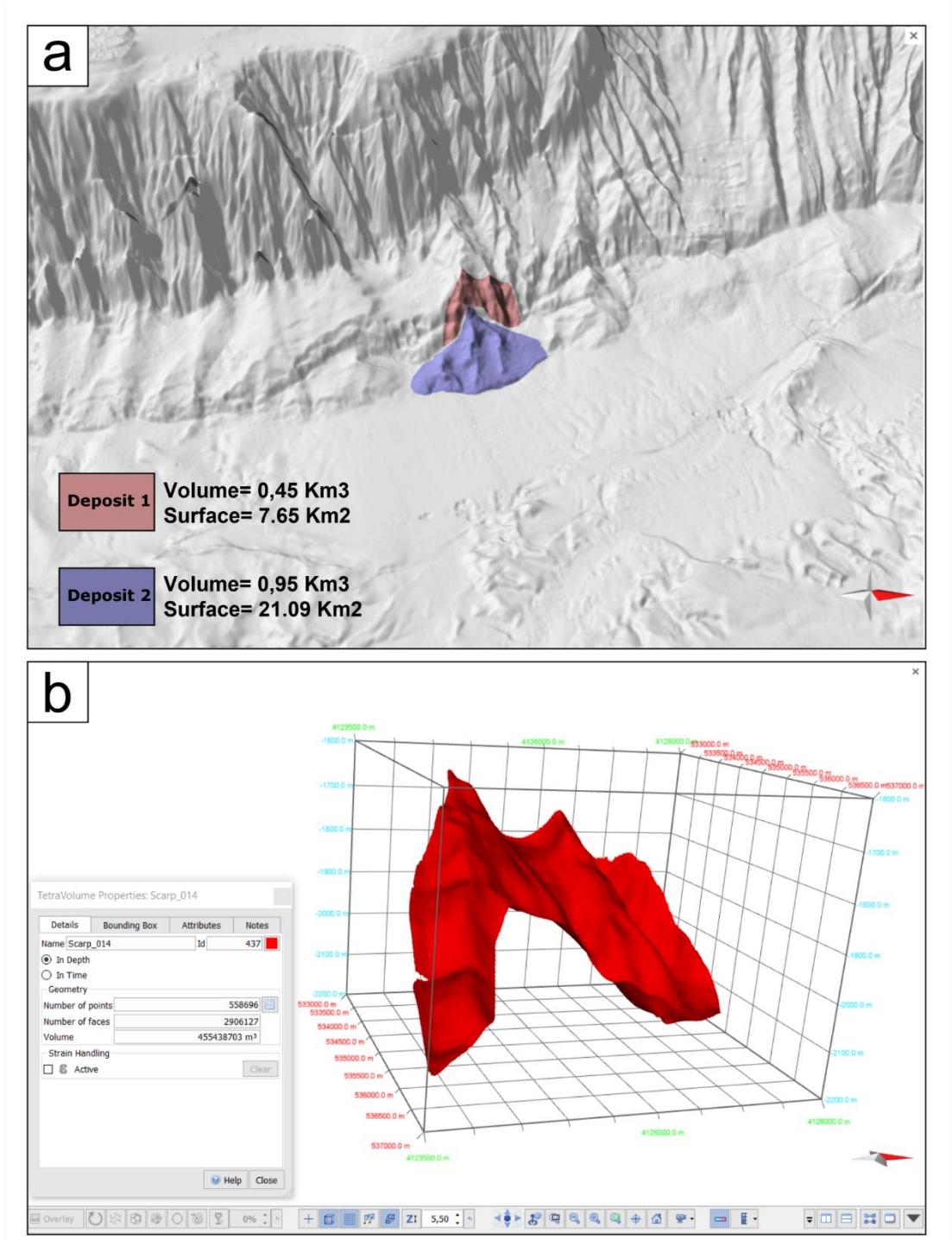

Figure 8.2. a) Perspective 3D view of the recognised deposits and estimation of volumes and covered area. b) 3D model and relative parameters of the deposit 1.

Deposit 2 shows a chaotic seismic character in proximity of the slope base, whereas seismic reflectors are more continuous and sub-parallel away from the slope. This feature suggests that the deposit 2 is likely the result of multiple mass movements. Moreover, deposit 2 is displaced by F3 (green fault) to the east (Fig. 8.1), and at the slope base it is overlaid by sub parallel reflectors

(sedimentation). Both evidences suggest for deposit 2 an age much older than the considered earthquake that would have produce the 1693 tsunami effect. For these reasons, deposit 2 could not be considered as a possible source for this earthquake. Conversely, a chaotic seismic marker on its entire volume characterizes deposit 1, with some slight evidence of its previous stratigraphy (Fig.8.2). Such chaotic facies disturb the high-frequency, continuous, parallel and high-amplitude seismic layering characterising the internal seismic feature of the undeformed slope. In addition, deposit 1 sutures F1 (black fault in Fig. 8.1) which is described as an active, high-rate fault (Bianca et al., 1999; Argnani et al., 2005, 2012; Gambino et al., 2021a, see section 3) as it shows an evident bathymetric expression to the north and south of the deposit 1. In addition, any recent sediments are observed covering the deposit 1, suggesting that it must be a very recent bathymetric feature.

Correlation with the original stratigraphy (to the left of the landslide) was inferred for the internal portion of the deposit 1 (Fig. 8.2) indicating about 60m of vertical offset. Reconstruction of inferred palaeo-bathymetric profile indicate a vertical drop of 65m, which is in agreement with the stratigraphic assessment of the offset. The assessment of volume of deposit 1 and the estimation of landslide vertical drop suggest a possible role played by this landslide in triggering of the 1693 tsunami wave and represent important parameters for numerical simulation of the tsunami effect due to sub-marine gravimetric mass movement.

9. Discussion

Collected data, including high-resolution seismic reflection profiles and bathymetry, field data as well as $2^1/_2$D modelling, allowed to achieve further information on Pliocene-Quaternary deformation pattern and tectonic evolution of the northern sector of the Malta Escarpment and related proximal basin. Here, the high-resolution seismic data allowed a better characterization of some tectonic structures previously mapped by other authors (Hirn et al., 1997; Bianca et al., 1999; Argnani and Bonazzi, 2002, 2005; Argnani et al., 2012; Polonia et al., 2012; Gutscher et al., 2016, Maesano et al., 2020), providing further constraints of their spatial dimension and new insight on tectonic evolution.

The data show how the Ionian offshore of southeastern Sicily is deformed by a N-S oriented, E-dipping fault system, consisting of three main segments (F1, F2 and F3). The low-penetration of seismic profiles does not permit to visualize the relation of faults with depth, whether they represents the shallower splay of a single crustal structure or not. However, the bathymetric expression shows faults convergence toward the F3, which is considered the main structure.

Analysis of seismic stratigraphy allowed defining four main seismic units (Pre-MES, MES, PQ1 and PQ2) based on their seismic facies, the bounding discontinuities and the geometrical relation of internal reflectors. Within the seismic units, chaotic wedge-shaped bodies thickening toward the F3 fault indicate fault-triggered gravitational mass movement, testifying the Pliocene-Quaternary fault activity (Fig. 3.2c).

Fault rate estimation pointed out to a low deformation rate for the given area, whose value was modulated through time. Fault pattern analysis provided information on the faults growing style, revealing that each fault plane nucleated discontinuously in two segments rather than in a single radial way (Fig. 3.7a-c- see Cartwrigth et al., 1995 for description). Successively, segment linkage has given rise to the three single-fault observed (F1, F2 and F3). The incipient segmentation is less visible in

the major F3 fault. The increasing fault dip to the west (36°, 46° and 49° respectively for F1, F2 and F3, see Tab. 4.1), would suggest a rotational, domino-style, simple-shear, deformation but this geometrical configuration also fits with fault converging to a deeper single structure. The latter model seems likely to be confirmed by the simultaneous activity highlighted by offset analysis (see section 3.6 and Fig. 3.7), convergence of fault bathymetric expressions, and by deeper seismic lines available from literature (Argnani and Bonazzi, 2003, 2005; Polonia et al., 2017). Since our low-penetrating seismic data do not resolve the deeper geometry of the MESC faults, they have been independently processed for 3D modelling and stress analysis.

Instrumental and historical earthquakes occurred in the study area (see section 1.4) point to a high seismogenic stress localized along the Sicily Ionian coastal sector, but the actual source of the most devasting earthquakes (1169 and 1693 earthquakes, with M>7.0) is still elusive. Empirical scaling relation (Wells and Coppersmith, 1994; Leonard, 2010) suggest the given faults to be capable of generating earthquakes with magnitude exceeding 7.0. Moreover, the Slip Tendency analysis, performed by applying field-derived stress tensor, indicate the F3 fault as the only one geometrically well oriented for reactivation along its entire length (with an estimated magnitude up to 7.17). Scaling relations also revealed that a so high-energy seismic event is compatible with surface displacements of about 3m (maximum displacement, MD) and 1.2m (average displacement, AD). Based on the MD and the AD, it was possible to estimate the recurrent time for M≈7 earthquakes potentially generated by the F3 fault. Assuming that the F3 seafloor scarp (66 m and 29 m respectively for maximum value and mean value) is the result of the cumulative slip produced by M≈7 earthquakes, a number (integer) of 22 (considering the maximum scarp divided by the MD) or 25 (considering the mean scarp divided by the AD) events is obtained. Considering the age of 11.700 years assumed for the seafloor, return periods of 470 and 537 years can be calculated. Even though the seafloor age is poorly constrained do to the lack of core/well data, the estimation of these return periods is comparable with those proposed by other authors for the same earthquake (475 years for events with intensity IX-X, Barbano

et al., 2001, and 644 years for events with intensity X, Bianca et al., 1999). Maximum expected magnitude and recurrent time are, in addition, in good agreement with those estimated for large historical events in the study area (Barbano, 1985; Boschi et al., 1995b; Rovida et al., 2016), suggesting F3 as a potential candidate for the considered earthquakes (1169, 1693). The presence of an offshore source could be further supported by the macroseismic intensity field for the 1693 (Barbano et al., 1985), showing isolines opening toward the sea; anyhow, a possible on shore, NE-SW oriented, source consistent with the Monterosso-Agnone fault system (see Fig.1.6, section 1.3.1), even if unlikely, cannot be ruled out.

Sequential restoration analysis allowed a better characterization of tectonic rates and provided an insight into the deformation experienced overtime by the Pliocene-Quaternary basin (turbidite valley in Fig. 6.1 and 6.2). Identification and reconstruction of the S3 erosive truncation gave the opportunity to estimate the amount of erosion affecting the seismic units and re-calibrate fault offsets accordingly. The reconstruction of the S3 geometry has suggested that the amount of erosion is higher at the slope base and gradually decrease up-slope in agreement with what expected for the turbidite nature of the basin down-slope. Moreover, reconstructed erosion indicates that about one third of the original PQ1c thickness was erased; this resulted in an offset reduction of about one half for the F1, with additional impact on decompaction of lower units. Similarly, a correction was adopted for the p607 profile, where the erosive surface is not visible due to a paraconformity between the seismic units.

The sequential restoration aimed to a revision of the previously measured offsets (on unrestored sections) and related faulting rates. A general throw decrease is observed for all the faults, which show an offset of about 50 m in average for all the considered restoration stages (Fig. 6.6 a, b). In particular, restored throw pointed out to a possible inception of the F2 fault activity after the deposition of PQa (upper-lower Pliocene transition) when F1 and F3 were already active. This is in line with the inferred secondary role of the F2 with respect to the F1 and the F3. Moreover, the

evidence (CIR-01 profile) of a null offset relatively to the younger S3a horizon (PQ1a top surface) coupled with the displacement of the older S2 horizon (MES top horizon, see Fig. 6b) would indicate that the F2 likely reactivated above an older fault affecting the MES unit.

The step-by-step analysis permitted to calculate the fault-rates for each stage of deformation and to discriminate the amount of deformation charged by the MESC faults with respect to the other faults within the analyzed section. In general, the basin has experienced a low-deformation (0.15 mm/yr in average) since the Messinian-Pliocene boundary. Deformation rate was slightly higher at the initial phase (0.18 mm/yr and 0.4 mm/yr, respectively, for p607 and CIR-01 sections) and slowly decreased (0.09 mm/yr and 0.05, respectively, for p607 and CIR-01) during the Pleistocene. Still elusive is the rate during the Holocene. The poorly constrained high rate (3 to 7 mm/yr) observed on a unrestored section could not be solved by sequential restoration since the actual age of the PQ2 unit remains inferred. Moreover, the analysis of horizontal and vertical displacements revealed how the MESC faults maintained a relatively flat offset trend (resulting in an average rate of 0.15 mm/yr) showing comparable values for all restoration stages (Fig. 6.7b). The overlap of vertical and extensional values shown for the MESC faults is in line with the average 45° dip of the faults. Conversely, the cumulative deformation (extension and throw components) was modulated through time, showing higher values during the Messinian-Pliocene transition and a decrease over time until it almost disappeared in Pleistocene times. This pattern has been interpreted as the result of an early-stage diffuse deformation probably controlled by all the faults within the basin. At this stage the MESC faults contributed to about 39% of the cumulative throw and about 33% of the cumulative extension. The subsequent deformation stage has shown a constant decrease of the cumulative deformation (not observed for the MESC faults) which, approaching the present day, is almost entirely (97.48% of throw and 100% of extension) taken over by the MESC faults. A more detailed observation of cumulative deformation highlights how, in the early stage, the extensional cumulative

deformation prevailed over the vertical one, but inverting the relation after the upper Pliocene (Fig. 6.7b) with the vertical component becoming higher than the horizontal.

This evidence, along with further observations, such as **1)** the internal geometry of reflectors within the PQ1 sub-units (Fig. 7.1b and 7.3, see section 7), **2)** the analysis of the modelled S3 surface (Fig. 4.3 and 7.4, see section 7), **3)** the horizontal (undeformed) reflector of PQ2 unit (Fig. 4.2d, 4.3a and 7.4 section 3.2), and **4)** the analysis of the curved MES unit at the final stage of the sequential restoration (step 48 in Fig. 6.4) allowed as to infer that another deformation process, characterized by major horizontal extension, was active simultaneously with the MESC faults during the early deformation stage. This process is likely related to the diffuse extensional deformation occurred during the early stage. A possible explanation should be given by ductile deformation underlying the top horizon of the MES (S2). Considering the partial hyaline nature of the MES unit, such a ductile deformation should be attributed to the presence of migrated salt layer. In fact, it has been seen by analogue simulations how the presence of an underlying level of ductile detachment favors the development of diffuse deformation on the overlying sediments (Bahroudi et al., 2003), which results in diffuse faulting. Conversely, the presence of a frictional detachment level promotes the development of localized faulting. In this view, the early deformation stage could have been driven by the horizontal migration of Messinian salt. Successively, due to the gradually thickness reduction of the salt layer, faulting localized on MESC faults.

The hypothesis of salt tectonics is further supported by the internal seismic stratigraphy of the PQ1 unit. The reflector array is consistent with subsidence and depocenters migration on sediments overlying migrating salt layer (due to sediment load), as observed in analogue simulations (Rojo et al., 2020). Simulations highlight how the local subsidence is always accompanied by uplift and possibly by diapirism toward the direction of sediments supply. The modelled S2 surface (see Fig. 7.4 and section 7) suggests that migration occurred toward the SE, which represents the same (cumulative) direction of sediments filling the basin. The strongly folded MES unit, observed at the

final stages of restoration of the CIR-01 section apparently confirms the ductile deformation experienced by the unit.

The inferred salt tectonics diffusely experienced by the basin should have ended in the upper Pliocene. This is deduced by the changing in deformation style from mainly extensional to mainly vertical occurred (see Fig. 6.7b) in the lower/upper Pliocene transition and by the diffused extension ended after the deposition of the PQ1 (upper Pliocene). This is further supported by the horizontal geometry of reflectors in the upper PQ2 unit, which does not show any internal deformation, unlike the PQ1 unit.

The analysed seismic profiles also highlighted the presence of a recent landslide, previously mapped by Argnani et al. (2012). This represents a key point for further studies on earthquake-triggered landslides and subsequent generation of tsunami waves. Interpolation of two seismic lines coupled with the analysis of high-resolution bathymetry led to the estimation of the 3D volume of the landslide deposits with a much higher precision than previously reported. Landslide parameters derived from the 3D reconstruction (volume, areal extent, vertical drop, etc.) will be useful for further simulations of tsunami triggering and related coastal effects.

10. Conclusions

New offshore seismic data and numerical approach allowed to achieve further information on the structural setting, seismotectonics and seismic potential of the seismically active Malta Escarpment and the Ionian coastal sector of Sicily.

Primary findings previously discussed are here briefly summarized:

- the norther sector of the Malta Escarpment and adjacent basin is deformed by a fault system (three main segments likely converging at depth), roughly N-S trending, in response of a regional stress field with maximum extension oriented ENE to E;
- high rate of active deformation is testified by clear expressions at the seafloor (fault scarps and triangular facets), in an area with a relatively high sedimentation rate. The actual present-day rate is still elusive due to the lack of clear datation of the shallower sub-seafloor;
- empirical scaling relations applied on 3D model-derived fault dimensions (in particular for the F3 main fault) pointed out a maximum expected magnitude and recurrent time in line with those estimated for large historical seismic events in the area (1169 and 1693 earthquakes);
- a possible source located further east on the 80 km-long NAF cannot be ruled out, even though its inferred almost pure strike-slip kinematic would not explain the tsunami effects associated with seismic events;
- sequential restoration of modelled seismic section provided a re-calibration of previously achieved fault displacements and rates; results point to a throw rate, modulated and decreasing through time, ranging from 0.09-0.4 mm/yr in the Pliocene to 0.05-0.09 mm/yr in the Pleistocene; extensional rates are, instead, estimated at 0.06-0.31 mm/yr for the Pliocene and 0.03-0.08 mm/yr for the Pleistocene;

- analysis of the MESC deformation components with respect to the cumulative ones revealed a diffuse mainly extensional deformation affecting the basin during the early deformation (lower Pliocene).

References

Accaino F., Catalano R., Di Marzo L., Giustiniani M., Tinivella U., Nicolich R., Sulli A., Valenti V. & Manetti P. (2011). A crustal seismic profile across Sicily. Tectonophysics, 508, 52-61.

Adam, J., Reuther, C. D., Grasso, M., & Torelli, L. (2000). Active fault kinematics and crustal stresses along the Ionian margin of southeastern Sicily. Tectonophysics, 326(3-4), 217-239.

Allmendinger, R. W., Cardozo, N., & Fisher, D. M. (2011). Structural geology algorithms: Vectors and tensors. Cambridge University Press, 1-289. https://doi.org/10.1017/CBO9780511920202

Amato, A., Azzara, R., Basili, A., Chiarabba, C., Cocco, M., Di Bona, M., & Selvaggi, G. (1995). Main shock and aftershocks of the December 13, 1990, Eastern Sicily earthquake. Annals of Geophysics, 38(2).

Angelier, J. (1984). Tectonic analysis of fault slip data sets. Journal of Geophysical Research: Solid Earth, 89(B7), 5835-5848.

Argnani, A. (1990). The strait of Sicily rift zone: Foreland deformation related to the evolution of a back-arc basin. Journal of Geodynamics, 12(2-4), 311-331. doi:10.1016/0264-3707(90)90028-S

Argnani, A. (1993). Neogene basins in the strait of Sicily (central Mediterranean): Tectonic settings and geodynamic implications. Recent Evolution and Seismicity of the Mediterranean Region, , 173-187. doi:10.1007/978-94-011-2016-6_8

Argnani, A. (2000). The southern tyrrhenian subduction system: Recent evolution and neotectonic implications. Annali Di Geofisica, 43(3), 585-607.

Argnani, A. (2009). Evolution of the southern tyrrhenian slab tear and active tectonics along the western edge of the tyrrhenian subducted slab doi:10.1144/SP311.7

Argnani, A., and Bonazzi, C. (2002). Tectonics of eastern Sicily offshore: preliminary results from the MESC 2001 marine seismic cruise. Boll. Geofis. Teor. Appl. 43 (3–4), 177–193.

Argnani, A., & Bonazzi, C. (2005). Malta Escarpment fault zone offshore eastern Sicily: Pliocene-Quaternary tectonic evolution based on new multichannel seismic data. Tectonics 24, TC4009. doi:10.1029/2004TC001656

Argnani, A., & Savelli, C. (1999). Cenozoic volcanism and tectonics in the southern tyrrhenian sea: Space-time distribution and geodynamic significance. Journal of Geodynamics, 27(4-5), 409-432. doi:10.1016/S0264-3707(98)00025-8

Argnani, A., Armigliato, A., Pagnoni, G., Zaniboni, F., Tinti, S., & Bonazzi, C. (2012). Active tectonics along the submarine slope of south-eastern Sicily and the source of the 11 january 1693 earthquake and tsunami. Natural Hazards and Earth System Science, 12(5), 1311-1319. doi:10.5194/nhess-12-1311-2012

Azzaro, R., and M.S. Barbano (2000). Analysis of seismicity of Southeastern Sicily: a proposed tectonic interpretation. Ann. Geofis. 43, 171-188.

Azzaro, R., Barbano, M. S., Moroni, A., Mucciarelli, M., & Stucchi, M. (1999). The seismic history of Catania. Journal of Seismology, 3(3), 235-252.

Bai, T., Maerten, L., Gross, M. R., & Aydin, A. (2002). Orthogonal cross joints: do they imply a regional stress rotation? J. Struct. Geol. 24, 77–88. doi:10.1016/S0191-8141(01)00050-5

Bai, T., & Pollard, D. D. (2000). Fracture spacing in layered rocks: a new explanation based on the stress transition. J. Struct. Geol. 22, 43–57. doi:10.1016/S0191-8141(99)00137-6

Bally, A. W., Gordy, P. L., & Stewart, G. A. (1966). Structure, seismic data, and orogenic evolution of southern Canadian Rocky Mountains. Bulletin of Canadian Petroleum Geology, 14, 337–381.

Baratta, M. (1901). I terremoti d'Italia: saggio di storia, geografia e bibliografia sismica italiana (No. 9). Fratelli Bocca.

Barbano, M. S. (1985). The val di Noto earthquake of January 11, 1693. In: Atlas of isoseismal maps of Italian earthquakes, CNR-PFG, quad Bologna: Consiglio nazionale delle ricerche, Vol. 2A, 48–49.

Barbano, M. S., & Cosentino, M. (1981). Il terremoto siciliano dell'11 Gennaio 1693. Rendiconti della Società geologica italiana, 4(5), 517-522.

Barbano, M. S., Rigano, R., Cosentino, M., & Lombardo, G. (2001). Seismic history and hazard in some localities of south-eastern Sicily. Bollettino Di Geofisica Teorica Ed Applicata, 42(1-2), 107-120.

Barberi, F., P. Gasparini, F. Innocenti, and L. Villari (1973). Volcanism of the southern Tyrrhenian Sea and its geodynamics implications. J. Geophys. Res., 78(23), 5221–5232, doi:10.1029/JB078i023p05221.

Barca, D., Cirrincione, R., De Vuono, E., Fiannacca, P., Ietto, F., & Lo Guidice, A. (2010). The triassic rift system in the northern calabrian-peloritani orogen: Evidence from basaltic dyke magmatism in the san donato unit. Periodico Di Mineralogia, 79(2), 61-72. doi:10.2451/2010PM0010

Bahroudi, A., Koyi, H. A., & Talbot, C. J. (2003). Effect of ductile and frictional décollements on style of extension. Journal of Structural Geology, 25, 1401–1423. https://doi.org/10.1016/S0191-141(02)00201 -8

Barreca, G. (2014). Geological and geophysical evidences for mud diapirism in south-eastern Sicily (Italy) and geodynamic implications. J. Geodyn. 82, 168–177. doi:10.1016/j.jog.2014.02.003

Barreca, G., & Monaco, C. (2013). Vertical-axis rotations in the sicilian fold and thrust belt:New structural constraints from the madonie mts. (Sicily, Italy). Italian Journal of Geosciences, 132(3), 407-421. doi:10.3301/IJG.2012.44

Barreca, G., Corradino, M., Monaco, C., & Pepe, F. (2018). Active tectonics along the south east offshore margin of mt. etna: New insights from high-resolution seismic profiles. Geosciences (Switzerland), 8(2) doi:10.3390/geosciences8020062

Barreca, G., Gross, F., Scarfì, L., Aloisi, M., Monaco, C., & Krastel, S. (2021). The strait of messina: Seismotectonics and the source of the 1908 earthquake. Earth-Science Reviews, 218 doi:10.1016/j.earscirev.2021.103685

Barreca, G., Scarfì, L., Cannavò, F., Koulakov, I., & Monaco, C. (2016). New structural and seismological evidence and interpretation of a lithospheric-scale shear zone at the southern edge of the Ionian subduction system (central-eastern Sicily, Italy). Tectonics, 35(6), 1489-1505.

Barreca, G., Scarfì, L., Gross, F., Monaco, C., & De Guidi, G. (2019). Fault pattern and seismotectonic potential at the south-western edge of the Ionian subduction system (southern Italy): New field and geophysical constraints. Tectonophysics, 761, 31-45. doi:10.1016/j.tecto.2019.04.020

Beccaluva, L., Colantoni, P., Savelli, C., & Di Girolamo, P. (1981). Upper-miocene submarine volcanism in the strait of sicily (banco senza nome). Bulletin Volcanologique, 44(3), 573-581. doi:10.1007/BF02600587

Beccaluva, L., Macciotta, G., Morbidelli, L., Serri, G., and Traversa, G. (1989). Cainozoic tectono-magmatic evolution and inferred mantle sources in the Sardo-Tyrrhenian area. In: Boriani, A., Bonafede, M., Piccardo, G. B., and Vai, G. B., Editors. Atti Convegni Lincei, 80, 229-248.

Behncke, B. (1998), Il vulcanesimo del Plateau Ibleo (Sicilia sud-orientale) negli ultimi 230 Ma, Boll. Accad. Gioenia Sci. Nat. Catania, 31(355), 39– 50.

Behncke, B. (2001). Volcanism in the Southern Apennines and Sicily. In: Vai, G.B., and Martini I.P., eds., Anatomy of an Orogen. The Apennines and adjacent Mediterranean basins: Amsterdam, Kluwer, 105–120.

Ben-Avraham, Z., Boccaletti, M., Cello, G., Grasso, M., Lentini, F., Torelli, L., & Tortorici, L. (1990). Principali domini strutturali originatisi dalla collisione nogenico–quaternaria nel Mediterraneo centrale. Memorie della Società Geologica Italiana, 45, 453–462.

Bianca, M., Monaco, C., Tortorici, L., and Cernobori, L., (1999). Quaternary normal faulting in southeastern Sicily (Italy): A seismic source for the 1693 large earthquake: Geophysical Journal International, v. 139, no. 2, p. 370–394, doi:10.1046/j.1365-246x.1999.00942.x.

Bianchi, F., Carbone, S., Grasso, M., Invernizzi, G., Lentini, F., Longaretti, G., Merlini, S., & Mostardini, F. (1987). Sicilia orientale: Profilo geologico Nebrodi-Iblei. Memorie della Società Geologica Italiana, 38, 429–458.

Bianchi, I., Lucente, F. P., Di Bona, M., Govoni, A., & Piana Agostinetti, N. (2016). Crustal structure and deformation across a mature slab tear zone: The case of southern Tyrrhenian subduction (Italy). Geophysical Research Letters, 43(24), 12,380-12,388. doi:10.1002/2016GL070978

Billi, A., & Salvini, F. (2001). Fault-related solution cleavage in exposed carbonate reservoirs rocks in the southern Apennines, Italy. Journal of Petroleum Geology, 24(2), 147-169. doi:10.1111/j.1747-5457.2001.tb00665.x

Billi, A., Barberi, G., Faccenna, C., Neri, G., Pepe, F., & Sulli, A. (2006a). Tectonics and seismicity of the Tindari fault system, southern Italy: Crustal deformations at the transition between ongoing contractional and extensional domains located above the edge of a subducting slab. Tectonics, 25(2) doi:10.1029/2004TC001763

Billi, A., Cuffaro, M., Beranzoli, L., Bigi, S., Bosman, A., Caruso, C., ... & Tartarello, M. C. (2020). The SEISMOFAULTS Project: First surveys and preliminary results for the Ionian Sea area, southern Italy. Annals of Geophysics.

Billi, A., Funiciello, R., Minelli, L., Faccenna, C., Neri, G., Orecchio, B., & Presti, D. (2008). On the cause of the 1908 Messina tsunami, southern Italy. Geophysical Research Letters, 35(6).

Billi, A., Minelli, L., Orecchio, B., & Presti, D. (2010). Constraints to the cause of three historical tsunamis (1908, 1783, and 1693) in the Messina Straits region, Sicily, southern Italy. Seismological Research Letters, 81(6), 907-915.

Billi, A., Porreca, M., Faccenna, C., & Mattei, M. (2006b). Magnetic and structural constraints for the non-cylindrical evolution of a continental forebulge (Hyblea, Italy). [Evoluzione non-cilindrica del rialzo periferico dell'avampaese Ibleo (Sicilia) da dati magnetici e strutturali] Rendiconti Della Societa Geologica Italiana, 2, 82.

Bingham, C. (1974). An antipodally symmetric distribution on the sphere. Ann. Stat. 2 (6), 1201–1225.

Boccaletti, M., Cello, G., Lentini, F., Nicolich, R., & Tortorici, L. (1989). Structural evolution of the Pelagian Block and Eastern Tunisia. In: Boriani, A., et al., eds., The lithosphere in Italy: Accademia Nazionale dei Lincei. pp. 129–138.

Boccaletti, M., Cello, G., & Tortorici, L. (1987). Transtensional tectonics in the Sicily Channel. Journal of Structural Geology, 9(7), 869-876.

Boccaletti, M., Cello, G., & Tortorici, L. (1990). Strike-slip deformation as a fundamental process during the Neogene-Quaternary evolution of the Tunisian-Pelagian area. Ann. Tecton., 4, 104–119.

Boccaletti, M., Nicolich, R., & Tortorici, L. (1984). The Calabrian arc and the Ionian sea in the dynamic evolution of the central Mediterranean. Marine Geology, 55(3-4), 219-222,IN1-IN8,223-245. doi:10.1016/0025-3227(84)90070-7

Boccone, P., (1697). Intorno il terremoto della Sicilia seguito l'anno 1693. Museo di fisica e di esperienze variate e decorato di osservazioni naturali, note medicinali e ragionamenti secondo i principi moderni, Venezia.

Bonforte, A., Guglielmino, F., Coltelli, M., Ferretti, A., & Puglisi, G. (2011). Structural assessment of mount etna volcano from permanent scatterers analysis. Geochemistry, Geophysics, Geosystems, 12(2) doi:10.1029/2010GC003213

Boschi E., Guidoboni E., (2001). Catania terremoti e lave dal mondo antico alla fine del Novecento. INGV-SGA, Bologna, 414 pp.

Boschi, E., Guidoboni, E. and Mariotti, D., (1995a), Seismic effects of the strongest historical earthquakes in the Syracuse area, Annali di Geofisica 38 (2) (May), 223–253.

Boschi, E., Ferrari, G., Gasperini, P., Guidoboni, E., Smriglio, G. and Valensise, G., (1995b). Catalogo dei forti terremoti in Italia dal 461 a.C. al 1980, ING-SGA, Ozzano Emilia

Boschi, E., Guidoboni, E., Ferrari, G., Mariotti, D., Valensise, G., & Gasperini, P. (2000). Catalogue of Strong Italian Earthquakes from 461 BC to 1997 (Appendix to volume 43 N° 4, 2000). Annals of Geophysics, 43(4).

Bott, M. H. P. (1959). The mechanics of oblique slip faulting. Geol. Mag. 96, 109–117

Bousquet, J. C., & Lanzafame, G. (2004). Compression and Quaternary tectonic inversion on the Northern edge of the Hyblean Mountains, foreland of the Appenine-Maghrebian chain in Eastern Sicily (Italy): geodynamic implications for Mt. Etna. GeoActa, 3(2004), 165-177.

Boyer, S. E., & Elliot, D. (1982). Thrust systems. American Association of Petroleum Geologists Bulletin, 66, 1196e1230.

Branca, S., Coltelli, M., De Beni, E. & Wijbrans, J. (2007). Geological evolution of Mount Etna volcano (Italy) from earliest products until the first central volcanism (between 500 and 100 ka ago) inferred from geochronological and stratigraphic data. Int J Earth Sci (Geol Rundsch) 97, 135–152. https://doi.org/10.1007/s00531-006-0152-0

Branca, S., Coltelli, M., & Groppelli, G. (2004). Geological evolution of etna volcano. In: Mt. Etna: Volcano Laboratory. Geophysical Monograph Series, 143, 49-63. doi:10.1029/143GM04

Branca, S., Coltelli, M., & Groppelli, G. (2011). Geological evolution of a complex basaltic stratovolcano: Mount Etna, Italy. Italian Journal of Geosciences, 130(3), 306-317. doi:10.3301/IJG.2011.13

Brancato, A., Hole, J. A., Gresta, S., & Beale, J. N. (2009). Determination of seismogenic structures in southeastern Sicily (Italy) by high-precision relative relocation of microearthquakes. Bulletin of the Seismological Society of America, 99(3), 1921-1936.

Brewer, R. C., & Kenyon, P. M. (1996). Balancing salt dome uplift and withdrawal basin subsidence in cross-section. Journal of Structural Geology, 18(4), 493-504.

Brun, J. P., & Fort, X. (2011). Salt tectonics at passive margins: Geology versus models. Marine and Petroleum Geology, 28(6), 1123-1145.

Burollet, P. F. (1991). Structures and tectonics of Tunisia. Tectonophysics, 195(2-4), 359-369. doi:10.1016/0040-1951(91)90221-D

Burollet, P. F., Mugniot, G. M., & Sweeney, P. (1978). The geology of the Pelagian Block: the margins and basins of Southern Tunisia and Tripolitania. In: Nairn A., Kanes W. & Stelhi F.G. (eds): The Ocean Basins and Margins. Plenum Press, New York, 331-339.

Burrus, J., 1984. Contribution to a geodynamic synthesis of the Provencal Basin (north-western Mediterranean). Mar. Geol. 55, 247e269.

Butler, R. W. H., Maniscalco, R., Sturiale, G., and Grasso, M. (2015). Stratigraphic variations control deformation patterns in evaporite basins: Messinian examples, onshore and offshore Sicily (Italy). J. Geol. Soc. 172, 113–124. doi:10.1144/jgs2014-024

Calanchi, N., Colantoni, P., Rossi, P. L., Saitta, M., & Serri, G. (1989). The strait of Sicily continental rift systems: Physiography and petrochemistry of the submarine volcanic centres. Marine Geology, 87(1), 55-83. doi:10.1016/0025-3227(89)90145-X

Calcagnile, G., D'Ingeo, F., Farrugia, P. & Panza, G.F., (1982). The lithosphere in the central-eastern Mediterranean area, Pageoph, 120, 389-406.

Calò, M., Dorbath, C., Luzio, D., Rotolo, S. G., & D'Anna, G. (2012). Seismic velocity structures of southern Italy from tomographic imaging of the Ionian slab and petrological inferences. Geophysical Journal International, 191(2), 751-764. doi:10.1111/j.1365-246X.2012.05647.x

Camassi, R., & Stucchi, M. (1997). NT4. 1, a parametric catalogue of damaging earthquakes in the Italian area. Gruppo Nazionale per la Difesa dai Terremoti, Milano.

Camerlenghi, A., Del Ben, A., Hubscher, C., Forlin, E., Geletti, R., Brancatelli, G., et al. (2019). Seismic markers of the Messinian salinity crisis in the deep Ionian Basin. Basin Res. 32, 716–738. doi:10.1111/bre.12392

Carbone., S., Branca., S., & Lentini, F. (2009). Note illustrative della Carta Geologica D'Italia alla scala 1:50.000. Foglio 634, Catania. S.EL.CA, Firenze

Carbone S, Grasso M, & Lentini, F (1984). Carta Geologica della Sicilia sud-orientale, scale 1:100.000, S.EL.CA, Firenze

Carbone S, Grasso M, & Lentini, F (1986). Carta Geologica del settore Nord-Orientale Ibleo (Sicilia S.E.), scale 1:50.000, S.EL.CA, Firenze, 1-167

Cardozo, N., & Allmendinger, R. W. (2013). Spherical projections with OSXStereonet. Computers & Geosciences, 51, 193-205.

Carey, S., W. (1955). The orocline concept in geotectonics. Proceedings of the Royal Society of Tasmania 89, 255–288

Carmignani, L., Funedda, A., Oggiano, G., & Pasci, S. (2004). Tectono-sedimentary evolution of southwest Sardinia in the paleogene: Pyrenaic or apenninic dynamic? Geodinamica Acta, 17(4), 275-287. doi:10.3166/ga.17.275-287

Carmignani, L., Oggiano, G., Funedda, A., Conti, P., & Pasci, S. (2016). The geological map of Sardinia (Italy) at 1:250,000 scale. Journal of Maps, 12(5), 826-835. doi:10.1080/17445647.2015.1084544

Carminati, E., Lustrino, M., & Doglioni, C. (2012). Geodynamic evolution of the central and western Mediterranean: Tectonics vs. igneous petrology constraints. Tectonophysics, 579, 173-192.

Cartwright, J. A., Trudgill, B. D., & Mansfield, C. S. (1995). Fault growth by segment linkage: An explanation for scatter in maximum displacement and trace length data from the canyonlands grabens of SE Utah. Journal of Structural Geology, 17(9), 1319-1326. doi:10.1016/0191-8141(95)00033-A

Casini, L., Cuccuru, S., Maino, M., Oggiano, G., Tiepolo, M. (2012). Emplacement of the Arzachena Pluton (Corsica Sardinia Batholith) and the geodynamics of incoming Pangaea. Tectonophysics 544-545, 31-49.

Cassinis, R. (1983). The structure of the earth's crust in the Italian region. In: Wezel, F.C. (Ed.), Sedimentary Basins of Mediterranean Margins. Tectonoprint, Bologna, pp. 19–32.

Catalano, R., & Sulli, A. (2006). Crustal image of the Ionian basin and accretionary wedge. Bollettino Di Geofisica Teorica Ed Applicata, 47(3), 343-374.

Catalano, R., Doglioni, C., & Merlini, S. (2001). On the Mesozoic Ionian Basin. Geophys. J. Int., 144, 49–64, doi:10.1046/j.0956-540X.2000.01287.x.

Catalano, R., Franchino, A., Merlini, S., & Sulli, A. (2000). A crustal section from the eastern Algerian basin to the Ionian ocean (central Mediterranean). Mem. Soc. Geol. Ital., 55, 71–85.

Catalano, R., Valenti, V., Albanese, C., Accaino, F., Sulli, A., Tinivella, U., Gasparo Morticelli M., Zanolla C., Giustiniani, M. (2013). Sicily's fold-thrust belt and slab roll-back: The SI.RI.PRO. seismic crustal transect. Journal of the Geological Society, 170(3), 451-464. doi:10.1144/jgs2012-099

Catalano, R., Valenti, V., Albanese, C., Sulli, A., Gasparo Morticelli, M., Accaino, F., Tinivella U., Giustiniani M., Zanolla C., Avellone G., Basilone, L. (2012). Crustal structures of the Sicily orogene along the SIRIPRO seismic profile. Rendiconti Online Societa Geologica Italiana, 21(PART 1), 67-68.

Catalano, S., De Guidi, G., Lanzafame, G., Monaco, C., Torrisi, S., Tortorici, G., & Tortorici, L. (2006). Inversione tettonica positiva tardo-quaternaria nel Plateau Ibleo (Sicilia SE). Rend. Soc. Geol. It, 2, 118-120.

Catalano S., De Guidi G., Romagnoli G., Torrisi S., Tortorici G. & Tortorici L. (2008). The migration of plate boundaries in SE Sicily: Influence on the large-scale kinematic model of the African promontory in southern Italy. Tectonophysics, 449 (1-4), 41-62.

Catalano, S., Monaco, C., Tortorici, L., Paltrinieri, W., & Steel, N. (2004). Neogene-quaternary tectonic evolution of the southern Apennines. Tectonics, 23(2), TC2003 1-19. doi:10.1029/2003TC001512

Cello, G., Crisci, G. M., Marabini, S., & Tortorici, L. (1985). Transtensive tectonics in the Strait of Sicily: structural and volcanological evidence from the Island of Pantelleria. Tectonics, 4(3), 311-322.

Cernobori, L., Hirn, A., McBride, J.H., Nicolich, R., Petronio, L. & Romanelli, M., (1996). Crustal image of the Ionian basin and its Calabrian margins. Tectonophysics, 264, 175-189.

Chamberlin, R. T. (1910). The Appalachian folds of central Pennsylvania. The Journal of Geology, 18, 228–251. https://doi.org/10.1086/621722

Chamot-Rooke, N., Rangin. C., Le Pichon, X., (2005). DOTMED (Deep Offshore Tectonics of the Mediterranean): a synthesis of deep marine data in the Eastern Mediterranean. Mémoires de la Société géologique de France (1924), 177.

Cherchi, A., & Montadert, L. (1982). Oligo-Miocene rift of Sardinia and the early history of the western Mediterranean basin. Nature, 298(5876), 736-739. doi:10.1038/298736a0.

Chiocci, F. L., Coltelli, M., Bosman, A., & Cavallaro, D. (2011). Continental margin large-scale instability controlling the flank sliding of etna volcano. Earth and Planetary Science Letters, 305(1-2), 57-64. doi:10.1016/j.epsl.2011.02.040

Cifelli, F., Mattei, M., Rossetti, F. (2007). Tectonic evolution of arcuate mountain belts on top of a retreating subduction slab: the example of the Calabrian Arc. J. Geophys. Res. 112.

Cifelli, F., Mattei, M., Della Seta, M. (2008). Calabrian Arc oroclinal bending: the role of subduction. Tectonics 27.

Cirrincione, R., Fazio, E., Fiannacca, P., Ortolano, G., Pezzino, A., & Punturo, R. (2015). The calabria-peloritani orogen, a composite terrane in central mediterranean; its overall architecture and geodynamic significance for a pre-alpine scenario around the tethyan basin. Periodico Di Mineralogia, 84(3B) doi:10.2451/2015PM0446

Cirrincione, R., Ortolano, G., Pezzino, A., & Punturo, R. (2008). Poly-orogenic multi-stage metamorphic evolution inferred via P-T pseudosections: An example from Aspromonte massif basement rocks (southern Calabria, Italy). Lithos, 103(3-4), 466-502. doi:10.1016/j.lithos.2007.11.001

Civile, D., Lodolo, E., Accettella, D., Geletti, R., Ben-Avraham, Z., Deponte, M., . . . Romeo, R. (2010). The Pantelleria graben (Sicily channel, central Mediterranean): An example of intraplate 'passive' rift. Tectonophysics, 490(3-4), 173-183. doi:10.1016/j.tecto.2010.05.008

Cogan, J., Rigo, L., Grasso, M., and Lerche, I. (1989). Flexural tectonics of southeastern Sicily. J. Geodyn. 11 (3), 189–241. doi:10.1016/0264-3707(89)90007-0

Corti, G., Cuffaro, M., Doglioni, C., Innocenti, F., & Manetti, P. (2006). Coexisting geodynamic processes in the sicily channel doi:10.1130/2006.2409(05)

Costa, E., Camerlenghi, A., Polonia, A., Cooper, C., Fabretti, P., Mosconi, A., ... & Wardell, N. (2004). Modeling deformation and salt tectonics in the eastern Mediterranean Ridge accretionary wedge. Geological Society of America Bulletin, 116(7-8), 880-894.

Cotton, C. A. (1950). Tectonic scarps and fault valleys. Geological Society of America Bulletin, 61(7), 717-758.

Cristofolini, R., Lentini, F., Patané, G., & Rasá, R. (1979). Integrazione di dati geologici, geofisici e petrologici per la stesura di un profilo crostale in corrispondenza dell'Etna. Bollettino della Società Geologica Italiana, 98, 239–247.

Cuffaro, M., Billi, A., Bigi, S., Bosman, A., Caruso, C. G., Conti, A., . . . Sgroi, T. (2019). The bortoluzzi mud volcano (Ionian Sea, Italy) and its potential for tracking the seismic cycle of active faults. Solid Earth, 10(3), 741-763. doi:10.5194/se-10-741-2019

Cultrera, F., Barreca, G., Scarfì, L., & Monaco, C. (2015). Fault reactivation by stress pattern reorganization in the Hyblean foreland domain of SE Sicily (Italy) and seismotectonic implications. Tectonophysics, 661, 215-228. doi:10.1016/j.tecto.2015.08.043

Cunningham, W. D., & Mann, P. (2007). Tectonics of strike-slip restraining and releasing bends. Geological Society of London, Special Publications, 290, 1–12. doi:10.1144/SP290.1

D'Addezio, G., and G. Valensise (1991). Metodologie per l'individuazione della struttura sismogenetica responsabile del terremoto del 13 Dicembre 1990, in: Boschi E., Basili, A. (Eds), Contributi allo studio del terremoto della Sicilia orientale del 13 dicembre 1990, I.N.G. 537, 115-125.

D'Agostino N. & Selvaggi G. (2004). Crustal motion along the Eurasia-Nubia plate boundary in the Calabrian Arc and Sicily and active extension in the Messina Straits from GPS measurements. J. Geophys. Res., 109, B11402, doi:10.1029/2004JB002998

Dahlstrom, C. D. A. (1969). Balanced cross sections. Canadian Journal of Earth Sciences, 6, 743–757. https://doi.org/10.1139/e69-069.

Dal Cin, M., Del Ben, A., Mocnik, A., Accaino, F., Geletti, R., Wardell, N., ... & Camerlenghi, A. (2016). Seismic imaging of Late Miocene (Messinian) evaporites from Western Mediterranean back-arc basins. Petroleum Geoscience, 22(4), 297-308.

Dannowski A., Kopp H., Klingelhoefer F., Klaeschen D., Gutscher M. A., Krabbenhoeft A., Dellong D., Rovere M., Graindorge D., Papenberg C., & Klaucke I. (2019). Ionian Abyssal Plain: a window into the Tethys oceanic lithosphere. Solid Earth, 10, 447–462, 2019 https://doi.org/10.5194/se-10-447-2019

De Astis, G., Lucchi, F., Dellino, P., La Volpe, L., Tranne, C. A., Frezzotti, M. L., & Peccerillo, A. (2013). Geology, volcanic history and petrology of Vulcano (central Aeolian archipelago). Geological Society, London, Memoirs, 37(1), 281-349.

De Guidi, G., Caputo, R., and Scudero, S. (2013). Regional and local stress field orientation inferred from quantitative analyses of extension joints: case study from southern Italy. Tectonics 32, 1–13. doi:10.1002/tect.20017

De Lorenzo, S., Di Grazia, G., Giampiccolo, E., Gresta, S., Langer, H., Tusa, G., & Ursino, A. (2004). Source and Qp parameters from pulse width inversion of microearthquake data in southeastern Sicily, Italy. Journal of Geophysical Research: Solid Earth, 109(B7).

De Voogd, B., C. Truffert, N. Chamot-Rooke, P. Huchon, S. Lallemant, and X. Le Pichon (1992), Two-ship deep seismic soundings in the basins of the eastern Mediterranean Sea (Pasiphae cruise), Geophys. J. Int., 109, 536–552, doi:10.1111/j.1365-246X.1992.tb00116.x.

Decima, D. & Wezel, F.C. 1973. Late Miocene evaporites of the central Sicilian Basin, Italy. Initial Reports of the Deep Sea Drilling Project, 13, 1234–1241

Del Ben, A. (1993). Calabrian arc tectonics from seismic exploration. Bollettino Di Geofisica Teorica Ed Applicata, 35(139), 339-347.

Della Vedova, B., and Pellis, G., (1989). New heat flow density measurements in the Ionian Sea. VIII Convegno Nazionale, Gruppo Naz. di Geofis. Della Terra Solida, Rome.

Dellong, D., Klingelhoefer, F., Kopp, H., Graindorge, D., Margheriti, L., Moretti, M., . . . Gutscher, M. -. (2018). Crustal structure of the Ionian basin and eastern Sicily margin: Results from a wide-angle seismic survey. Journal of Geophysical Research: Solid Earth, 123(3), 2090-2114. doi:10.1002/2017JB015312

Dercourt, J., Zonenshain, L. P., Ricou, L.-E., Kazmin, V. G., Le Pichon, X., Knipper, A. L., et al. (1986). Geological evolution of the Tethys belt from the Atlantic to the Pamirs since the Lias. Tectonophysics, 123(1-4), 241–315. https://doi.org/10.1016/0040-1951(86)90199-X

Dewey, J.F., Helman, M.L., Turco, E., Hutton, D.H.W., Knott, S.D., (1989). Kinematics of the Western Mediterranean. In: Coward, M.P., Dietrich, D., Park, R.G. (Eds.), Alpine tectonics. Geol. Soc. Spec. Publ 45, pp. 265–283.

Di Stefano, P., Galacz, A., Mallarino, G., Mindszenty, A., Voros, A., (2002). Birth and early evolution of a Jurassic escarpment: Monte Kumeta, Western Sicily. Facies 46, 273–298.

DISS Working Group (2018). Database of Individual Seismogenic Sources (DISS), Version 3.2.1: A compilation of potential sources for earthquakes larger than M 5.5 in Italy and surrounding areas. http://diss.rm.ingv.it/diss/, Istituto Nazionale di Geofisica e Vulcanologia; DOI:10.6092/INGV.IT-DISS3.2.1.

Doglioni, C. (1991). A proposal for the kinematic modelling of W-dipping subductions - possible applications to the Tyrrhenian-Apennines system. Terra Nova, 3(4), 423-434. doi:10.1111/j.1365-3121.1991.tb00172.x

Dong, G., & Papageorgiou, A.S. (2003). On a new class of kinematic models: Symmetrical and asymmetrical circular and elliptical cracks, Phys. Earth Planet. Inter., 137, 129–151.

Elliott, D. (1983). The construction of balanced cross sections. Journal of Structural Geology, 5, 101. https://doi.org/10.1016/0191-8141(83)90035 -4

Faccenna, C., Becker, T. W., Lucente, F. P., Jolivet, L., & Rossetti, F. (2001a). History of subduction and back-arc extension in the central Mediterranean. Geophysical Journal International, 145(3), 809-820. doi:10.1046/j.0956-540X.2001.01435.x

Faccenna, C., Davy, P., Brun, J. -., Funiciello, R., Giardini, D., Mattei, M., & Nalpas, T. (1996). The dynamics of back-arc extension: An experimental approach to the opening of the Tyrrhenian Sea. Geophysical Journal International, 126(3), 781-795. doi:10.1111/j.1365-246X.1996.tb04702.x

Faccenna, C., Funiciello, F., Giardini, D., Lucente, P., (2001b). Episodic back-arc extension during restricted mantle convection in the Central Mediterranean. Earth Planet. Sci. Lett. 187, 105e116.

Faccenna, C., Molin, P., Orecchio, B., Olivetti, V., Bellier, O., Funiciello, F., ... & Billi, A. (2011). Topography of the Calabria subduction zone (southern Italy): Clues for the origin of Mt. Etna. Tectonics, 30(1).

Faccenna, C., Piromallo, C., Crespo-Blanc, A., Jolivet, L., & Rossetti, F. (2004). Lateral slab deformation and the origin of the western Mediterranean arcs. Tectonics, 23(1), TC1012 1-21. doi:10.1029/2002TC001488

Farrugia, P. & Panza, G.F., (1981). Continental character of the lithosphere beneath the Ionian sea, in The Solution of the Inverse Problem in Geophysical Interpretation, pp. 327-334, ed. Cassinis, R., Plenum, New York.

Fazio, E., Cirrincione, R., & Pezzino, A. (2008). Estimating P-T conditions of alpine-type metamorphism using multistage garnet in the tectonic windows of the cardeto area (southern Aspromonte massif, Calabria). Mineralogy and Petrology, 93(1-2), 111-142. doi:10.1007/s00710-007-0216-2

Ferrara, F. (1829). Storia di Catania sino alla fine del secolo XVIII. Dato.

Ferrucci, F., G. Gaudiosi, A. Hirn, and R. Nicolich (1991), Ionian Basin and Calabria Arc: Some new elements from DSS data, Tectonophysics, 195, 411–419, doi:10.1016/0040-1951(91)90223-F.

Finetti, I. (1982). Structure, stratigraphy and evolution of central Mediterranean (pelagian sea, Ionian Sea). Bollettino Di Geofisica Teorica Ed Applicata, 24(96), 247-312.

Finetti, I. (1984). Geophysical study of the sicily channel rift zone. Bollettino Di Geofisica Teorica Ed Applicata, 26(101-102), 3-28.

Finetti, I. (1985). Structure and evolution of central Mediterranean (Pelagian and Ionian Seas). In: Stanley, D.J., Wezel, F.C. (Eds.). Geological evolution of the Mediterranean basin. Springer, 215-30.

Finetti, I. (2004). Innovative CROP seismic highlights on the Mediterranean Region. In: Crescenti, U., et al., eds., Geology of Italy, special volume of the Italian Geological Society for the IGC 32 Florence, p. 132–140.

Finetti, I., and C. Morelli (1973), Geophysical exploration of the Mediterranean Sea, Boll. Geofis. Teor. Appl., 15, 263–341.

Finetti I., Lentini F., Carbone S., Catalano S. & Del Ben A. (1996). Il sistema Appennino meridionale-Arco Calabro-Sicilia nel Mediterraneo centrale: tudio geologico-geofisico. Mem. Soc. Geol. It., 115: 529-559.

Finetti, I., Lentini, F., Carbone, S., Del Ben, A., Di Stefano, A., Guarnieri, P., Pipan, M., and Prizzon, A. (2005a). Crustal tectonostratigraphy and geodynamics of the southern Apennines from CROP and other integrating geophysical-geological data. In: Finetti, I.R., ed., CROP: Deep seismic exploration of the Mediterranean region, special volume: Amsterdam, Elsevier, chapter 12, p. 225–262

Finetti, I., Lentini, F., Carbone, S., Del Ben, A., Di Stefano, A., Forlin, E., Guarnieri, P., Pipan, M., and Prizzon, A. (2005b). Geological outline of Sicily and lithospheric tectono-dynamics of its Tyrrhenian margin from new CROP seismic data. In: Finetti, I.R., ed., CROP: Deep seismic exploration of the Mediterranean region, special volume: Amsterdam, Elsevier, chapter 15, p. 319–376.

Gallais, F., Graindorge, D., Gutscher, M.-A., & Klaeschen, D. (2013). Propagation of a lithospheric tear fault (STEP) through the western boundary of the calabrian accretionary wedge offshore eastern Sicily (southern Italy). Tectonophysics, 602, 141-152. doi:10.1016/j.tecto.2012.12.026

Gallais, F., Gutscher, M. -., Klaeschen, D., & Graindorge, D. (2012). Two-stage growth of the calabrian accretionary wedge in the Ionian Sea (central Mediterranean): Constraints from depth-migrated multichannel seismic data. Marine Geology, 326-328, 28-45. doi:10.1016/j.margeo.2012.08.006

Gambino, S., Barreca, G., Gross, F., Monaco, C., Gutscher, M.-A.., & Alsop, G. I. (2021b). Assessing the rate of crustal extension by 2D sequential restoration analysis: A case study from the active portion of the malta escarpment. Basin Research, doi:10.1111/bre.12621

Gambino, S., Barreca, G., Gross, F., Monaco, C., Krastel, S., & Gutscher, M.-A. (2021a). Deformation Pattern of the Northern Sector of the Malta Escarpment (Offshore SE Sicily, Italy): Fault Dimension, Slip Prediction, and Seismotectonic Implications. Front. Earth Sci. 8:594176. doi:10.3389/feart.2020.594176

Gardiner, W., Grasso, M., & Sedgeley, D. (1995). Plio-Pleistocene fault movement as evidence for mega-block kinematics within the Hyblean-Malta Plateau, central Mediterranean. Journal of Geodynamics, 19(1), 35–51. https://doi.org/10.1016/0264-3707(94)00006-9

Gautier, F., Clauzon, G., Suc, J. -., Cravatte, J., & Violanti, D. (1994). Age and duration of the messinian salinity crisis. [Age et duree de la crise de salinite messinienne] Comptes Rendus - Academie Des Sciences, Serie II: Sciences De La Terre Et Des Planetes, 318(8), 1103-1109.

Ge, Z., Gawthorpe, R. L., Rotevatn, A., Zijerveld, L., Jackson, C. A. L., & Oluboyo, A. (2020). Minibasin depocentre migration during diachronous salt welding, offshore Angola. Basin Research, 32(5), 875-903.

Ge, Z., Warsitzka, M., Rosenau, M., & Gawthorpe, R. L. (2019). Progressive tilting of salt-bearing continental margins controls thin-skinned deformation. Geology, 47(12), 1122-1126.

Ghisetti, F., & Vezzani, L. (1980). The structural features of the Iblean Plateau and of the mount Judica area (Southeastern Sicily); a microtectonic contribution to the deformational history of the calabrian arc. Bollettino della Societa Geologica Italiana, 99(1-2), 57–102.

Ghisetti, F., & L. Vezzani (1982). Different styles of deformation in the Calabrian Arc [southern Italy]: Implications for a seismotectonic zoning. Tectonophysics, 85, 149–165.

Gibbs, A. D. (1983). Balanced cross-section construction from seismic sections in areas of extensional tectonics. Journal of Structural Geology, 5, 153–160. https://doi.org/10.1016/0191-8141(83)90040 -8

Gibbs, A. D. (1984). Structural evolution of extensional basin margins. Journal of the Geological Society, London, 141, 609–620. https://doi.org/10.1144/gsjgs.141.4.0609

Gorini, C., Le Marrec, A., Mauffret, A. (1993). Contribution to the structural and sedimentary history of the Gulf of Lions (western Mediterranean) from the ECORS profiles, industrial seismic profiles and well data. Bull. Soc. Geol. France 164, 353-363.

Gorini C., Mauffret A., Guennoc P., Le Marrec A. (1994) Structure of the Gulf of Lions (Northwestern Mediterranean Sea): A Review. In: Mascle A. (eds) Hydrocarbon and Petroleum Geology of France. Special Publication of the European Association of Petroleum

Geoscientists, vol 4. Springer, Berlin, Heidelberg. https://doi.org/10.1007/978-3-642-78849-9_17

Goteti, R., Ings, S. J., & Beaumont, C. (2012). Development of salt minibasins initiated by sedimentary topographic relief. Earth and Planetary Science Letters, 339, 103-116.

Govers, R., & Wortel, M. J. R., (2005). Lithosphere tearing at STEP faults: response to edges of subduction zones. Earth Planet Sci. Lett. 236 (1–2), 505–523. doi:10.1016/j.epsl.2005.03.022

Grasso, M., & Lentini, F., 1982, Sedimentary and tectonic evolution of the eastern Hyblean Plateau (southeast Sicily) during Late Cretaceous to Quaternary time: Palaeogeography, Palaeoclimatology, Palaeoecology, v. 39, p. 261–280, doi:10.1016/0031-0182(82)90025-6.

Grasso, M., & Reuther, C. D. (1988). The western margin of the Hyblean Plateau: a neotectonic transform system on the SE Sicilian foreland. Ann. Tect. 2, 107–120.

Grasso, M., Pedley, H. M., Behncke, B., Maniscalco, R., and Sturiale, G. (2004). "Integrated the neogene-frontiers quaternary sedimentation and volcanism in the northern Hyblean Plateau (Sicily)," in Mapping geology in Italy Editors G. Pasquarè and C. Venturini (Roma, IT: APAT), 159–166.

Gratier, J. P., Guiller, B., Delorme, A., & Odonne, F. (1991). Restoration and balance of a folded and faulted surface by best-fitting of finite elements: Principle and applications. Journal of Structural Geology, 13, 111–115. https://doi.org/10.1016/0191-8141(91)90107 -T

Groshong, R. H. Jr (1990). Unique determination of normal fault shape from hangingwall bed geometry in detached half grabens. Eclogae Geologicae Helvetiae, 83, 455e471.

Gueguen, E., C. Doglioni, and M. Fernandez (1998), On the post-25 Ma geodynamic evolution of the western Mediterranean, Tectonophysics, 298, 259–269, doi:10.1016/S0040-1951(98)00189-9.

Guidoboni, E., Ferrari, G., Mariotti, D., Comastri, A., Tarabusi, G., & Valensise, G. (2007). Catalogue of Strong Earthquakes in Italy (461 BC-1997) and Mediterranean Area (760 BC-1500).

Gutscher, M. A., Dellong, D., Dominguez, S., Malavieille, J., Graindorge, D., & Klingelhoefer, F. (2019). Strike-slip faulting in the calabrian accretionary wedge: using analog modeling to test the kinematic boundary conditions of geodynamic models. In Transform Plate Boundaries and Fracture Zones (pp. 321-337). Elsevier. https://doi.org/10.1016/B978-0-12-812064-4.00013-X

Gutscher, M.-A., Dominguez, S., Mercier de Lepinay, B., Pinheiro, L., Gallais, F., Babonneau, N., et al. (2016). Tectonic expression of an active slab tear from high-resolution seismic and bathymetric data offshore Sicily (Ionian Sea). Tectonics 35, 39–54. doi:10.1002/2015TC003898

Gutscher, M.-A., Kopp, H., Krastel, S., Bohrmann, G., Garlan, T., Zaragosi, S., Klaucke, I., Wintersteller, P., Loubrieu, B., LeFaou, Y., San Pedro, L., Dominguez, S., Rovere, M., Mercier de Lepinay, B., Ranero, C., Sallares, V. (2017). Active tectonics of the calabrian subduction revealed by new multi-beam bathymetric data and high-resolution seismic profiles in the Ionian Sea (central Mediterranean). Earth and Planetary Science Letters, 461, 61-72. doi:10.1016/j.epsl.2016.12.020

Gvirtzman, Z., & Nur, A. (1999). The formation of mount etna as the consequence of slab rollback. Nature, 401(6755), 782-785. doi:10.1038/44555

Hanks, T. C., & H. Kanamori (1979). A moment magnitude scale, J. Geophys. Res. 84, no. B5, 2348–2350.

Hatzfeld, D., M. Besnard, K. Makropoulos, and P. Hatzidimitriou (1993), Microearthquake seismicity and fault-plane solutions in the southern Aegean and its geodynamic implications, Geophys. J. Int., 115, 799–818, doi:10.1111/j.1365-246X.1993.tb01493.x.

Henriquet, M., Dominguez, S., Barreca, G., Malavieille, J., Cadio, C., & Monaco, C. (2019). Deep origin of the dome-shaped Hyblean Plateau, southeastern Sicily: A new tectono-magmatic model. Tectonics, 38(12), 4488-4515.

Henriquet, M., Dominguez, S., Barreca, G., Malavieille, J., & Monaco, C. (2020). Structural and tectono-stratigraphic review of the Sicilian orogen and new insights from analogue modeling. Earth-Science Reviews, 103257.

Hinz, K. (1974), Results of seismic refraction and seismic reflection measurements in the Ionian Sea, Geol. Jahrb., 2, 33–65.

Hirn, A., Nicolich, R., Gallart, J., Laigle, M., Cernobori, L., & ETNASEIS Scientific Group. (1997). Roots of Etna volcano in faults of great earthquakes. Earth and Planetary Science Letters, 148(1-2), 171-191.

Hossack, J. R. (1979). The use of balanced cross sections in the calculation of orogenic contraction: A review. Journal of the Geological Society London, 136, 705e711. https://doi.org/10.1144/gsjgs.136.6.0705

Hsü, K. J., Montadert, L., Bernoulli, D., Bizon, G., Cita, M., Erickson, A., et al. (1978). "Site 374: messina abyssal plain part 1," in Initial reports of the deep-sea drilling project Washington, DC: U.S. Government Printing Office, Vol. 42.

Isaaks, E.H. & Srivastrava, R.M., (1989). An introduction to applied geostatistics. NewYork: Oxford University Press.

Jamaludin, S. N. F., Latiff, A. H. A., & Ghosh, D. P. (2015). Structural balancing vs horizon flattening on seismic data: Example from extensional tectonic setting. IOP Conference Series: Earth and Environmental Science, 23, 012003. https://doi.org/10.1088/1755-1315/23/1/012003

Jitmahantakul, S., Phetheet, J., & Kanjanapayont, P. (2020). 2D sequential restoration and basin evolution of the Wichianburi sub-basin, Phetchabun basin, central Thailand. Frontiers in Earth Science, 8, 578218. https://doi.org/10.3389/feart.2020.578218

Jolivet, L., Faccenna, C., Agard, P., Frizon de Lamotte, D., Menant, A., Sternai, P., & Guillocheau, F. (2015). Neo-Tethys geodynamics and mantle convection: From extension to compression in Africa and a conceptual model for obduction. Canadian Journal of Earth Sciences, 53(11), 1190–1204.

Jordan, T.E. (1995). Retroarc foreland and related basins. In: Busby, C.J., and Ingersoll, R.V., eds. Tectonics of sedimentary basins. Oxford, Blackwell Science, 331–362.

Kanamori, H. (1977). The energy release in great earthquakes, J. Geophys. Res. 82, no. 20, 2981–2987.

Kaneko, Y., & Shearer, P.M. (2015). Variability of seismic source spectra, estimated stress drop, and radiated energy, derived from cohesive-zone models of symmetrical and asymmetrical circular and elliptical ruptures, J. Geophys. Res. Solid Earth, 120, doi:10.1002/2014JB011642.

Kastens, K.A., & Mascle, J.L. (1990). The Geological Evolution of the Tyrrhenian Sea: An Introduction to the Scientific Results of ODP Leg 107.

Krastel, S. (2016). RV POSEIDON-CRUISE POS496, Malaga–Catania, 24.03. 2016-04.04. 2016, Short Cruise Report: MAGOMET-Offshore flank movement of Mount Etna and associated landslide hazard in the Ionian Sea (Mediterranean Sea).

Krézsek, C., Adam, J., & Grujic, D. (2007). Mechanics of fault and expulsion rollover systems developed on passive margins detached on salt: insights from analogue modelling and optical strain monitoring. Geological Society, London, Special Publications, 292(1), 103-121.

Krijgsman, W., Fortuin, A. R., Hilgen, F. J., & Sierro, F. J. (2001). Astrochronology for the messinian sorbas basin (SE spain) and orbital (precessional) forcing for evaporite cyclicity. Sedimentary Geology, 140(1-2), 43-60. doi:10.1016/S0037-0738(00)00171-8

Krijgsman, W., Hilgen, F. J., Raffi, I., Sierro, F. J., & Wilson, D. S. (1999). Chronology, causes and progression of the Messinian salinity crisis. Nature, 400(6745), 652-655.

Lavecchia G., Ferrarini F., De Nardis R., Visini F. & Barbano M.S. (2007). Active thrusting as a possible seismogenic source in Sicily (Southern Italy): some insights from integrated structural-kinematic and seismological data. Tectonophysics, 445, 145-167.

Le Pichon, X., Huchon, P., Angelier, J., Lybéris, N., Boulin, J., Bureau, D., . . . Thiébault, F. (1982). Subduction in the hellenic trench: Probable role of a thick evaporitic layer based on seabeam and submersible studies doi:10.1144/GSL.SP.1982.010.01.21

Lentini, F. (1982). The geology of the Mt. Etna basement: Memorie della Società Geologica Italiana, 23, 7–25.

Lentini, F., Carbone, S. (2014). Geologia della SiciliaMem. Descr. Carta Geol. d'It. Vol. XCV (2014), pp. 7-414 figg. 533, tabb. 5; Tavv. 5

Lentini, F., Carbone, S., & Catalano, S. (1994). Main structural domains of the central Mediterranean region and their Neogene tectonic evolution. Bollettino Di Geofisica Teorica Ed Applicata, 36(141-144), 103-125.

Lentini, F., Carbone, S., Catalano, S., & Grasso, M. (1995). Principali lineamenti strutturali della Sicilia Nord-orientale. Vol. Spec. Studi Geol. Camerti(1995/2): 319-329.

Lentini, F., Carbone, S., & Guarnieri, P., (2006). Collisional and post-collisional tectonics of the Apenninic-Maghrebian orogen (southern Italy). In: Dilek, Y., and Pavlides, S., eds., Post-collisional tectonics and magmatism in the Mediterranean region and Asia. Geological Society of America Special Paper 409, p. 57–81, doi:10.1130/2006.2409(04).

Lentini, F., Carbone, S., Di Stefano, A., & Guarnieri, P. (2002). Stratigraphical and structural constraints in the lucanian Apennines (southern Italy): Tools for reconstructing the geological evolution. Journal of Geodynamics, 34(1), 141-158. doi:10.1016/S0264-3707(02)00031-5

Lentini, F., Catalano, S., and Carbone, S., (1996). The External Thrust System in Southern Italy: A target for petroleum exploration: Petroleum Geoscience, Vol. 2, pp. 333–342.

Lentini, F. & Vezzali, L. (1974). Carta Geologica delle Madonie (Sicilia centrosettentrionale), 1:50.000. L.A.C., Firenze.

Leonard, M. (2010). Earthquake fault scaling: Self-consistent relating of rupture length, width, average displacement, and moment release. Bulletin of the Seismological Society of America, 100(5A), 1971-1988.

Lickorish, W. H., Grasso, M., Butler, R. W. H., Argnani, A., & Maniscalco, R. (1999). Structural styles and regional tectonic setting of the 'gela nappe' and frontal part of the maghrebian thrust belt in Sicily. Tectonics, 18(4), 655-668. doi:10.1029/1999TC900013

Liner, C. L. (2004). Elements of 3D Seismology: Pennwell Corporation. Tulsa, Oklahoma.

Lofi, J., Deverchère, J., Gaullier, V., Gillet, H., Gorini, C., Guennoc, P., et al. (2011). Seismic atlas of the messinian salinity crisis markers in the Mediterranean and Black Seas. Mém. Soc. Géol. CCGM 179, 1–72.

Lombardo, G. (1985). The Catania earthquake of February 4, 1169. Atlas of isoseismal maps of italian earthquake, 12-13.

Lonergan, L., & White, N. (1997). Origin of the Betic Rif mountain belt. Tectonics, 16(3), 504–522. https://doi.org/10.1029/96TC03937

Longaretti, G., S. Rocchi, and L. Ferrari (1991), Il magmatismo dell'avampaese ibleo (Sicilia orientale) tra il Trias e il Quaternario: Dati di sottosuolo della Piana di Catania dal Pleistocene al Miocene medio, Mem. Soc. Geol. Ital., 47, 537– 555.

López-Mir, B. (2013). Extensional salt tectonics in the Cotiella post-rift basin (south-central Pyrenees): 3D structure and evolution. Dissertation, University of Barcelona.

Lopez-Mir, B., Anton Muñoz, J., & García Senz, J. (2014). Restoration of basins driven by extension and salt tectonics: Example from the cotiella basin in the central Pyrenees. Journal of Structural Geology, 69(PA), 147–162. https://doi.org/10.1016/j.jsg.2014.09.022

Madariaga, R. (1976). Dynamics of an expanding circular fault. Bulletin of the Seismological Society of America, 66(3), 639-666.

Maesano, F. E., Tiberti, M. M., & Basili, R. (2020). Deformation and fault propagation at the lateral termination of a subduction zone: The Alfeo fault system in the calabrian arc, southern Italy. Frontiers in Earth Science, 8 doi:10.3389/feart.2020.00107

Makris, J., R. Nicolich, and W. Weigel (1986), A seismic study of the western Ionian Sea, Ann. Geophys., 6, 665–678.

Malinverno, A., & W. B. F. Ryan (1986), Extension in the Tyrrhenian Sea and shortening in the Apennines as result of arc migration driven by sinking of the lithosphere, Tectonics, 5(2), 227–245, doi:10.1029/TC005i002p00227.

Mantovani, E., Viti, M., Babbucci, D., Tamburelli, C., & Cenni, N. (2020). Geodynamics of the central-western Mediterranean region: Plausible and non-plausible driving forces. Marine and Petroleum Geology, 113 doi:10.1016/j.marpetgeo.2019.104121

Manuella, F. C., Carbone, S., & Barreca, G. (2012). Origin of saponite-rich clays in a fossil serpentinite-hosted hydrothermal system in the crustal basement of the Hyblean plateau (Sicily, Italy). Clays and Clay Minerals, 60(1), 18-31. doi:10.1346/CCMN.2012.0600102

Marrett, R., & Allmendinger, R. W. (1990). Kinematic analysis of fault-slip data. Journal of structural geology, 12(8), 973-986.

Marshak, S. (2004). Salients, Recesses, Arcs, Oroclines, and Syntaxes — a review of ideas concerning the formation of map-view curves in fold-thrust belts. McClay, K.R. (ed.). Thrust tectonics and hydrocarbon systems. American Association of Petroleum Geologists Memoir 82, 131–156.

Maerten, L. (2007). Geomechanics to solve structure related issues in petroleum reservoirs. AAPG European Regulation Newsletter, 2, 2–3.

Mascle, J., and E. Chaumillon (1998), An overview of Mediterranean Ridge collisional accretionary complex as deduced from multichannel seismic data, Geo Mar. Lett., 18, 81–89, doi:10.1007/s003670050056.

Mastrolembo Ventura, B., Serpelloni, E., Argnani, A., Bonforte, A., Bürgmann, R., Anzidei, M., . . . Puglisi, G. (2014). Fast geodetic strain-rates in eastern Sicily (southern Italy): New insights into block tectonics and seismic potential in the area of the great 1693 earthquake. Earth and Planetary Science Letters, 404, 77-88. doi:10.1016/j.epsl.2014.07.025

Mattei, M., Cipollari, P., Cosentino, D., Argentieri, A., Rossetti, F., Speranza, F., Di Bella, L., 2002. The Miocene tectono-sedimentary evolution of the southern Tyrrhenian Sea: stratigraphy, structural and palaeomagnetic data from the on-shore Amantea basin (Calabrian Arc, Italy). Basin Res. 14, 147e168.

Mattia, M., Bruno, V., Cannavò, F., & Palano, M. (2012). Evidences of a contractional pattern along the northern rim of the Hyblean plateau (Sicily, Italy) from GPS data. Geologica Acta, 10(1), 63-70. doi:10.1344/105.000001705

Mencos, J. (2011). Metodologies de reconstrucció i modetització 3D d'estructures geològiques: Anticlinal de Sant Corneli–Bóixols (Pirineus centrals). D dissertation, Universitat de Barcelona, Barcelona.

Mercalli, G., (1909). Contributo allo studio del terremoto calabro-messinese del 28 dicembre 1908. «Atti del R. Istituto di Incoraggiamento di Napoli», serie VI, vol. VII, pp. 249-292.

Meschis, M., Scicchitano, G., Roberts, G. P., Robertson, J., Barreca, G., Monaco, C., . . . Scardino, G. (2020). Regional deformation and offshore crustal local faulting as combined processes to explain uplift through time constrained by investigating differentially uplifted late quaternary paleoshorelines: The foreland Hyblean plateau, SE Sicily. Tectonics, 39(12) doi:10.1029/2020TC006187

Micallef, A., Camerlenghi, A., Georgiopoulou, A., Garcia-Castellanos, D., Gutscher, M.-A., Lo Iacono, C., . . . Accettella, D. (2019). Geomorphic evolution of the malta escarpment and implications for the Messinian evaporative drawdown in the eastern Mediterranean Sea. Geomorphology, 327, 264-283. doi:10.1016/j.geomorph.2018.11.012

Milano, M., Kelemework, Y., La Manna, M. et al. Crustal structure of Sicily from modelling of gravity and magnetic anomalies. Sci Rep 10, 16019 (2020). https://doi.org/10.1038/s41598-020-72849-z

Milia, A., Torrente, M.M., 2014. Early-stage rifting of the Southern Tyrrhenian region: the Calabriae Sardinia breakup. J. Geodyn. 81, 17-29.

Minelli, L., & Faccenna, C. (2010). Evolution of the calabrian accretionary wedge (central Mediterranean). Tectonics, 29(4), 1-21. doi:10.1029/2009TC002562

Misra, A. A., & Yadav, A. (2018). Introduction to Seismic Data. Atlas of Structural Geological Interpretation from Seismic Images, 11.

Monaco, C., & Tortorici, L. (2000). Active faulting in the calabrian arc and eastern Sicily. Journal of Geodynamics, 29(3-5), 407-424. doi:10.1016/S0264-3707(99)00052-6

Monaco, C., Bianca, M., Catalano, S., De Guidi, G., and Tortorici, L., 2002, Sudden change in the late Quaternary tectonic regime in eastern Sicily: Evidences from geological and geomorphological features: Bollettino della Società Geologica Italiana, v. 121, no. 1, p. 901–913.

Monaco, C., Catalano, S., De Guidi, G., & Tortorici, L. (2005). Geology of the urban area of catania (eastern Sicily). Advances in Earthquake Engineering, 14, 83-102.

Monaco, C., Tortorici, L., Nicolich, R., Cernobori, L., & Costa, M. (1996). From collisional to rifted basins: An example from the southern calabrian arc (Italy). Tectonophysics, 266(1-4), 233-249. doi:10.1016/S0040-1951(96)00192-8

Montone, P., Mariucci, M. T., & Pierdominici, S. (2012). The Italian present-day stress map. Geophys. J. Int. 189 (2), 705–716. doi:10.1111/j.1365-246X.2012.05391.x

Montone P., Mariucci M. T., Pondrelli S. & Amato A. (2004). An improved stress map for Italy and surrounding regions (central Mediterranean). Journal of Geophysical Research, 109 (B10410), 1-22, doi:10.1029/1003JB002703

Morris, A., Ferrill, D. A. & Henderson, D. B. (1996). Slip-tendency analysis and fault reactivation. Geology, 24(3), 275-278.

Mulargia, F., Broccio, F., Achilli, V., & Baldi, P. (1985). Evaluation of a seismic quiescence pattern in southeastern Sicily. Tectonophysics, 116(3-4), 335-364.

Musumeci, C., Patanè, D., Scarfí, L., & Gresta, S. (2005). Stress directions and shear-wave anisotropy: Observations from local earthquakes in southeastern Sicily, Italy. Bulletin of the Seismological Society of America, 95(4), 1359-1374. doi:10.1785/0120040108

Musumeci, C., Scarfì, L., Palano, M., & Patanè, D. (2014). Foreland segmentation along an active convergent margin: New constraints in southeastern Sicily (Italy) from seismic and geodetic observations. Tectonophysics, 630(C), 137-149. doi:10.1016/j.tecto.2014.05.017

Nicol, A., Watterson, J., Walsh, J. J., & Childs, C. (1996). The shapes, major axis orientations and displacement patterns of fault surfaces. Journal of Structural Geology, 18(2-3), 235-248.

Nicolich, R., Laigle, M., Hirn, A., Cernobori, L., & Gallart, J. (2000). Crustal structure of the Ionian margin of Sicily: Etna volcano in the frame of regional evolution. Tectonophysics, 329(1-4), 121-139. doi:10.1016/S0040-1951(00)00192-X

Nigro, F., Renda, P., (2002). From Mesozoic extension to Tertiary collision: deformation patterns in the units of the North-Western Sicilian chain. Bolletino della Societa Geologica Italiana 121, 87–97.

Ogniben, L. (1960). Nota illustrativa dello schema geologico della Sicilia nordorientale. Rivista Mineraria Siciliana, Vol. 11, p. 183–212.

Palano, M. (2015). On the present-day crustal stress, strain-rate fields and mantle anisotropy pattern of Italy. Geophysical Journal International, 200(2), 969-985.

Palano, M., Ferranti, L., Monaco, C., Mattia, M., Aloisi, M., Bruno, V., Cannavò, F, Siligato, G. (2012). GPS velocity and strain fields in Sicily and southern Calabria, Italy: Updated geodetic constraints on tectonic block interaction in the central Mediterranean. Journal of Geophysical Research: Solid Earth, 117(7) doi:10.1029/2012JB009254

Paliaga, G. (2015). Erosion triangular facets as markers of order in an open dissipative system. Pure and Applied Geophysics, 172(7), 1985-1997.

Patacca, E., R. Sartori, and P. Scandone (1990), Tyrrhenian basin and Apenninic arcs. Kinematic relations since late Tortonian times, Mem. Soc. Geol. Ital., 45, 425–451.

Patacca, E., Scandone, P., Giunta, G., and Liguori, V. (1979). Mesozoic paleotectonic evolution of the Ragusa zone (southern Sicily). Geol. Rom. 18, 331–369.

Peccerillo, A., De Astis, G., Faraone, D., Forni, F., & Frezzotti, M. L. (2013). Compositional variations of magmas in the Aeolian arc: implications for petrogenesis and geodynamics. Geological Society, London, Memoirs, 37(1), 491-510. doi:10.1144/M37.15

Pedley, M., and Grasso, M. (1992). Miocene syntectonic sedimentation along the western margins of the Hyblean-Malta platform: a guide to plate margin processes in the central Mediterranean. J. Geodyn. 15 (1–2), 19–37. doi:10.1016/0264-3707(92)90004-C

Peel, F. J. (2014a). The engines of gravity-driven movement on passive margins: Quantifying the relative contribution of spreading vs. gravity sliding mechanisms. Tectonophysics, 633, 126-142.

Peel, F. J. (2014b). How do salt withdrawal minibasins form? insights from forward modelling, and implications for hydrocarbon migration. Tectonophysics, 630(C), 222-235. doi:10.1016/j.tecto.2014.05.027

Piatanesi, A., & S. Tinti (1998). A revision of the 1693 eastern Sicily earthquake and tsunami. J. Geophys. Res. 103, 2749-2758.

Platania, G., (1909). Il maremoto dello Stretto di Messina del 28 dicembre 1908. Boll. Soc. Sismol. It. 13, 369–458.

Polonia, A., Camerlenghi, A., Davey, F., & Storti, F., (2002). Accretion, structural style, and syncontractional sedimentation in the eastern Mediterranean Sea. Mar. Geol., 186, 127–144, doi:10.1016/S0025-3227(02)00176-7.

Polonia, A., Torelli, L., Artoni, A., Carlini, M., Faccenna, C., Ferranti, L., Gasperini, L., Govers, R., Klaeschen, D., Monaco, C., Neri, G., Nijholt, N.,Orecchio, B. & Wortel, R. (2016). The Ionian and alfeo-etna fault zones: New segments of an evolving plate boundary in the central Mediterranean sea? Tectonophysics, 675, 69-90. doi:10.1016/j.tecto.2016.03.016

Polonia, A., Torelli, L., Capozzi, R., Riminucci, F., Artori, A., Ramella, R., & Calarc Group. (2008). African/Eurasian plate boundary in the Ionian Sea: shortening and strike slip deformation in the outer Calabrian Arc accretionary wedge. Convegno Nazionale, Gruppo Naz. di Geofis. della Terra Solida, Trieste, Italy.

Polonia, A., L. Torelli, L. Gasperini & P. Mussoni (2012). Active faults and historical earthquakes in the Messina Straits area (Ionian Sea), Nat. Hazards Earth Syst. Sci., 12, 2311-2328, doi:10.5194/nhess-12-2311-2012.

Polonia, A., Torelli, L., Mussoni, P., Gasperini, L., Artoni, A., & Klaeschen, D. (2011). The calabrian arc subduction complex in the Ionian Sea: Regional architecture, active deformation, and seismic hazard. Tectonics, 30(5) doi:10.1029/2010TC002821

Polonia, A., Torelli, L., Gasperini, L., Cocchi, L., Muccini, F., Bonatti, E., Hensen, C., Schmidt, M., Romano, S., Artoni, A., Carlini, M. (2017). Lower plate serpentinite diapirism in the calabrian arc subduction complex. Nature Communications, 8(1) doi:10.1038/s41467-017-02273-x

Prada, M., Sallares, V., Ranero, C. R., Vendrell, M. G., Grevemeyer, I., Zitellini, N., & de Franco, R. (2018). Spatial variations of magmatic crustal accretion during the opening of the Tyrrhenian back-arc from wide-angle seismic velocity models and seismic reflection images. Basin Research, 30, 124-141. doi:10.1111/bre.12211

Privitera, F., (1695). Dolorosa tragedia rappresentata nel Regno di Sicilia nella città di Catania, Catania.

Ragg, S., Grasso, M., and Müller, B. (1999). Patterns of tectonic stress in Sicily from borehole breakout observations and finite element modeling. Tectonics 18 (4), 669–685. doi:10.1029/1999TC900010

Ramberg, H. (1981). The role of gravity in orogenic belts. Geological Society, London, Special Publications, 9(1), 125-140.

Rebesco, M., Camerlenghi, A., Munari, V., Mosetti, R., Ford, J., Micallef, A., & Facchin, L. (2021). Bottom current-controlled Quaternary sedimentation at the foot of the Malta Escarpment (Ionian Basin, Mediterranean). Marine Geology, 441, 106596.

Reston, T. J., von Huene, R., Dickmann, T., Klaeschen, D., & Kopp, H. (2002). Frontal accretion along the western Mediterranean Ridge: The effect of the Messinian evaporites on wedge mechanics and structural style. Mar. Geol., 186, 59–82, doi:10.1016/S0025-3227(02)00173-1.

Reuther, C. D., & Eisbacher, G. H. (1985). Pantelleria Rift-crustal extension in a convergent intraplate setting. Geologische Rundschau, 74(3), 585-597.

Reuther, C.D., (1989). Extensional tectonics within the Central Mediterranean of the Afro-European zone of convergence. Memorie della Società Geologica Italiana, v. 38, pp. 69–80

Reuther, C. D., Ben-Avraham, Z., & Grasso, M. (1993). Origin and role of major strike-slip transfers during plate collision in the central Mediterranean. Terra Nova 5(3), 249-257.

Rey, P., Vanderhaeghe, O., & Teyssier, C. (2001). Gravitational collapse of the continental crust: definition, regimes and modes. Tectonophysics, 342(3-4), 435-449.

Rocchi, S., G. Longaretti, and M. Salvadori (1998), Subsurface Mesozoic and Cenozoic magmatism in south-eastern Sicily: Distribution, volume and geochemistry of magmas, Acta Vulcanol., 10, 395– 408.

Rojo, L. A., Koyi, H., Cardozo, N., & Escalona, A. (2020). Salt tectonics in salt-bearing rift basins: Progradational loading vs extension. Journal of Structural Geology, 141, 104193. https://doi.org/10.1016/j.jsg.2020.104193

Romagnoli, G., Catalano, S., Pavano, F., & Tortorici, G. (2015). Geological map of the Tellaro River Valley (Hyblean Foreland, southeastern Sicily, Italy). Journal of Maps, 11(1), 66–74. https://doi.org/10.1080/17445647.2014.944878

Rosenbaum, G., & Lister, G. S. (2004). Neogene and quaternary rollback evolution of the tyrrhenian sea, the apennines, and the sicilian maghrebides. Tectonics, 23(1), TC1013 1-17. doi:10.1029/2003TC001518

Rossi, S., and R. Sartori (1981), A seismic reflection study of the external Calabrian Arc in the northern Ionian Sea (eastern Mediterranean), Mar. Geophys. Res., 4, 403–426, doi:10.1007/BF00286036.Rotolo, S. G., Castorina, F., Cellura, D., & Pompilio, M. (2006). Petrology and geochemistry of submarine volcanism in the Sicily channel rift. Journal of Geology, 114(3), 355-365. doi:10.1086/501223.

Roveri, M., Flecker, R., Krijgsman, W., Lofi, J., Lugli, S., Manzi, V., . . . Stoica, M. (2014). The messinian salinity crisis: Past and future of a great challenge for marine sciences. Marine Geology, 352, 25-58. doi:10.1016/j.margeo.2014.02.002

Rovida, A. N., Locati, M., Camassi, R. D., Lolli, B., & Gasperini, P. (2016). CPTI15, the 2015 version of the Parametric Catalogue of Italian Earthquakes.

Rowan, M. G., & Ratliff, R. A. (2012). Cross-section restoration of salt-related deformation: Best practices and potential pitfalls. Journal of Structural Geology, 41, 24–37. https://doi.org/10.1016/j.jsg.2011.12.012

Ryan, W.B.F. (1973). Geodynamic implications of the Messinian crisis of salinity. In: Messinian Events in the Mediterranean (Ed. C.W. Drooger), pp. 26–38. North-Holland Publ. Co., Amsterdam, Netherlands.4

Ryan, W. B. F. (2009). Decoding the Mediterranean salinity crisis. Sedimentology, 56(1), 95-136. doi:10.1111/j.1365-3091.2008.01031.x

Ryan, W. B., & Cita, M. B. (1978). The nature and distribution of Messinian erosional surfaces—Indicators of a several-kilometer-deep Mediterranean in the Miocene. Marine Geology, 27(3-4), 193-230.

Ryan, W.B.F., Hsu, K.J., Cita, M.B., Dumitrica, P., Lort, P., Maync, W., Nesteroff, W.D., Pautot, P., Stradner, H. and Wezel, F.C. (1973). Initial Reports of the Deep Sea Drilling Project (Eds W.B.F. Ryan and K.J. Hsu¨), Vol. 13, pp. 1447. U.S. Government Printing Office, Washington, DC

Sartori, R. (1990). The main results of ODP Leg 107 in the frame of Neogene to Recent geology of peri-Tyrrhenian areas. In: Proceedings of the Ocean Drilling Program, Scientific Results (Vol. 107, pp. 715-730).

Sartori, R. (1990). The main results of ODP leg 107 in the frame of Neogene to recent geology of peri tyrrhenian areas. Proc., Scientific Results, ODP, Leg 107, Tyrrhenian Sea, , 715-730. doi:10.2973/odp.proc.sr.107.183.1990

Sartori, R., Colalongo, M. L., Gabbianelli, G., Bonazzi, C., Carbone, S., Curzi, P. V., Evangelisti, D., Grasso., M., Lentini, F., Rossi, S. & Selli, L. (1991). Note stratigrafiche e tettoniche sul rise di Messina (Ionio nord-occidentale). Giornale di Geologia, 53, 49-64.

Scandone, P., Patacca, E., Radoicic, R., Ryan, W. B. F., Cita, M. B., Rawson, M., et al. (1981). Mesozoic and Cenozoic rocks from Malta escarpment (Central Mediterranean). AAPG Bull. 65 (7), 1299–1319. doi:10.1306/03B5949F-16D1-11D7-8645000102C1865D

Scarascia, S., Lozej, A., Cassinis, R., 1994. Crustal structure of the Ligurian, Tyrrhenian and Ionian seas and adjacent onshore areas interpreted from wide-angle seismic profiles. Boll. Geof. Teor. Appl. 36 (141–144), 1–19.

Scarascia, S., Cassinis, R., Lozej, A., and Nebuloni, A. (2000). A seismic and gravimetric model of crustal structures across the Sicily Channel Rift Zone. Bollettino della Società Geologica Italiana, 19, 213–222.

Scarfì, L., Barberi, G., Barreca, G., Cannavò, F., Koulakov, I., & Patanè, D. (2018). Slab narrowing in the central Mediterranean: The calabro-ionian subduction zone as imaged by high resolution seismic tomography. Scientific Reports, 8(1) doi:10.1038/s41598-018-23543-8

Scarfì, L., Barberi, G., Musumeci, C., & Patanè, D. (2016). Seismotectonics of northeastern Sicily and southern Calabria (Italy): New constraints on the tectonic structures featuring in a

crucial sector for the central Mediterranean geodynamics. Tectonics, 35(3), 812-830. doi:10.1002/2015TC004022

Scarfi, L., Messina, A., & Cassisi, C. (2013). Sicily and southern Calabria focal mechanism database: A valuable tool for local and regional stress-field determination. Annals of Geophysics, 56(1) doi:10.4401/ag-6109

Schiano, P., Clocchiatti, R., Ottolini, L., & Sbrana, A. (2004). The relationship between potassic, calc-alkaline and Na-alkaline magmatism in south Italy volcanoes: A melt inclusion approach. Earth and Planetary Science Letters, 220(1-2), 121-137. doi:10.1016/S0012-821X(04)00048-2

Schmincke, H.-U., B. Behncke, M. Grasso, and S. Raffi (1997), Evolution of the northwestern Iblean Mountains, Sicily: Uplift, Pliocene/Pleistocene sea-level changes, paleoenvironment, and volcanism, Geol. Rundsch., 86, 637– 669.

Scicchitano, G., Antonioli, F., Berlinghieri, E.F.C., Dutton, A., and Monaco, C., 2008, Submerged archaeological sites along the Ionian coast of southeastern Sicily (Italy) and implications for the Holocene relative sea-level change: Quaternary Research, v. 70, no. 1, p. 26–39, doi:10.1016/j.yqres .2008.03.008.

Sclater, J. G., & Christie, P. A. (1980). Continental stretching: An explanation of the post-Mid-Cretaceous subsidence of the central North Sea Basin. Journal of Geophysical Research: Solid Earth, 85(B7), 3711–3739. https://doi.org/10.1029/JB085 iB07p 03711

Selvaggi, G., & Chiarabba, C. (1995). Seismicity and P-wave velocity image of the southern Tyrrhenian subduction zone. Geophysical Journal International, 121(3), 818-826. doi:10.1111/j.1365-246X.1995.tb06441.x

Serpelloni E., Vannucci G., Pondrelli S., Argnani A., Casula G., Anzidei M., Baldi P. & Gasperini P. (2007). Kinematics of the Western Africa-Eurasia plate boundary from focal mechanisms and GPS data. Geophysical Journal International, 169 (3), 1180-1200. doi:10.1111/j.1365-246X.2007.03367.x.

Servizio Geologico d'Italia (2011). Foglio 641 Augusta della Carta Geologica d'Italia alla scala 1:50.000. Coordinatore scientifico Carbone S. Direttore dei rilevamenti Lentini F. Note illustrative a cura di Carbone S. (ISPRA). 247.

Sgroi, T., Beranzoli, L., Di Grazia, G., Ursino, A., & Favali, P. (2007). New observations of local seismicity by the SN-1 seafloor observatory in the Ionian Sea, off-shore Eastern Sicily (Italy). Geophysical Journal International, 169(2), 490-501.

Sgroi, T., de Nardis, R., & Lavecchia, G. (2012). Crustal structure and seismotectonics of central Sicily (southern Italy): new constraints from instrumental seismicity. Geophysical Journal International, 189(3), 1237-1252.

Sirovich, L., & Pettenati, F. (1999). Seismotectonic outline of South-Eastern Sicily: an evaluation of available options for the earthquake fault rupture scenario. Journal of Seismology, 3(3), 213-233.

Speranza, F., Maniscalco, R., & Grasso, M. (2003). Pattern of orogenic rotations in central-eastern Sicily: Implications for the timing of spreading in the Tyrrhenian sea. Journal of the Geological Society, 160(2), 183-195. doi:10.1144/0016-764902-043

Speranza, F., Minelli, L., Pignatelli, A., & Chiappini, M. (2012). The Ionian Sea: The oldest in situ ocean fragment of the world? Journal of Geophysical Research B: Solid Earth, 117(12) doi:10.1029/2012JB009475

Speranza, F., Villa, I. M., Sagnotti, L., Florindo, F., Cosentino, D., Cipollari, P., & Mattei, M. (2002). Age of the corsica-sardinia rotation and liguro-provençal basin spreading: New paleomagnetic and Ar/Ar evidence. Tectonophysics, 347(4), 231-251. doi:10.1016/S0040-1951(02)00031-8

Stampfli, G. M., Borel, G. D., Marchant, R., & Mosar, J. (2002). Western alps geological constraints on western tethyan reconstructions. Journal of the Virtual Explorer, 8 doi:10.3809/jvirtex.2002.00057

Stampfli, G.M., Mosar, J., Marquer, D., Marchant, R., Baudin, T. & Borel, G., (1998). Subduction and obduction processes in the Swiss Alps, Tectonophysics, 296, 159-204.

Suppe, J. (1983). Geometry and kinematics of fault-bend folding. American Journal of Science, 283, 684e721. https://doi. org/10.2475/ajs.283.7.684

Suppe, J., & Medwedeff, D. A. (1990). Geometry and kinematics of fault-propagation folding. Eclogae Geologicae Helvetiae, 83(3), 409–454.

Tinti, S., and A. Artigliato (2003). The use of scenarios to evaluate the tsunami impact in southern Italy. Mar. Geol. 199, 221-243

Tinti, S., Armigliato, A., & Bortolucci, E. (2001). Contribution of tsunami data analysis to constrain the seismic source: The case of the 1693 eastern Sicily earthquake. Journal of Seismology, 5(1), 41-61. doi:10.1023/A:1009817601760

Tinti, S., Maramai, A., & Graziani, L. (2004). The new catalogue of italian tsunamis. Natural Hazards, 33(3), 439-465. doi:10.1023/B:NHAZ.0000048469.51059.65

Torelli, L., Grasso, M., Mazzoldi, G., Peis, D., (1998). Plio-Quaternary tectonic evolution and structure of the Catania foredeep, the northern Hyblean Plateau and the Ionian shelf (SE Sicily). Tectonophysics 298, 209–221.

Trua, T., Serri, G., & Marani, M. P. (2003). Lateral flow of african mantle below the nearby Tyrrhenian plate: Geochemical evidence. Terra Nova, 15(6), 433-440. doi:10.1046/j.1365-3121.2003.00509.x

Tugend, J., Chamot-Rooke, N., Arsenikos, S., Blanpied, C., & Frizon de Lamotte, D. (2019). Geology of the Ionian Basin and margins: A key to the East Mediterranean geodynamics. Tectonics, 38, 2668–2702. https://doi.org/10.1029/2018TC005472

Vai, G. B. (1994). Crustal evolution and basement elements in the italian area: Palaeogeography and characterization. Bollettino Di Geofisica Teorica Ed Applicata, 36(141-144), 411-434.

Valenti, V. (2010). Shallow structures at the outer calabrian accretionary wedge (NW Ionian sea): New insights from recently migrated reflection data. Terra Nova, 22(6), 453-462. doi:10.1111/j.1365-3121.2010.00964.x

Van Der Voo, R. (1993). Paleomagnetism of the atlantic, Tethys and Iapetus oceans. Paleomagnetism of the Atlantic, Tethys and Iapetus Oceans.

Van Hinsbergen, D. J. J., Vissers, R. L. M., & Spakman, W. (2014). Origin and consequences of western Mediterranean subduction, rollback, and slab segmentation. Tectonics, 33(4), 393-419. doi:10.1002/2013TC003349

Van Hinsbergen, D. J. J., Torsvik, T. H., Schmid, S. M., Maţenco, L. C., Maffione, M., Vissers, R. L. M., . . . Spakman, W. (2020). Orogenic architecture of the Mediterranean region and kinematic reconstruction of its tectonic evolution since the Triassic. Gondwana Research, 81, 79-229. doi:10.1016/j.gr.2019.07.009

Wallace, R. E. (1951). Geometry of shearing stress and relation to faulting. J. Geol. 59, 118–130. doi:10.1086/625831

Wang, W., Yin, H., Jia, D., Wu, Z., Wu, C., & Zhou, P. (2017). Calculating detachment depth and dip angle in sedimentary wedges using the area–depth graph. Journal of Structural Geology, 107, 1–11. https://doi.org/10.1016/j.jsg.2017.11.014

Wells, D. L., & Coppersmith, K. J. (1994). New empirical relationships among magnitude, rupture length, rupture width, rupture area, and surface displacement. Bulletin of the seismological Society of America, 84(4), 974-1002.

White, N. J., Jackson, J. A., & McKenzie, D. P. (1986). The relationship between the geometry of normal faults and that of sedimentary layers in their hanging walls. Journal of Structural Geology, 8, 897e910.

Williams, G., & Vann, I. (1987). The geometry of listric normal faults and deformation in their hanging walls. Journal of Structural Geology, 9, 789e795. https://doi.org/10.1016/0191-8141(87)90080-0

Aknowledgements

To Prof. **Carmelo Monaco** for his availability, for sharing his infinite knowledge and for giving me the possibility to carry out this important step for my career.

To Dr. **Giovanni Barreca** for his precious teachings and valuable discussions which highly improved my knowledge of geological processes and analytical methods.

To Dr.**Felix Gross** for his friendship, for the productive and positive discussions and for giving me the chance to work on the data of the Poseidon POS496 cruise.

To my wife Dr. **Claudia Ricchiuti** who has always supported me with her presence and her love. I cannot thank her enough for this.

To the reviewers Prof. **Sebastian Krastel** and Dr **Stephan Dominguez** for their valuable advice and detailed comments that surely improved this thesis.

For all those who have contributed to my professional growth.

THANKS!